Development of a new isogeometric finite element and its application for Lamb wave based structural health monitoring

Dissertation

zur Erlangung des akademischen Grades

Doktoringenieur
(Dr.-Ing.)

von Dipl.-Ing. Christian Willberg

geb. am 17.10.1981 in Magdeburg

genehmigt durch die Fakultät für Maschinenbau
der Otto-von-Guericke-Universität Magdeburg

Gutachter:
        Prof. Dr.-Ing. habil. Dr. h. c. Ulrich Gabbert
        Prof. Dr.-Ing. Rolf Lammering
        Prof. Dr.-Ing. Michael Sinapius

Promotionskolloquium am 06.12.2012

Danksagung

Die Danksagung ist der letzte und angenehmste Teil einer Arbeit. Als erstes möchte ich meiner Freundin Victoria Rupprecht für ihre Geduld und Unterstützung danken. Für die Möglichkeit zur Durchführung einer Promotion, für Kritik und für die Diskussionen möchte ich mich bei Professor Ulrich Gabbert bedanken. Bei Professor Rolf Lammering, trotz schwieriger Umstände, und Professor Michael Sinapius bedanke ich mich für die schnell erstellten Gutachten und die gute Zusammenarbeit im Projekt *Integrierte Bauteilüberwachung in Faserverbunden durch Analyse von Lambwellen nach deren gezielter Anregung durch piezokeramische Flächenaktoren*. Weiterhin möchte ich Professor Gerhard Mook und Professor Jürgen Pohl für die interessanten Diskussionen zum Thema Strukturüberwachung danken.

Für ein angenehmes Arbeitsklima, und reichlich förderliche, manchmal auch lustige Diskussionen am Mittagstisch, danke ich dem gesamten Institut für Mechanik. Besonders danken möchte ich Sascha (für das viele Korrektur lesen und den geteilten Ärger bei manch Publikation), Miguel (für das angenehme Zusammenleben im Büro), Mathias (für das ständige, anstrengende Hinterfragen), Zair, Seyed, Elmar (für das Erstellen absurder Theorien), Christian (für das Ertragen in der Mittagspause bei ausgedehnten "Diskussionen" mit Elmar), Steffen (beide), Corinna, Stefan und Rainer.

Natürlich dürfen meine Eltern nicht vergessen werden, schließlich würde es mich ohne sie nicht geben. Sie und meine restliche Familie (ja auch du Topher) haben mich immer unterstützt und waren da, wenn ich sie brauchte. Auch meinen Schwiegereltern möchte ich dafür danken, dass sie mich so gut aufgenommen haben. Bei meinen Freunden, diesmal vergesse ich sie nicht, möchte ich mich bedanken, dass sie mich regelmäßig aus dem akademischen Alltag herausgeholt haben. Entspannung beim Sport und bei Feiern ist notwendig um nicht während einer Doktorarbeit durchzudrehen. Dank an Frank, Sebastian, Kubi, Hofi, Maria, Jens, Vincent und allen anderen mit denen ich meine Freizeit verbracht habe.

Als Letztes möchte ich meinen neuen Kollegen für Ihre Unterstützung bei meiner Verteidigung danken. Allen denen, die noch an ihrer Arbeit schreiben, möchte ich Mut machen. Auch Ihr werdet es schaffen.

"Reality is frequently inaccurate"

- Douglas Adams -
The Ultimate Hitchhiker's Guide to the Galaxy: The Restaurant at the End of the
Universe

Contents

List of abbreviations

2D	**2** Dimensional
3D	**3** Dimensional
$\mathbf{A_0}$	first **A**nti-symmetric *Lamb* wave mode
CAD	**C**omputer **A**ided **D**esign
CMC	**C**ontinuous **M**ode **C**onversion
CFRP	**C**arbon **F**ibre **R**einforced **P**lastic
dof	**D**egrees-**O**f-**F**reedom
FEM	**F**inite **E**lement **M**ethod
FFT	**F**ast ***F**ourier* **T**ransform
GLL	**G**auss **L**obatto **L**egendre
LASER	**L**ight **A**mplification by **S**timulated **E**mission of **R**adiation
LISA	**L**ocal **I**nteraction **S**imulation **A**nalysis
NASA	**N**ational **A**eronautics and **S**pace **A**dministration
N-FEM	**N**URBS based **F**inite **E**lement **M**ethod
NURBS	**N**on-**U**niform **R**ational **B**-**S**pline
$\mathbf{S_0}$	first **S**ymmetric *Lamb* wave mode
SAFE	**S**emi-**A**nalytical **F**inite **E**lement method
SEM	**S**pectral **E**lement **M**ethod
SHM	**S**tructural **H**ealth **M**onitoring
UD	**U**ni-**D**irectional

List of mathematical operations

$\times$	vector product
$\dot{(..)}$, $\ddot{(..)}$	first and second derivative with respect to time
$(..)'$	first derivative
$(..)^k = \frac{\partial^k}{\partial(..)^k}$	k-th derivative
$(..)^T$	transpose of a matrix
$(..)^{-1}$	inverse of a matrix
$\int$	integral
$\sum$	sum
$\prod$	product
j	imaginary unit $j = \sqrt{-1}$
$\mathcal{D}$	differential operator
∇	gradient operator
$\det(..)$	determinant

List of symbols

Chapter 2

$(..)_{44}$, $(..)_{55}$, $(..)_{66}$	1313-, 2323-, 1212-direction
$(..)^{(m)}$	element number
$(..)_\phi$	matrix corresponding to electrical potential
$(..)_u$	matrix corresponding to displacement
$(..)_{u\phi}$, $(..)_{\phi u}$	matrix coupling mechanical displacement and electrical potential, vice versa
A_1, A_2, B_1, B_2	integration constants
α^h, α^p	abbrevations
$\mathbf{b}$	matrix of piezoelectric coupling constants
$\mathbf{B}$	strain-displacement matrix
$\mathbf{BC}$, $\mathbf{BS}$, $\mathbf{BV}$	B-spline curve, surface, volume
β_i, γ_i, $zeta_i$	knots
c_L, c_T	longitudinal, transversal wave velocity
C_p	capacitance
$\mathbf{C}^E$	elastic stiffness matrix measured at constant electrical field
$\mathbf{d}$	piezoelectric coupling matrix
$\mathbf{D}$	electrical displacement
δ	variation operator
$\mathbf{E}$	electrical field vector
E_C	coercive electrical field
E_{max}	maximum electrical field
$\boldsymbol{\varepsilon}$	mechanical strain vector
$\boldsymbol{\epsilon}^\sigma$	permittivity measured at constant mechanical stress
f	frequency
$\mathbf{f}$	external load vector
$\mathbf{F}$, $\mathbf{f}_{ext}$	elemental external load vector (FEM), global external load vector (FEM)
Φ	electrical potential
ϕ_N	nodal electrical potentials
h	thickness
H	electric *Gibbs* energy
$\mathbf{H}$	interpolation matrix
k	wavenumber
$\mathbf{K}_{\phi\phi}$	dielectric stiffness matrix
$\mathbf{K}_{\phi u}$	inverse piezoelectric coupling matrix
$\mathbf{K}_{uu}$	mechanical stiffness matrix
$\mathbf{K}_{u\phi}$	direct piezoelectric coupling matrix
l	length
L	*Lagrangian*

$\overline{\lambda},\ \overline{\mu}$	first and second *Lamé* constants
$\mathbf{M}_{uu}$	mass matrix
$n_{cont},\ m_{cont},\ o_{cont}$	number of control points in different local directions
$N(\beta)_{i,p_{x_1}},$	i-th B-spline basis function of order $p_{x_i}+1$ in different
$M(\gamma)_{i,p_{x_2}},\ O(\zeta)_{i,p_{x_3}}$	local directions
$\mathbf{NC},\ \mathbf{NS},\ \mathbf{NV}$	NURBS curve, surface, volume
ν	*Poisson*s ratio
ω	angular frequency
$\tilde{p},\ \tilde{q}$	abbreviations
$p_{x_1},\ p_{x_2},\ p_{x_3}$	polynomial degrees in three dimensions
P	polarization
$\mathbf{P}$	control point
$\Psi,\ \mathbf{T}$	scalar and vector potential
$Q,$	electrical charge
$\mathbf{Q},\ \mathbf{q}_{ext}$	external charge vector, external charge vector (FEM)
$R(\beta)_{i,p}$	i-th NURBS basis function of order $p+1$
ρ	mass density
S_i	surface
$\mathbf{S}^E$	elastic compliance matrix measured at constant electrical field
$\boldsymbol{\sigma}$	mechanical stresses
t	time
T	kinetic energy
T_C	*Curie* temperature
$\mathbf{u},\ \dot{\mathbf{u}},\ \ddot{\mathbf{u}}$	vector of displacement, velocity, acceleration
$\mathbf{U}_N$	nodal displacement vector
V	volume
V_C	voltage
$\mathbf{V}$	knot vector
w_i	weight of the i-th NURBS basis function
b	width
W	work
$x_1,\ x_2,\ x_3$	coordinates
Y	*Young*s modulus

Chapter 3

a	element length
C^n	n-continuity
cond	condition number
d	diameter
δ_i	constants
eps	computer accuracy
el	number of element control points
$\hat{\boldsymbol{\Phi}},\ \hat{U}$	eigenvectors
G	shear modulus

$\mathbf{J}_1, \mathbf{J}_2$	first and second Jacobian
N_i	abbrevations
ω_0	eigenfrequency
$\Omega, \tilde{\Omega}, \overline{\Omega}$	different domains
$\tilde{p}$	pressure
$\tilde{\mathbf{Q}}_1, \tilde{\mathbf{Q}}_2, \tilde{\mathbf{A}}, \tilde{\mathbf{T}}$	matrices
R	radius
$\mathbf{x}$	vector of coordinates

Chapter 4

$u_{a,b}(t)$	displacements on the measurement point A and B
$e_{A,B}$	envelope of the signal measured at points A and B
$H_{A,B}(u(t))$	*Hilbert* transform
χ_{A_0,S_0}	"nodes" per wavelength of the A_0- or S_0-mode
Lo	*Lobatto* polynomials
L_n	*Legendre* polynomials
n_P	number of periods of the excitation signal
$N_n^{\text{Lagrange},p}$	shape functions based on *Lagrange* polynomials
$N_n^{\text{Legendre},p}$	shape functions based on normalized integrals of the *Legendre* polynomials
$t_{A,B}$	centroid of the envelope $e_{A,B}$
t_c	time-of-flight
$\Theta_n(\xi)$	normalized integrals of the *Legendre* polynomials
ξ	local coordinate

Chapter 5

c	speed of light
Δf_D	frequency shift
f_{Laser}	frequency of the laser
λ_{Laser}	wavelength of the laser
v_{object}	velocity of the measured object
z_j	eigenvalues of the analytical solution

Abstract

Structural Health Monitoring (SHM) is a new, rapidly developing technology for the monitoring of engineering structures. The main features are permanent and automatic assessment of the structural integrity by built-in devices such that non-destructive testing becomes an integral part of the structure. Therefore, SHM aims at damage detection and loads monitoring by intrinsic means of the structure. The tasks can be defined similar to those of conventional non-destructive testing: damage detection, localisation and further characterisation. Consequently, this leads in an increased safety and a reduction of the maintenance costs.

Among different approaches, the use of ultrasonic *Lamb* waves is an attractive method for structural health monitoring. *Lamb* waves are able to propagate over large distances, thus wide areas of a structure can be monitored. Because *Lamb* waves sensitively interact with defects, they offer a chance for defect detection and further characterization. The use of embedded or surface-attached piezoceramic elements as actuators and sensors for generation and reception of *Lamb* waves is an attractive way for designing smart SHM structures.

To gain a better understanding of the physics of *Lamb* wave, e.g. interaction, damages, excitation process, efficient models are needed. Furthermore, in future these models can be used to develop and optimize an actuator-sensor grid for SHM systems in complex structures, e.g. airplanes. Therefore, SHM applications call for both efficient and powerful numerical tools to predict the behavior of *Lamb* waves. The mesh density required to obtain good quality solutions has to be rather fine both spatial and temporal. This results in enormous computational costs (computational time and memory storage requirements) when ultrasonic wave propagation problems are solved in the time domain. Furthermore, in future design process one has to deal with complex structures. To resolve the issue of complex structures the thesis utilize the idea of the isogeometric element concept. The isogeometric approach utilizes the non-uniform rational B-spline (NURBS) functions of the geometrical description of the computer aided design (CAD) software. Therefore, no meshing in the todays common way is needed.

To model the complete SHM structure including actuators and sensors, in this thesis a three-dimensional isogeometric piezoelectric finite element is developed, tested in several benchmarks and compared to other numerical higher order approaches with respect to their ability to model *Lamb* wave propagation problems. The research results are used to recommend an optimal discretization scheme. To illustrate the advantage of the new isogeometric finite element two SHM specific problems are investigated, namely the dynamic behavior of a piezoceramic actuator and the material induced continuous mode conversion. Both problems are studied numerically as well as experimentally.

Zusammenfassung

Die Idee des Structural Health Monitoring (SHM) besteht darin, Strukturen während des Betriebs kontinuierlich zu überwachen. Die Vorteile liegen in einer automatisierten, zerstörungsfreien und permanenten Überwachung der strukturellen Integrität. Schäden sollen frühzeitig erkannt, lokalisiert und charakterisiert werden. Hierdurch sollen sowohl die Sicherheit gesteigert als auch die Wartungskosten verringert werden.

Ein vielversprechender Ansatz zur Strukturüberwachung stellt die Nutzung von Lambwellen dar. Lambwellen sind in der Lage, große Distanzen zu überwinden und sind sensitiv gegenüber Schäden. Dies ermöglicht eine großflächige Überwachung von Strukturen, wie sie in Flugzeugen vorzufinden sind. Die Nutzung von integrierten oder applizierten Piezokeramiken hat sich dabei als besonders vielversprechend herausgestellt, da diese sowohl als Aktuatoren als auch als Sensoren verwendet werden können.

Für die Untersuchung des physikalischen Verhaltens von Lambwellen, z.B. die Schadensinteraktion, oder das Anregungsverhalten von Piezokeramiken, werden effiziente Modelle benötigt. Zukünftig sollen diese Modelle verwendet werden, um Aktuator-Sensor Netzwerke für komplexe Strukturen, wie Flugzeuge, zu entwickeln und zu optimieren. Daher werden effiziente und genaue numerische Werkzeuge benötigt, um das Verhalten von Lambwellen vorherzusagen. Für die notwendige Lösungsqualität wird eine hohe räumliche und zeitliche Auflösung benötigt. Aus der Berechnung von Lambwellen im Zeitbereich resultiert daher ein hoher Rechenzeit- und Speicheraufwand.

Da im zukünftigen Entwicklungsprozess komplexe Strukturen berücksichtigt werden müssen, wird in dieser Arbeit die Idee des isogeometrischen Elementkonzeptes verfolgt. Isogeometrische finite Elemente nutzten die geometrische Beschreibung mit Hilfe von non-uniform rational B-spline (NURBS) Funktionen, welche in der CAD Software benutzt werden, als Ansatzfunktionen für die Finite-Elemente-Formulierung. Eine Diskretisierung der geometrischen Modelle in der heute üblichen Weise wird nicht benötigt. Um die Gesamtstruktur mit Aktuatoren und Sensoren zu modellieren, wird in dieser Arbeit ein dreidimensionales piezoelektrisches isogeometrisches finites Element entwickelt, getestet und auf seine Fähigkeiten zur Lambwellenberechnung mit anderen finiten Elementen höherer Ordnung in einem Benchmark verglichen. Die Ergebnisse werden genutzt, um ein optimales Diskretisierungsschema vorzugeben. Um die Vorteile des neuen isogeometrischen Elementes darzustellen, werden zwei SHM spezifische Probleme untersucht. Zum Einen wird der Einfluss der Eigendynamik des Aktuator studiert und zum Anderen wird die materialinduzierte kontinuierliche Modenkonversion. Neben den numerischen Untersuchungen werden auch Messsungen mit Hilfe der Laser-Scanning-Vibrometrie durchgeführt und die Ergebnisse verglichen.

1 Introduction

> *To Columbia, here is Houston; we see your tyre pressure messages and we did
> not copy your last message.*
> *After a moment, Husband replied: "Roger but ..."*

In the year 2003 by entering the atmosphere the space shuttle Columbia explodes. Seven months after the crash the reason of the accident was found. During the start a piece of insulating foam breaks from the fuel tank and hits the wings leading edge. The impact caused a hole. Through this hole high temperature plasma could reach the inner structure and destroyed the shuttle [3].

1.1 Principle of structural health monitoring and its motivation

The Columbia disaster illustrates that a small leak can sink a great ship. It was known that the shuttle was hit by a piece of frozen foam. However, an analysis of the impact zone was not possible and the existence or the size of the damage was not known. This disaster points out in an appalling way the importance of health monitoring measurements for safety relevant component parts. In standard applications even the impact event itself is not observed. Airplanes, bridges and other engineering structures are not monitored continuously by cameras like a space flight. Therefore, the time of the damaging event is not thoroughly known.

In maintenance and inspection cycles parts of the structure are checked. Between the cycles no information about the structure exist. In 2005 the fall of the vertical stabiliser of Flight TS961 (Airbus A310) occurred just five days after its routine check and the next major inspection was scheduled for 2006 [143].

To close the inspection gap in the maintenance cycles the idea of an continuous structural monitoring was born. In the early 1990s first research teams explicitly dealt with the term structural health monitoring (SHM), although the basic idea can be tracked back to much earlier works [130]. SHM is defined as *"the nondestructive and continuous monitoring characteristics using an array of sensors related to the fitness of an engineered component as it operates, so as to diagnose the onset of anomalous structural behaviour. It involves measuring and evaluating the state properties and relating these to defined performance parameter"* [143].

Figure 1.1 illustrates the basic idea of a SHM system. A SHM application works as "nervous system" of the structure. If a damage reaches a critical size the monitoring system feels "pain" and the structure is inspected systematically and repaired if necessary.

Human nervous system   Structure

+

Structural **H**ealth **M**onitoring (SHM)
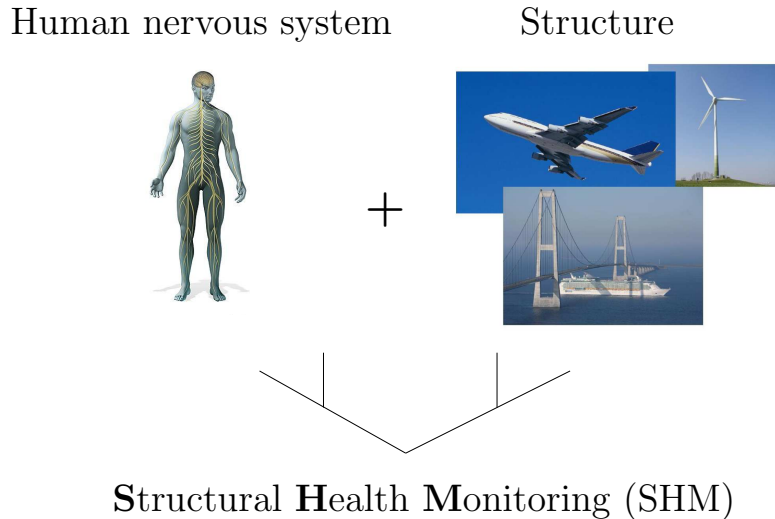
Figure 1.1: Basic idea of structural health monitoring (SHM).

Because of the continuous structural inspection the time between scheduled maintenances can be increased as well as the operating life of the structure. This leads to a reduction of the running costs. Major research programmes in the field of SHM assume that up to 20% of current maintance/inspection costs can be saved in civil and military transportation by the use of integrated on-line damage monitoring systems [139]. Table 1.1 shows exemplarily that 44% of the inspection time can be reduced by using an online monitoring system, e.g. by a partial substitution of the flight line inspection or an extension of the time between scheduled inspections.

Table 1.1: Inspection time effort for a modern fighter aircraft [139].

Inspection type	Current inspection time (% of total)	Estimated potential for smart systems	Time saved (% of total)
Flight line	16	0.40	6.4
Scheduled	31	0.45	14.0
Unscheduled	16	0.10	1.6
Service instructions	37	0.60	22.2
	100		44.0

1.2 State of the art

The opportunities to use SHM systems are given for several engineering applications. However, useful monitoring strategies have to be developed, which take the structural as well as environmental conditions into account. Depending on the SHM application different physical principles can be utilized. Some strategies are already in use or almost fully developed. The health and usage monitoring for propulsion systems is highly advanced. Different in-flight Engine Condition Monitoring (ECM) systems have gradually developed and are still further improved [18]. Health and usage monitoring has also been successfully

introduced to the helicopter industry, mainly to monitor vibrations on gears and specifically gear shafts, which once a crack has emerged have a relatively short crack propagation life [18].

Kuroishi et al. [79] reported on a guided wave pipe inspection monitoring system intended for the application to thermal power plants. The use of this system reduces the maintenance cost, because less heat insulation has to be removed. Furthermore, the inspection can be made until the working process, which also reduces the cost. In civil engineering SHM systems are already in use. One example is an online monitoring system for the Tsing Ma bridge in China, which works since the bridges commissioning in May 1997 [23]. However, for every structure which should be monitored a special solution has to be developed and many open-ended questions still exist. Particularly, for complex light weight structures, e.g. windturbines and airplanes no SHM system is available, yet. In recent years quite a lot of scientific work has been done to close the gap between laboratory and "real world" applications.

Various different standard non-destructive testing and SHM methods are studied by Ciang et al. [25] for their applicability for the monitoring of windturbines. They conclude that wind power generation systems are huge and expensive to construct and maintain. Therefore, the related industries require SHM systems that can provide cost effective maintenance programmes which deliver accurate detection of faults as early as possible. However, no distinctive idea to realize such monitoring system is given. In the following, some of the common approaches for SHM systems are presented.

1.2.1 Strategies of SHM

Several approaches are investigated to realize SHM systems. There are strategies based on static measurements as strain gages or fibre bragg sensors [70, 94], as well as dynamic strategies, e.g. modal analysis for structural monitoring [151].

Furthermore, one can distinguish between active and passive systems. Passive systems "feel" the impact through a structure, "hear" the evolution of a damage (acoustic emission) or exploit the vibration caused by wind or an engine to monitor a damage [117] . Active systems use energy, e.g. to excite waves which interact with the damage or stimulate vibrations. Sensors measure the response of the structure. Damages influence the vibration or the traveling waves. The difference in the signal between damaged and undamaged structures could be determined and used as criterion for a defect [113].

Methods which apply structural vibration [46] or modal parameters [151] are another class of ideas for damage detection. Furthermore, the impedance spectroscopy can be used to determine the structural health. The electrical impedance of a applied piezoceramic patch is influenced by stiffness changes in the structure, adhesive layer or the ceramic itself [7, 90, 107, 114]. Therefore, this measurement strategy has a great potential to check actuator-sensor networks which deploy piezoceramics. Bhalla et al. investigated the influence of changes of the adhesive layer to the impedance curve [17].

One favorable active method in thin-walled light-weight structures is based on *Lamb* waves. *Lamb* waves are elastic waves which occur in thin-walled structures and named after Horace *Lamb* who has first described these waves in 1917 [81]. *Lamb* waves exist at least in two modes for every given frequency and they are also dispersive. They interact with damages and in recent years a lot of research has been done to understand their properties [18, 49, 84, 85, 127, 136, 140, 143, 155, 157, 160, 161]. In this thesis primarily thin-walled

structures are studied. Therefore, the researches on *Lamb* waves are presented in the next subsection.

1.2.2 Previous work

Designing SHM systems requires the expertise of a variety of different scientific disciplines, primarily of engineering sciences like machine construction or electrotechnology, but also of computer science, mathematics and physics for instance [130]. Detailed investigations are executed experimentally as well as numerically.

Often experiments measure the complete wave field in a structure to study damage interaction or *Lamb* wave excitation. Typically laser scanning vibrometers are utilized [88, 140], because they have a high spatial resolution and need no coupling medium. Moreover, air coupled ultrasonic measurements [59, 60] or speckle interferometry [82] can be used to scan wave fields of *Lamb* waves without a coupling media.

With measurements dispersion curves can be determined using a three-dimensional fast *Fourier* transform (FFT) [8]. The results can be used to verify mathematical models [4, 56, 57, 171]. Many investigations for plates made of isotropic materials have been done [62, 84–86, 98]. With respect to the development of SHM systems for aeronautic structures multi-layer composite materials are also in the focus of investigations. In that case the material properties are very complex [148, 173]. Furthermore, for multi-layer composite materials different types of damages, such as impact damages [99] or delaminations [123, 147, 150], have to be taken into account in comparison to isotropic metal materials. Moreover, the material is anisotropic, which makes the damage detection very hard [42, 98, 135, 153]. Effects of *Lamb* wave reflection [4, 34], damping [122] or mode conversion [4, 24, 75, 169] in composite plates have been studied. Moreover, Andrews et al. [6] show the influence of temperature to the group velocity.

Piezoceramic patches are commonly used to excite *Lamb* waves in structures, but other methods could be used as well, e.g. Nakano et al. (1991) used a thermal source (laser beam) to excite *Lamb* waves [103]. Yan et al. applied the thermal excitation of *Lamb* waves to study the leaky *Lamb* wave phenomenon [172]. However, this method has no practical importance for SHM applications.

Investigations of different types of thin piezoceramic transducers are made by Giurgiutiu et al. [49]. Studies regarding the actuator or phased array designs are done by Ostachowicz et al. [4, 105, 134]. Moulin et al. work with embedded instead of surface bonded piezoceramics [102].

The influence of the adhesive layer between the actuator and the plate is studied by Sirohi et al. [22, 119, 120, 136, 163]. They focused on the so called "shear lag" effect. The effect describes a reduction of the transfer of the shear stresses from the actuator to the host structure caused by the adhesive layer. Ha et al. found that the eigendynamic of thicker piezoceramics dominantly influences the amplitude of the excited *Lamb* waves [54, 116]. The influence of debonding is studied by Blackhire et al. [83, 109, 110]. Furthermore, Huang et al. showed that unsymmetric eigenforms of the piezoeceramic transducer cause an unsymmtric wavefield amplitude characteristic [64] just as the soldering points used to contact the piezoceramic actuators [168].

In addition to the experimental investigations numerical tools for *Lamb* wave simulation are in development, e.g. to support the SHM development process. The given brief overview about the complex properties of *Lamb* waves shows that there are many requirements to develop an effective simulation tool, which are:

- Low computational effort regarding a fine spatial and temporal discretization.
- Flexibility in modeling different types of materials as piezoelectric or multi-layer composites, with linear or non-linear constitutive equations.
- Possibility of modeling complex geometries (damages, airplane fuselage, etc.).
- Possibility to describe delaminations or cracks inside the material.
- Exchangeability of the models between different parts of the structural design process (static, eigenvalue, SHM design analysis).

Various different tools have been developed for the simulation of *Lamb* wave propagation. Analytical methods are advanced from the original solution of Horace Lamb to more complex material properties, but they are limited in describing complex geometries or multi-layer materials [49, 158, 160]. The semi-analytical finite element methods (SAFE) use an analytical approach in direction of the wave propagation and a discrete finite element approximation perpendicular to this direction. This offers fast and accurate results and is often used to calculate dispersion curves. To study complex geometries one has to couple this method with standard finite elements and an extension to three dimensions is hardly done [4].

The local interaction simulation approach (LISA) by Lee et al. [84] based on the central difference scheme or the mass-spring lattice model (MSLM) by Yim et al. [175] are also confined to non-complex geometries. The MSLM material parameters have no physical meaning, because in complex structures a local spring stiffness is not measurable.

To break the limitations of the geometrical description several finite element approaches are investigated. Mostly these approaches are based on utilizing higher order polynomial shape functions to reduce the computational effort. The so called spectral finite elements (SEM) is deployed in the time [77, 93, 105] or the frequency domain [168]. Some of these approaches are based on utilizing higher order shell finite elements to describe thin structures [77, 93, 105]. However, they have the drawback that multi-layered materials and complex three-dimensional stress states arising at welded joints or rivets, for example, cannot be resolved. Moreover, the symmetric *Lamb* wave mode can not be described by plate elements, because the elements assume a constant strain state in the thickness direction of the plate.

Therefore, three-dimensional SEM approaches based on *Lagrange* polynomials on the *Gauss-Lobatto-Legendre* grid have been developed [76, 78, 130]. When higher order finite element approaches are considered SEM has been used almost exclusively for high frequency wave propagation problems. Other higher order approaches as p-FEM, which apply the normalized integrals of the *Legendre* polynomials [145] or isogeometric finite elements utilize non-uniform rational B-splines (NURBS) [66] have been principally utilized for static problems including non-linear analyses, plasticity, etc.

To handle the increasing complexity of structures, in recent years the so called isogeometric element concept was developed. This concept closes the gap between computer aided designs (CAD) and finite element analysis (FEA) [12, 13, 29, 31, 66]. The isogeometric concept uses the functional description of the geometry from the CAD software (B-splines, NURBS, T-splines, etc.) and reuses them as shape function for the FEA [29]. No discretization process, which approximates the CAD geometry function description

with other functions, e.g. *Lagrange* polynomials, is required and, consequently, the exact description of the geometry is not lost. This is an important consideration for shape optimization schemes. Not only the exchange between finite element software and CAD software works better, but also the exact CAD geometry is used for the optimization. This allows an accurate state of the problem instead of a discretized mesh used by standard finite elements, which leads to better solutions in the optimization process [118]. However, the performance of this approach has not be applied to *Lamb* wave based problems, this includes the development of a piezoelectrical element.

1.3 Objective and outline of the thesis

Because of their numerical properties offering tremendous advantages the application of isogeometric finite elements will drastically increase in the near future. In order to model Lamb wave based SHM systems not only displacement finite elements but also multiphysics ones are required. The monitored structures often have complex geometries and isogeometric finite elements have shown their capability to model them, e.g. abdominal aorta models [12] or the NASA aluminum testbed cylinder (ATC) [29]. Furthermore, as known from other higher order finite element schemes also isogeometric finite elements are less prone to locking. For polynomial orders $p \geq 4$ the locking phenomenon does not pollute the solution noticeably [43]. Since NURBS based elements hardly suffer from locking phenomena, adhesive layers as well as thin-walled structures can be modeled using a three-dimensional approach. However, the behavior of isogeometric finite elements in the dynamic case is not well studied and understood yet. Only one-dimensional studies, research on two-dimensional membranes and eigenvalue analysis have been conducted [31, 124]. So far, isogeometric finite elements have not been investigated regarding their capability to simulate *Lamb* wave based problems. Moreover, piezomechanical properties which allow the modelling of transducers have not be considered until now. Therefore, the following needs to be address:

- Are isogeometric finite elements an effective numerical tool to model *Lamb* wave based problems?
- How is it possible to determine the quality of the solution of *Lamb* wave propagation problems?
- What is the influence of the inter-element-continuity to the convergence behavior of isogeometric finite elements in a transient analysis?
- What are the advantages of isogeometric finite elements compared to other higher order approaches?
- Are isogeometric finite elements able to describe complex SHM specific problems?

To answer these questions a three-dimensional piezoelectric finite element has to be developed and tested. Several static and eigendynamic benchmark tests are derived to proof the reliability of the element. The maximal permissible aspect ratio is to be determined. This bound on the element distortion can then be used for an effective modelling of thin layers, e.g. as the adhesive layer between structure and actuator or sensor.

Up to now the isogeometric finite element is only compared with analytical reference solutions or conventional finite elements. In this thesis another approach will be taken. Here, the NURBS based elements will be compared with two other higher order finite element

approaches. Their convergence behavior and the quality of the solution are scrutinized. After studying its numerical properties the isogeometric element is used to investigate two SHM specific problems. First the effect of resonance on the uncoupled and coupled piezoceramic is studied and compared with experiments. Second the isogeometric approach is used to model the structure of a twill fabric plate, to show the possibility of modeling complex structures. This result is used to study the material induced continuous mode conversion (CMC) in detail.

To answer to the previously stated questions the thesis is structures in the following way:

1. Development of the isogeometric piezoelectric finite element.
2. Testing of the isogeometric piezoelectric finite element using several benchmarks.
3. Comparison of the isogeometric piezoelectric finite element to experimental and numerical results.
4. Application of the isogeometric element to two SHM specific problems.
5. Evaluation of tge pro and contras of isogeometric finite elements with respect to design SHM systems.

In detail the thesis is divided into five main chapters:

Theoretical background: In the second chapter the basic analytical equations of *Lamb* waves are recalled. These equations are later used to calculate reference solutions as well as the dispersion curves. The properties of the *Lamb* waves are explained. To be precise, only guided waves arising in thin-walled structures made of isotropic material ought to be called *Lamb* waves. However, in this thesis the term *Lamb* wave is extended, in compliance with the commonly accepted usage in the literature, to all guided waves in thin-walled structures. To excite *Lamb* waves in structures typically piezoceramic actuators are used. Therefore, the basic material properties and governing equations of piezoelectricity are explained. The development of a electromechanical finite element is shown thereafter. For the development of the isogeometric finite element approach the shape functions are introduced. Here, the properties of non-uniform rational B-splines (NURBS) are explained as well.

Development of a new piezomechanical 3D NURBS element: In the third chapter the development of an isogeometric finite element with electromechanical coupling is shown. The basic FEM equations and the shape functions that have been introduced in the previous chapter are used. Differences to standard finite elements are shown. Static and dynamic verification tests are conducted, e.g. the patch test and the modal analysis. The convergence behaviour is studied as well. As known from this type of element the geometrical description is exact and thus better compared to isogeometric finite elements. [29]. Hence, the influence of the geometry description is also studied. Finally the locking phenomenon is scrutinized in order to guarantee the accuracy of the solution when dealing with thin-walled structures.

Comparison and evaluation of the NURBS element with alternative approaches for *Lamb* wave simulation: In the fourth chapter the isogeometric approach is compared to two different higher order numerical methods for simulating *Lamb* waves. A two-dimensional isotropic aluminum plate is modeled and the wave is excited using a point force

model. An adapted analytical solution is used to compare the convergence properties in terms of the group velocity of the two basic *Lamb* wave modes. The isogeometric method is compared with spectral finite elements based on *Lagrange* polynomials and p-elements based on the normalized integrals of the *Legendre* polynomials. Furthermore, the influence of the inter-element-continuity to the convergence rate of the isogeometric finite element is investigated.

Application of the NURBS finite elements to SHM problems: The fifth chapter is devoted to study two SHM based problems. The chapter first introduces the experimental method which has been used to verify the numerical results. The first SHM based problem studies the *Lamb* wave excitation process. It started with the eigendynamic of of a free piezoceramic disc. The numerical results are compared with the experimental one. Experimental investigations show that the resonances of the coupled piezoceramic actuators have a big impact on the excited *Lamb* wave. Therefore, the parameters, e.g. adhesive layer, actuator geometry, which influence the resonance are studied. This part of the research is done numerically deploying the developed isogeometric finite elements.
The second SHM based problem is about the phenomenon of continuous mode conversion (CMC). Several experiments have shown that in certain CFRP plates a conversion between the two basic *Lamb* modes occurs continuously. The phenomenon is described using experimental data. However, a numerical model is useful to understand the effect and the reason of CMC. The numerical effort in modeling this phenomenon is very high, caused by the geometric structure of the composite. Therefore, the NURBS based approach is used to create a simplified as well as complex model to reduce the numerical effort. The solutions will be compared with experimental findings.

Conclusion and outlook: In the last chapter the thesis is concluded. The main results are briefly summarized and a few comments on future work are given.

2 Theoretical background

2.1 Introduction

The chapter provides an overview of the theoretical background of this thesis. The research is focused on the simulation of *Lamb* waves used for SHM applications. As pointed out in chapter 1 *Lamb* waves are elastic waves which occur in thin-walled structures. In the first part of chapter 2 the analytical *Lamb* wave solution in an isotropic material is developed. This solution can be used as reference to determine the quality of numerical approaches. Moreover, frequently used terms like dispersion, *Lamb* mode, mode conversion etc. are introduced.

The second part of the chapter deals with piezoelectric materials. Surface bonded piezoceramic patch actuators are a common way to excite *Lamb* waves. Due to the fact that the coupling between an electrical field and a mechanical deformation is invertible the piezoceramics can be used both as actuators and as sensors. The material law is needed to develop a finite element which includes elastic and piezoelectric properties.

The third part of the chapter provides a short overview of the FEM. Since the analytical approaches are limited to simple geometries and materials numerical FEM approaches, for instance, are needed to circumvent the limitation of the analytical *Lamb* wave solution. The FEM divides the stated complex problem in several subsections. To obtain an accurate solution of a *Lamb* wave simulation model a fine spatial and temporal discretization is required. To minimize the computational effort an alternative mathematical description of the finite elements is figured out. An isogeometric approach based on NURBS is developed in the next chapter. Therefore, in the last part of this chapter the B-spline and NURBS functions are introduced and some of their advantages, e.g. the accuracy of the geometrical description, are shown. With respect to future applications more complex structures need to be computed for the design of SHM systems.

2.2 *Lamb* waves

Lamb waves are a special type of ultrasonic waves. They refer to elastic perturbations propagating in elastic solid plates (or layers) with free boundaries, for which displacements occur both in the direction of wave propagation and perpendicular to the plane of the plate [155]. The first mathematical description of this phenomenon has been made by Horace Lamb in 1917 [81] and later named after him. *Lamb* waves are of two basic types, a symmetric and an anti-symmetric one. For each propagation type exists a number of modes corresponding to the solution of the mathematical model defined by *Lamb* [49]. Furthermore, these modes can convert into each other under special conditions, e.g. reflections at flat bottom holes [169], and they are dispersive. The properties which make them interesting for SHM applications are their small wavelengths (in higher frequency range) and only a slight loss of amplitude magnitude ($1/\sqrt{r}$) in relation to the traveled

distance r [143]. For damage detection they are widely in use [84, 91, 143].

This section illustrates the mathematical theory of *Lamb* waves. The fundamental equations are derived. To understand the properties of *Lamb* waves the analytical statement of the problem is helpful. Therefore, the derivation of the equations for an isotropic material in a thin plate starting from the *Navier* wave equation is shown in the following.

2.2.1 Isotropic 3D wave equation

It is dealt with the problem of wave propagation in a three-dimensional isotropic material. To describe the point displacement, the solution of the 3D wave equation is needed. For more details refer to Lai et al. [80]. It is started from the *Navier* wave equation

$$(\overline{\lambda} + \overline{\mu})\boldsymbol{\nabla}\boldsymbol{\nabla} \cdot \mathbf{u} + \overline{\mu}\boldsymbol{\nabla}^2\mathbf{u} + \mathbf{f} = \rho\ddot{\mathbf{u}}\,, \tag{2.1}$$

with the *Lamé* constants $\overline{\lambda}$ and $\overline{\mu}$. For an isotropic material, both are related to the *Young*s modulus Y and the *Poisson*s ratio ν [16]. The vector $\mathbf{u}$ is the displacement $\mathbf{u} = \mathbf{u}(x_1,\, x_2,\, x_3,\, t)$, $\ddot{\mathbf{u}}$ the acceleration, $\mathbf{f}$ is the external load vector, $\boldsymbol{\nabla} = \mathrm{grad}(..)$ is the gradient operator and ρ is the mass density. Using the *Helmholtz* decomposition, which separates the displacement in a scalar potential Ψ and a vector potential $\mathbf{T}$

$$\mathbf{u} = \boldsymbol{\nabla}\Psi + \boldsymbol{\nabla} \times \mathbf{T}\,, \tag{2.2}$$

complemented by the uniqueness condition

$$\boldsymbol{\nabla}\mathbf{T} = 0\,, \tag{2.3}$$

one obtains

$$\boldsymbol{\nabla}\left((\overline{\lambda} + 2\overline{\mu})\boldsymbol{\nabla}^2\Psi - \rho\ddot{\Psi}\right) + \boldsymbol{\nabla} \times \left(\overline{\mu}\boldsymbol{\nabla}^2\mathbf{T} - \rho\ddot{\mathbf{T}}\right) = 0\,. \tag{2.4}$$

The terms in the parentheses must be independently zero to fulfill Equation (2.4) which leads to

$$\begin{aligned} \boldsymbol{\nabla}^2\Psi &= \frac{1}{c_L^2}\ddot{\Psi}\,, \\ \boldsymbol{\nabla}^2\mathbf{T} &= \frac{1}{c_T^2}\ddot{\mathbf{T}}\,. \end{aligned} \tag{2.5}$$

The constants c_T and c_L

$$\begin{aligned} c_T &= \sqrt{\frac{Y}{2\rho(1+\nu)}}\,, \\ c_L &= \sqrt{\frac{Y(1-\nu)}{\rho(1+\nu)(1-2\nu)}}\,, \end{aligned} \tag{2.6}$$

are described as velocity of the transversal and longitudinal wave for an elastic isotropic solid [155]. With these basic equations the three-dimensional problem of wave propagation in an isotropic material is solved. With the aid of these concepts it is explained how the solution of *Lamb*s problem can be derived.

2.2.2 Derivation of the *Lamb* wave equations for a plate

Based on the *Helmholtz* decomposition (see Equation (2.2)) for the 3D wave equation the solution for *Lamb*s problem is derived. The model is an infinite plate, where the upper and lower boundaries are stress free. The plates cross section is sketched in Figure 2.1. It is assumed that applied loads do not depend on the x_2-direction. All quantities in Equations (2.1) - (2.3) become independent from x_2, and a two-dimensional problem can be considered [104]. For more details refer to Lamb [81] and Viktorov [155].
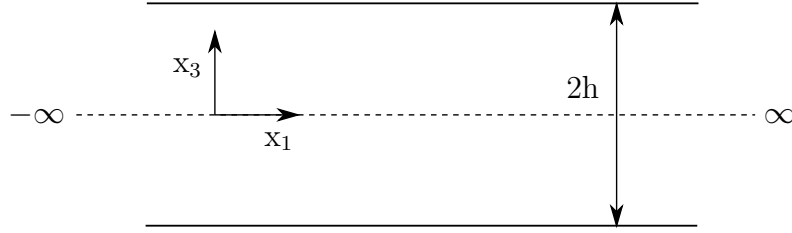

Figure 2.1: 2D plate model with coordinates.

In case of a harmonic motion an ansatz of the form

$$
\begin{aligned}
\Psi(x_1,\, x_3,\, t) &= g(x_3)e^{j(kx_1-\omega t)}, \\
T_3(x_1,\, x_3,\, t) &= h(x_3)e^{j(kx_1-\omega t)},
\end{aligned}
\tag{2.7}
$$

is suitable to describe the wave propagation in a plate with the wave number k and the angular frequency $\omega = 2\pi f$. The functions $g(x_3)$ and $h(x_3)$ are chosen as [49]

$$
\begin{aligned}
g(x_3) &= A_1 \sin(\tilde{q}x_3) + A_2 \cos(\tilde{q}x_3), \\
h(x_3) &= B_1 \sin(\tilde{p}x_3) + B_2 \cos(\tilde{p}x_3).
\end{aligned}
\tag{2.8}
$$

The unknowns $\tilde{p}$ and $\tilde{q}$ are abbreviations for

$$
\tilde{p}^2 = \frac{\omega^2}{c_L^2} - k^2 \qquad \text{and} \qquad \tilde{q}^2 = \frac{\omega^2}{c_T^2} - k^2.
\tag{2.9}
$$

The variables A_1, A_2, B_1 and B_2 are integration constants. Substituting Equation (2.8) into Equation (2.2) the displacements are

$$
\begin{aligned}
u_1 &= \quad A_2 jk \cos \tilde{p}x_3 + B_1 \tilde{q} \cos \tilde{q}x_3) + (A_1 jk \sin \tilde{p}x_3 - B_2 \tilde{q} \sin \tilde{q}x_3), \\
u_3 &= -(A_2 \tilde{p} \sin \tilde{p}x_3 + B_1 jk \sin \tilde{q}x_3) + (A_1 \tilde{p} \cos \tilde{p}x_3 - B_2 jk \cos \tilde{p}x_3).
\end{aligned}
\tag{2.10}
$$

With the derivatives of the potentials Ψ and H_3 with respect to x_3 and the *Lamé* constant $\overline{\mu}$, the shear stresses σ_{31} are given by

$$
\begin{aligned}
\sigma_{31} = \overline{\mu}[&-A_2 2jk\tilde{p} \sin \tilde{p}x_3 + B_1(k^2 - \tilde{q}^2) \sin \tilde{p}x_3 \\
&+ A_1 jk\tilde{p} \cos \tilde{p}x_3 + B_2(k^2 - \tilde{q}^2) \cos \tilde{q}x_3]
\end{aligned}
\tag{2.11}
$$

and the normal stresses σ_{33} are given by

$$
\begin{aligned}
\sigma_{33} = \overline{\mu}[&A_2(k^2 - \tilde{q}^2) \cos \tilde{p}x_3 - B_1 2jk\tilde{q} \cos \tilde{q}x_3 \\
&+ A_1(k^2 - \tilde{q}^2) \sin \tilde{p}x_3 + B_2 2j\tilde{q} \sin \tilde{q}x_3].
\end{aligned}
\tag{2.12}
$$

Including the boundary conditions (stress free surface)

$$\sigma_{31}(x_1, -h) = \sigma_{31}(x_1, h) = 0,$$
$$\sigma_{33}(x_1, -h) = \sigma_{33}(x_1, h) = 0 \tag{2.13}$$

in Equations (2.11) and (2.12) a system of equations is obtained to calculate the integration constants A_1, A_2, B_1 and B_2. It can be noted that the constants A_2 and B_1 are independent from A_1 and B_2. Since the constants are decoupled the original system of equations can be split in two, one for each basic type of the waves. In matrix form they can be written as

$$\begin{bmatrix} -(k^2 - \tilde{p}^2)\cos(\tilde{q}h) & 2jk\tilde{p}\cos(\tilde{p}h) \\ -2jk\tilde{q}\sin(\tilde{q}h) & (k^2 - \tilde{p}^2)\sin(\tilde{p}h) \end{bmatrix} \begin{bmatrix} A_2 \\ B_1 \end{bmatrix} = \begin{bmatrix} 0 \\ 0 \end{bmatrix} \tag{2.14}$$

and

$$\begin{bmatrix} -(k^2 - \tilde{p}^2)\sin(\tilde{q}h) & -2jkp\sin(\tilde{p}h) \\ 2jk\tilde{q}\cos(\tilde{q}h) & (k^2 - \tilde{p}^2)\cos(\tilde{p}h) \end{bmatrix} \begin{bmatrix} A_1 \\ B_2 \end{bmatrix} = \begin{bmatrix} 0 \\ 0 \end{bmatrix}. \tag{2.15}$$

The system of equations describes a symmetric and an anti-symmetric movement of the particles with respect to the central plane of the plate. To obtain non trivial solutions for this system the determinants of the system matrices must vanish, leading to the so called dispersion relation. The solutions are

$$\frac{\tan(\tilde{p}h)}{\tan(\tilde{q}h)} + \frac{4\tilde{p}\tilde{q}k^2}{(k^2 - \tilde{p}^2)^2} = 0 \tag{2.16}$$

for the symmetric part and

$$\frac{\tan(\tilde{q}h)}{\tan(\tilde{p}h)} + \frac{(k^2 - \tilde{p}^2)^2}{4\tilde{p}\tilde{q}k^2} = 0 \tag{2.17}$$

for the anti-symmetric one, respectively. Normally the influence of changing the product frequency times thickness is displayed in dispersion curves of the *Lamb* modes. These curves show the phase or group velocity in relation to the frequency times thickness product of the plate. To obtain the results of the dispersion curves the Equations (2.16) and (2.17) have to be solved. In Figure 2.2A the dispersion curve of the phase velocity

$$c_p = \frac{\omega}{k} \tag{2.18}$$

for an aluminum plate is displayed. The material data are given in Table A-1. The dispersion describes the dependency of the phase or group velocity of a *Lamb* wave from the product of frequency times thickness. Between 0 and 4 MHzmm four modes exist, two symmetric ones (S_0, S_1) and two anti-symmetric ones (A_0, A_1). At higher frequencies the wavelength of the modes becomes shorter. Ultimately the velocities of the different modes converge to the *Rayleigh* wave speed [155]. In the dispersion curves the cut off frequencies of the higher modes (A_1, S_1) can be seen. The A_1-mode exist only for fh higher than 1.5 MHzmm, analogously the S_1 mode for 2.5 MHzmm. For higher frequencies more modes exist. In SHM applications based on *Lamb* waves the fh range below the first cut off frequency is used to simplify the received signals, because only S_0- and A_0-modes are present.

The group velocity, shown in Figure 2.2B, is defined as

$$c_g = \frac{\partial \omega}{\partial k}. \tag{2.19}$$

(A) Phase velocity curve   **(B)** Group velocity curve
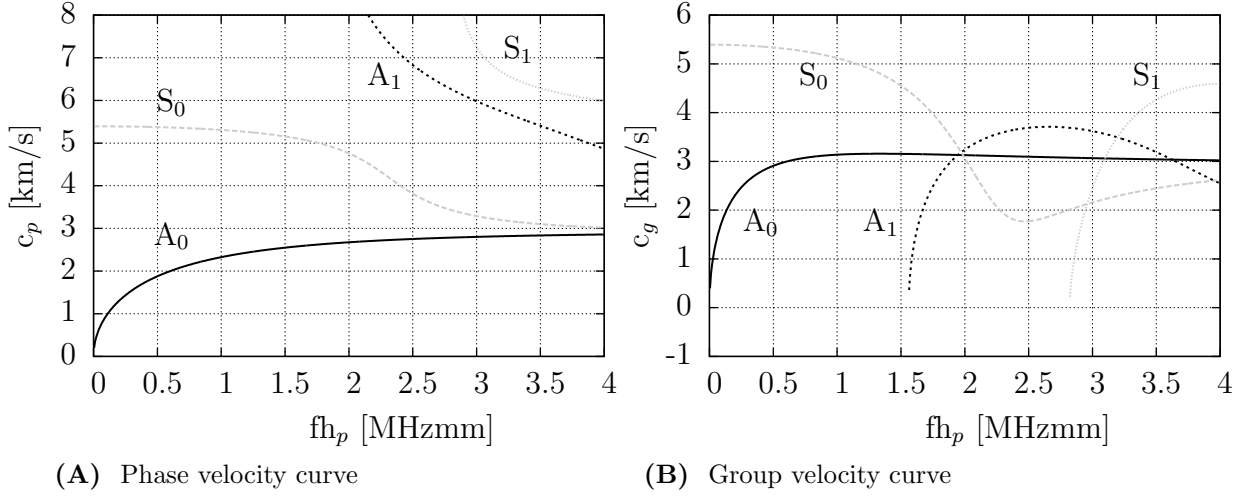
Figure 2.2: Phase and group velocity dispersion curves for the first two symmetric and anti-symmetric *Lamb* modes in an aluminum plate (see Table A-1; $h_p = 2h$).

With the wavelength $\lambda = c_p/f$ and after some transformations the solution of the group velocity in dependency of the frequency times thickness can be written as [49]

$$c_g = c_p^2 \left(c_p - f \frac{\partial c_p}{\partial f} \right)^{-1} . \tag{2.20}$$

In experiments the group velocity is measurable via the time-of-flight corresponding to a defined distance. This information is important to analyse the sensor data by using a non-continuous signal like a pulse. By measuring the wave length of the *Lamb* wave modes the phase velocity can be determined.

Using Equation (2.14) to determine A_2 and B_1 in Equation (2.10) the displacements u_1 and u_3 of the symmetric mode can be calculated (see Figure 2.3A)

$$
\begin{aligned}
u_1 &= -2k^2 \tilde{q} \cos \tilde{q}h \cos \tilde{p}x_3 + \tilde{q}(k^2 - \tilde{q}^2) \cos \tilde{p}h \cos \tilde{q}x_3, \\
u_3 &= -2jk\tilde{p}\tilde{q} \cos \tilde{q}h \sin \tilde{p}x_3 - jk(k^2 - \tilde{q}^2) \cos \tilde{p}h \sin \tilde{q}x_3 .
\end{aligned}
\tag{2.21}
$$

In an analogous way the displacements u_1 and u_3 of the anti-symmetric mode can be calculated (see Figure 2.3B) using Equation (2.15) to determine A_1 and B_2 in Equation (2.10)

$$
\begin{aligned}
u_1 &= -2k^2 \tilde{q} \sin \tilde{q}h \sin \tilde{p}x_3 + \tilde{q}(k^2 - \tilde{q}^2) \sin \tilde{p}h \sin \tilde{q}x_3, \\
u_3 &= 2jk\tilde{p}\tilde{q} \sin \tilde{q}h \cos \tilde{p}x_3 + jk(k^2 - \tilde{q}^2) \sin \tilde{p}h \cos \tilde{q}x_3 .
\end{aligned}
\tag{2.22}
$$
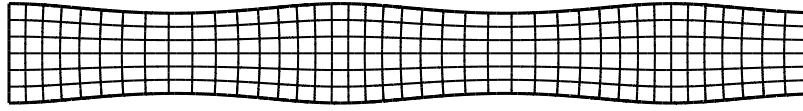
(A) S$_0$-mode
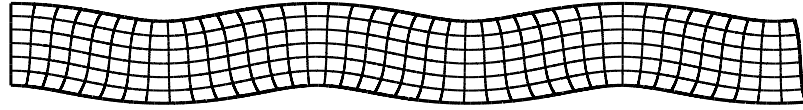
(B) A$_0$-mode

**Figure 2.3:** *Lamb* wave mode shapes.

The corresponding mode shapes (u_1, u_3) for the S$_0$- and A$_0$-mode are illustrated in Figures 2.3. The symmetric mode is comparable to a compression wave, whereas the anti-symmetric mode resembles a flexural wave. The amplitude characteristics of the displacements u_1 and u_3 over the height are influenced by the mode type and the frequency. The shape of the displacements u_1 and u_3 over the plate thickness of the symmetric and the anti-symmetric mode are shown in Figure 2.4. The x-axis corresponds to the normalized displacements, whereas the y-axis corresponds to x_3. The displacements are normalized utilizing the smallest absolute value of $u_1(fh_p)$ or $u_3(fh_p)$, respectively. The frequency times thickness dependency is not equal for both displacements. The normalized u_1-displacement of the S$_0$-mode has a maximum at the midplane Figure 2.4A. This maximum increases at higher frequencies. The u_3-displacement is zero in the midplane shown in Figure 2.4B. For the anti-symmetric mode the u_3-displacement (see Figure 2.4D) is stronger influenced by a change of the frequency times thickness than the u_1-displacement (see Figure 2.4C). The non-linear deformation especially for the u_1-displacement of the S$_0$-mode underlines the need to develop a three-dimensional finite element as done in chapter 3. Moreover, the sensitivity of the modes with different damages at different depths inside structure could be studied. This knowledge is important, e.g. to identify the useful *Lamb* mode for different types of damages if a mono-modal excitation is used for SHM purposes.
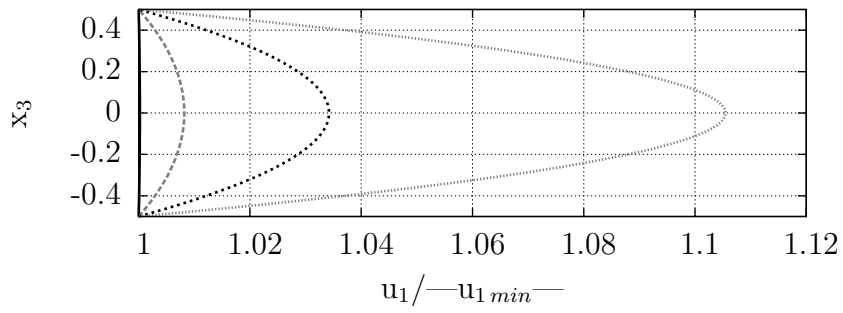
(A) Normalized u_1-displacement of the S_0-mode
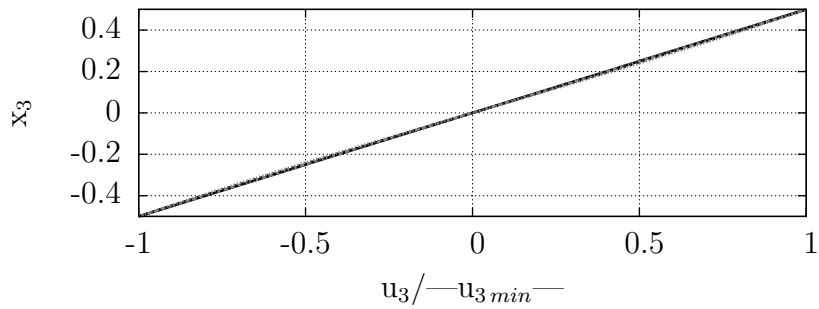
(B) Normalized u_3-displacement of the S_0-mode

(C) Normalized u_1-displacement of the A_0-mode

| 0.1 MHzmm | ——— | 1.1 MHzmm | ············ |
| 0.8 MHzmm | --------- | 1.6 MHzmm | ············ |
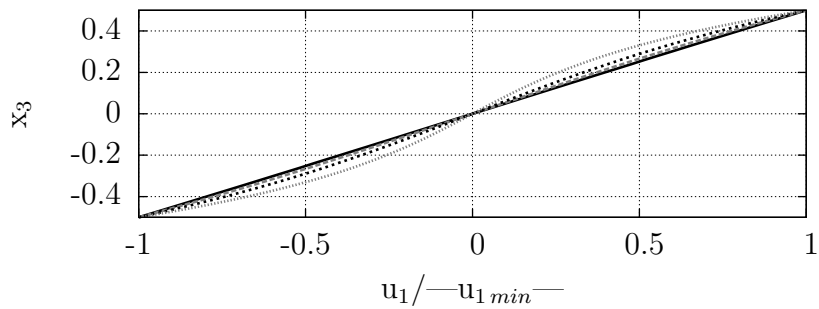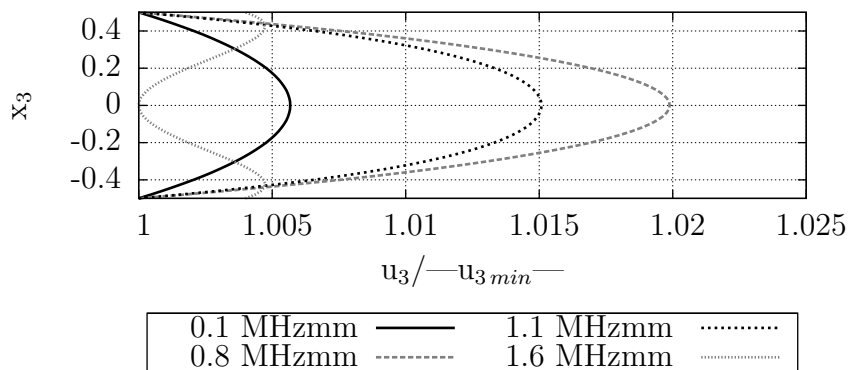
(D) Normalized u_3-displacement of the A_0-mode

Figure 2.4: Normalized displacments over the thickness of the plate of the S_0- and A_0-mode for different frequencies. u_{min} corresponds to the minimal displacement for each fh_p.

2.3 *Lamb* wave excitation

When using *Lamb* waves for structural health monitoring applications one has to be able to excite them as well as to sense them. Different methods for the actuation of *Lamb* waves are possible induced, e.g. by temperature [103], by ultrasonic transducers [144, 155], applied by magneto restrictive patches [50]. However, a commonly used way is to apply piezoceramic patches at the surface of the structure [143] and to use them as actuators and sensors. With piezoelectric strain sensors, strong and clear voltage signals can be obtained directly from the sensor without the need for intermediate gage bridges, signal conditioners, and signal amplifiers. These direct sensing properties are especially significant in dynamics, vibration, and audio applications in which alternating effects occur in rapid succession thus preventing charge leaking [49]. Figure 2.5 illustrates some standard designs of piezoceramics. All of them have different advantages and disadvantages, but they use the piezoelectric effect as physical principle.

(A) Pure piezoceramic

(B) Piezoceramic composite

(C) Piezoelectric flexible thin layer [2]

(D) Piezoelectric fiber [1]
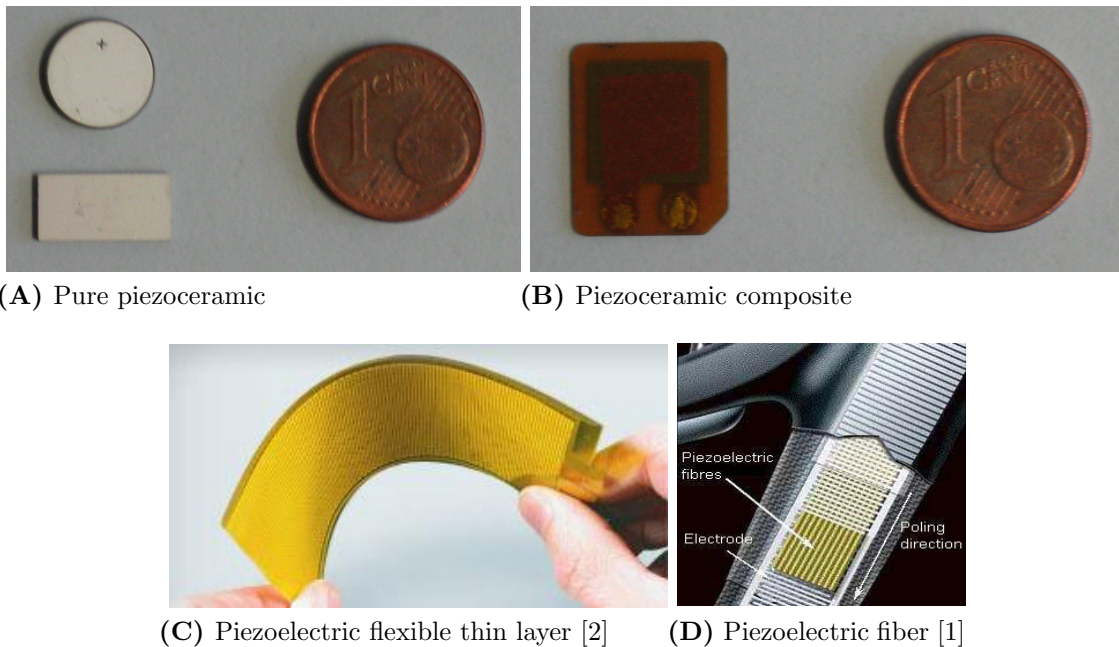
Figure 2.5: Examples of different types of piezoelectric actuators.

2.3.1 Piezoelectric material

The piezoelectric effect was discovered by the brothers Jacques and Pierre Curie in 1880 [71]. Piezoceramics are active materials which transform mechanical deformation into electrical energy (direct piezoelectric effect) as well as electrical energy into mechanical deformation (inverse piezoelectric effect). One ceramic can be used both as actuator and sensor. Therefore, piezoceramics are widely utilized in technical applications, e.g. ultrasonic measurements, medical diagnostics, micro pumps, telephones, etc. [58].

Most of the technological applications of piezoelectricity used nowadays are based on ferroelectric materials. To gain an understanding of the piezoelectric effect in ferroelectric materials, the behavior of the material on a microscopic scale has to be considered. Above

a certain temperature, called *Curie* temperature (T_C), the crystal structure of a ferroelectric material does have a center of symmetry and has therefore no electric dipole moment. A non-symmetric crystal structure is formed below the material specific *Curie* temperature and the crystal presents a natural electric dipole (pyroelectricity) which may be reversed (ferroelectricity) and also switched in certain allowed directions by the application of a sufficiently high electric field [111].
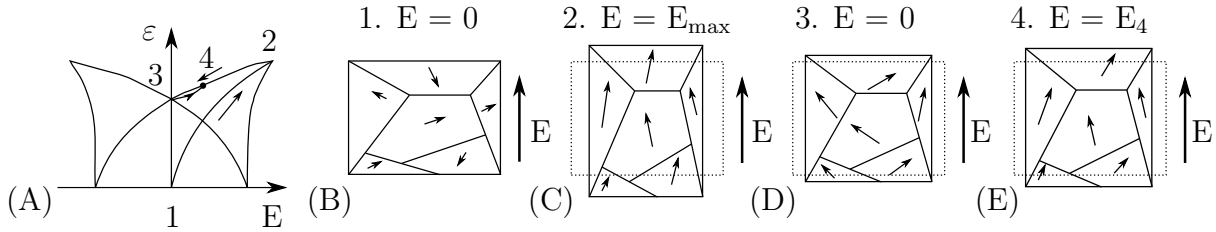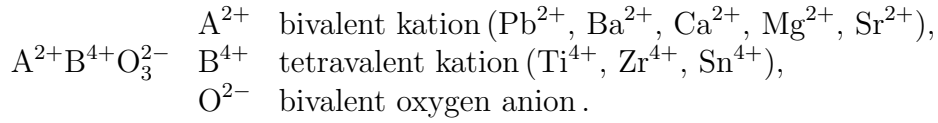

Figure 2.6: Polarization reorientation and strain changes under the influence of external electric field E [95].

Ferroelectric crystals possess regions with uniform polarization called ferroelectric domains. In one domain the electric dipoles have the same orientation. The interfaces which separate the domains are called domain walls. Usually, a ferroelectric material consists of many domains, and all directions of the electric polarization have the same probability of appearance. The overall net electric dipole in the ferroelectric is zero. The term "ferroelectric material" was coined because of an analogy to the term "ferromagnetic materials", in which the remanent magnetization is altered by the application of an external magnetic field [49]. Typically, the polarization is impressed after the production process. The body has become permanently piezoelectric and can convert mechanical energy into electrical energy, and vice versa.

Figure 2.6 schematically shows the polarization process in a multi-domain ferroelectric piezoceramic. The arrows inside the cells correspond to the polarization direction of a single domain. The material is initially randomly poled (Figure 2.6 (B)). An electric field E_{max} is applied. The polarization in each domain orientates to the direction of applied electrical field (Figure 2.6 (C)). As the electric field is reduced, the strain decreases monotonically and no depolarization occurs also if the electric field is set to zero (Figure 2.6 (D)). The material is now poled and has a remanent polarization and remanent strain [111].

Typically the polarization process is done only one time in life of a piezoceramic. After it small electric fields E_4 (Figure 2.6 (D)) are used to activate the piezoceramic. The region between 3 and 4 in the low voltage range is approximately linear. For further investigations it is focussed on this region. The mechanical behavior of the material will be assumed to be linear elastic without dissipation. The laws are valid near the points 3 and 4 in Figure 2.6 (A) [19].

The most representative materials among the displacive ferroelectrics are the perovskites, of which BaTiO$_3$ is a prototype. The lattice structure of Barium titanate is depicted in Figure 2.7. They can be described by the perovskite formula

$$A^{2+}B^{4+}O_3^{2-} \quad \begin{array}{ll} A^{2+} & \text{bivalent kation}\,(Pb^{2+},\,Ba^{2+},\,Ca^{2+},\,Mg^{2+},\,Sr^{2+}), \\ B^{4+} & \text{tetravalent kation}\,(Ti^{4+},\,Zr^{4+},\,Sn^{4+}), \\ O^{2-} & \text{bivalent oxygen anion}\,. \end{array}$$

Below the *Curie* temperature ($T_C \approx 120°C$ [179]) the position of the Ti^{4+} ion is not within the plane of symmetry (dashed horizontal lines). The shift defines the direction of polarization of the single crystal. The application of an electric field moves the Ti^{4+} ion which causes a deformation of the crystal.

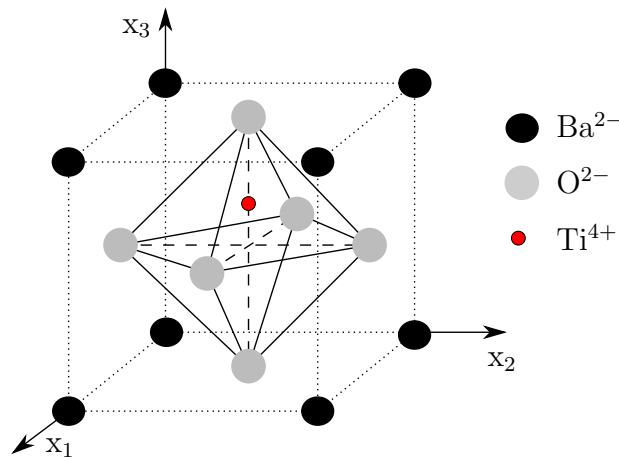**Figure 2.7:** Cubic unit cell of perovskite structure of ABO$_3$ type, for BaTiO$_3$ [95].

2.3.2 Constitutive equations of piezoelectric material

To model a piezoelectric elastic material in a low voltage range, the linearized piezoelectric constitutive equations are sufficient to describe the coupled electro-mechanical behavior [19, 49].
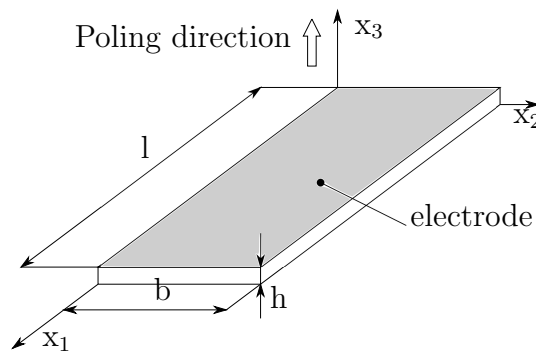

Figure 2.8: Coordinate definition of a piezoceramic patch.

The linearized piezomechanical material law can be written as

$$\boldsymbol{\varepsilon} = \mathbf{S}^E \boldsymbol{\sigma} + \mathbf{d}\mathbf{E}\,, \tag{2.23}$$

$$\mathbf{D} = \mathbf{d}^T \boldsymbol{\sigma} + \boldsymbol{\epsilon}^\sigma \mathbf{E}\,. \tag{2.24}$$

The parameters $\boldsymbol{\sigma}$, $\boldsymbol{\varepsilon}$, $\mathbf{E}$, $\mathbf{D}$, $\mathbf{S}^E$, $\mathbf{d}$ and $\boldsymbol{\epsilon}^\sigma$ are the mechanical stresses, the mechanical strains, the electric field, the electrical displacement, the elastic compliance matrix measured at constant electric field, the piezoelectric coupling matrix and the permittivity measured at constant mechanical stress, respectively. The mechanical strain is related to the displacement $\mathbf{u}$ as $\boldsymbol{\varepsilon} = \boldsymbol{\mathcal{D}}\mathbf{u}$, where

$$\boldsymbol{\mathcal{D}} = \begin{bmatrix} \frac{\partial}{\partial x_1} & 0 & 0 \\ 0 & \frac{\partial}{\partial x_2} & 0 \\ 0 & 0 & \frac{\partial}{\partial x_3} \\ \frac{\partial}{\partial x_3} & 0 & \frac{\partial}{\partial x_1} \\ 0 & \frac{\partial}{\partial x_3} & \frac{\partial}{\partial x_2} \\ \frac{\partial}{\partial x_2} & \frac{\partial}{\partial x_1} & 0 \end{bmatrix}\,, \tag{2.25}$$

is the differential operator. The electric field is defined as the negative gradient of the electrical potential Φ

$$\mathbf{E} = -\mathrm{grad}\Phi = -\begin{bmatrix} \frac{\partial \Phi}{\partial x_1} \\ \frac{\partial \Phi}{\partial x_2} \\ \frac{\partial \Phi}{\partial x_3} \end{bmatrix}\,. \tag{2.26}$$

The extension of *Hooke*s Law to piezoelectric coupling between quasistatic mechanical and electrical variables is represented by the 9 x 9 *Van Dyke* matrix [58]. Assuming transversal isotropic material properties and utilizing the coordinate system shown in Figure 2.8 the constitutive equation can be written as

$$\begin{bmatrix} \varepsilon_1 \\ \varepsilon_2 \\ \varepsilon_3 \\ \varepsilon_4 \\ \varepsilon_5 \\ \varepsilon_6 \\ D_1 \\ D_2 \\ D_3 \end{bmatrix} = \begin{bmatrix} s_{11}^E & s_{12}^E & s_{13}^E & 0 & 0 & 0 & 0 & 0 & d_{31} \\ s_{12}^E & s_{11}^E & s_{13}^E & 0 & 0 & 0 & 0 & 0 & d_{31} \\ s_{13}^E & s_{13}^E & s_{33}^E & 0 & 0 & 0 & 0 & 0 & d_{33} \\ 0 & 0 & 0 & s_{44}^E & 0 & 0 & 0 & d_{15} & 0 \\ 0 & 0 & 0 & 0 & s_{44}^E & 0 & d_{15} & 0 & 0 \\ 0 & 0 & 0 & 0 & 0 & s_{66}^E & 0 & 0 & 0 \\ 0 & 0 & 0 & 0 & d_{15} & 0 & \epsilon_{11}^\sigma & 0 & 0 \\ 0 & 0 & 0 & d_{15} & 0 & 0 & 0 & \epsilon_{11}^\sigma & 0 \\ d_{31} & d_{31} & d_{33} & 0 & 0 & 0 & 0 & 0 & \epsilon_{33}^\sigma \end{bmatrix} \cdot \begin{bmatrix} \sigma_1 \\ \sigma_2 \\ \sigma_3 \\ \sigma_4 \\ \sigma_5 \\ \sigma_6 \\ E_1 \\ E_2 \\ E_3 \end{bmatrix} \tag{2.27}$$

with $s_{66}^E = 2(s_{11}^E - s_{12}^E)$ as shear modulus belonging to the plane of isotropy. The indices $(..)_1$, $(..)_2$, $(..)_3$, $(..)_4$, $(..)_5$ and $(..)_6$ match with the x_1-, x_2-, x_3-, x_{13}-, x_{23}- and x_{12}-direction, respectively.

(A) Electrical field work in direction of the polarization

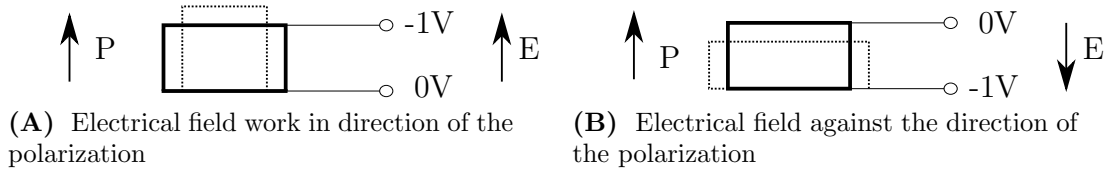**(B)** Electrical field against the direction of the polarization

Figure 2.9: Deformation of piezoceramics under electrical load (black - undeformed, dotted - deformed).

Using a piezoceramic material as actuator an external electrical field has to be applied, e.g. parallel to the polarization of the ceramic. With the knowledge of the direction of polarization, it is possible to predict the occurring deformation. Figure 2.9A illustrates the deformation caused by applying a positive electrical field. Figure 2.9B shows a shrinking, because of a negative electrical field. Equation (2.23) allows us to calculate the strain for both examples. Using the piezoceramic patch as sensor the conversion of mechanical strain to voltage output can be derived. The charge Q and the voltage V_C generated across the sensor electrodes are related by the capacitance C_p of the sensor as

$$V_C = \frac{Q}{C_p} \, . \tag{2.28}$$

According to Sirohi et al. [136] a piezoelectric sheet can be treated as a parallel plate capacitor, with a capacitance given by

$$C_p = \frac{\epsilon_{33}^\sigma \cdot l_C \cdot b_C}{d_C} \, . \tag{2.29}$$

Whereas ϵ_{33}^σ describes the dielectric permittivity in x_3-direction, d_C the height, l_C the length and b_C the width of a cuboid piezoceramic sensor. The electric displacement is related to the generated charge through the expression

$$q = \int_{S_i} \begin{bmatrix} D_1 & D_2 & D_3 \end{bmatrix} \cdot \begin{bmatrix} \mathrm{dS}_1 \\ \mathrm{dS}_2 \\ \mathrm{dS}_3 \end{bmatrix} \tag{2.30}$$

where S_i are surfaces of the capacitor. Incorporating the assumption that the electrical field $\mathbf{E}$ is zero [22, 136] inside a piezoelectric sensor into equation (2.24) the dielectric displacement is given as

$$\begin{bmatrix} D_1 \\ D_2 \\ D_3 \end{bmatrix} = \begin{bmatrix} 0 & 0 & 0 & 0 & d_{15} & 0 \\ 0 & 0 & 0 & d_{15} & 0 & 0 \\ d_{31} & d_{31} & d_{33} & 0 & 0 & 0 \end{bmatrix} \cdot \begin{bmatrix} \sigma_1 \\ \sigma_2 \\ \sigma_3 \\ \sigma_4 \\ \sigma_5 \\ \sigma_6 \end{bmatrix} \, . \tag{2.31}$$

The voltage can be calculated using the equations (2.28) - (2.30). It is noted that shear stress in the 1-2 plane σ_6 is not capable of generating any electric response

$$V_C = \frac{Q}{C_p} = \frac{d_C}{e_{33}^\sigma \cdot l_C \cdot b_C} \cdot \left[\int_b \int_h D_1 \, \mathrm{dx}_2 \, \mathrm{dx}_3 + \int_l \int_h D_2 \, \mathrm{dx}_1 \, \mathrm{dx}_3 + \int_l \int_b D_3 \, \mathrm{dx}_1 \, \mathrm{dx}_2 \right] \, . \tag{2.32}$$

2.4 Finite element method

The finite element method (FEM) is the most widely used method for the simulation of structural problems in engineering. A distinctive feature of the finite element method is the division of a given domain into a set of simple subdomains, called finite elements [125]. For arbitrary problems it is not possible to find functions to describe the solution of the whole domain. The development of the method started in the 1940's with Hrenikoff (1941), Courant (1943), McHenry (1943), Newmark (1949) and others [176]. Until now a large variety of books and articles are published about this topic, e.g. Bathe [11], Hughes [65], Reddy [125], Zienkiewicz and Taylor [176–178], etc. These books are mainly focused on the development of the h-version of the finite elements. The quality of the solution is increased by using a higher number of elements. Nevertheless, the accuracy can be also enhanced by increasing the polynomial order of the ansatz function. Szabò, Babŭska and Düster [43, 145] should be mentioned when talking about the development of the p-version of the finite elements. In 2005 the term "isogeometric" finite elements was coined [66]. The work was motivated by closing the existing gap between the finite element analysis (FEA) and the computer aided-design (CAD) in FEA applications [29]. Using a NURBS-based description of the geometrical model in CAD reduces the effort of the discretization process [45].

Regardless of the proposed approaches the basic finite element equations are equal. In the following sections these equations are given.

2.4.1 Variational principle

The dynamic equations of a piezoelectric continuum can be derived using *Hamilton*s principle, which states that the motion of the system in time interval $[t_1, t_2]$ is such that the variation of action vanishes, i.e. the motion of the system takes the path of stationary action [55]

$$\delta \int_{t_1}^{t_2} (L + W)\,\mathrm{dt} = 0\,, \tag{2.33}$$

where L represents the *Lagrangian*, and δW the virtual work of the external forces. The *Hamilton*s principle is adapted in a way that the *Lagrangian* includes the kinetic energy T as well as the electric enthalpy density function H (electric *Gibbs* energy [68])

$$L = T - H\,. \tag{2.34}$$

The kinetic energy is well known as

$$T = \frac{1}{2} \int_V \rho \dot{\mathbf{u}}^T \dot{\mathbf{u}}\,\mathrm{dV}\,, \tag{2.35}$$

with the mass density ρ and the velocity field $\dot{\mathbf{u}}$. The electric enthalpy density function H is usually used to derive the governing equations of the coupled piezoelectric continuum and for the linear piezoelectric behavior [128]. The potential energy density of a piezoelectric material includes contributions from the strain energy and from the electrostatic energy [111]

$$H = \frac{1}{2} \int_V (\boldsymbol{\varepsilon}^T \boldsymbol{\sigma} - \mathbf{E}^T \mathbf{D})\,\mathrm{dV}\,, \tag{2.36}$$

where $\boldsymbol{\sigma}$ are the mechanical stresses, $\boldsymbol{\varepsilon}$ the mechanical strain, $\mathbf{E}$ the electrical field and $\mathbf{D}$ the dielectrical displacement. Using the Equations (2.35) and (2.36) the *Lagrangian L* can be written as

$$L = \int\limits_V \frac{1}{2} \left[\rho \dot{\mathbf{u}}^T \dot{\mathbf{u}} - \boldsymbol{\varepsilon}^T \boldsymbol{\sigma} - \mathbf{E}^T \mathbf{D} \right] \, \mathrm{dV} \,. \tag{2.37}$$

Following Samal et al [128] the work W done by external mechanical $\mathbf{f}$ forces and electrical charges Q at volumes $(..)_V$, surfaces $(..)_{S_i}$ or nodals $(..)_i$ is given as

$$W = \int\limits_V \mathbf{u}^T \mathbf{f}_V \, \mathrm{dV} + \int\limits_{S_1} \mathbf{u}^T \mathbf{f}_{S_1} \, \mathrm{dS}_1 - \sum_{i=1}^n \mathbf{u}_i^T \mathbf{f}_i - \int\limits_{S_2} \Phi Q_{S_2} \, \mathrm{dS}_2 - \sum_{j=1}^m \Phi_j Q_j \,, \tag{2.38}$$

the variables and the electromechanical analogy is illustrated in Table 2.1.

Table 2.1: Electromechanical analogy.

Mechanical variables		Electrical variables	
Force	$\mathbf{f}$	Charge	Q
Displacement	$\mathbf{u}$	Electric potential	Φ
Stress	$\boldsymbol{\sigma}$	Dielectric displacement	$\mathbf{D}$
Strain	$\boldsymbol{\varepsilon}$	Electric field	$\mathbf{E}$

With *Hooke*s law

$$\boldsymbol{\sigma} = \mathbf{C}^E \boldsymbol{\varepsilon} = \left(\mathbf{S}^E \right)^{-1} \boldsymbol{\varepsilon} \tag{2.39}$$

and substituting the Equations (2.23), (2.24), (2.37) and (2.38) in Equation (2.33) the *Hamilton*s principle is obtained in the following form [95]

$$0 = -\int\limits_V \left[\rho \delta \mathbf{u}^T \ddot{\mathbf{u}} + \delta \boldsymbol{\varepsilon}^T \mathbf{C}^E \boldsymbol{\varepsilon} - \delta \boldsymbol{\varepsilon}^T \mathbf{b}^T \mathbf{E} - \delta \mathbf{E}^T \mathbf{b} \boldsymbol{\varepsilon} - \delta \mathbf{E}^T \boldsymbol{\epsilon}^\sigma \mathbf{E} \right] \, \mathrm{dV}$$
$$+ \int\limits_V \delta \mathbf{u}^T \mathbf{f}_V \, \mathrm{dV} + \int\limits_{S_1} \delta \mathbf{u}^T \mathbf{f}_{S_1} \, \mathrm{dS}_1 + \sum_{i=1}^n \delta \mathbf{u}_i^T \mathbf{f}_i - \int\limits_{S_2} \delta \Phi Q_{S_2} \, \mathrm{dS}_2 - \sum_{j=1}^m \delta \Phi_j Q_j \,, \tag{2.40}$$

where $\ddot{\mathbf{u}}$ is the acceleration and $\mathbf{b} = \mathbf{C}^E \mathbf{d}$.

2.4.2 Finite element equations

Based on Equation (2.40) the finite element equations can be derived. When using the finite element approach a continuous body is approximated with shape functions defined on a local domain (elements). The shape functions will be discussed in the next section (see section 2.5). The displacements $\mathbf{u}^{(m)}$ and the electrical potential $\Phi^{(m)}$ in an element can be expressed as

$$\mathbf{u}^{(m)}(\mathbf{x}) = \mathbf{H}_u^{(m)}(\mathbf{x})\mathbf{U}_\mathrm{N} \quad \text{and} \quad \Phi(\mathbf{x})^{(m)} = \mathbf{H}_\phi^{(m)}(\mathbf{x})\boldsymbol{\phi}_\mathrm{N} \,. \tag{2.41}$$

$\mathbf{H}^{(m)}$ is an interpolation matrix which includes the shape functions. $\mathbf{U}_{\mathrm{N}}$ and $\boldsymbol{\phi}_{\mathrm{N}}$ are the displacement vector and the electrical potential of each node, respectively, m is the element number and $\mathbf{x} = [x_1, x_2, x_3]$ is the position vector [176]. The mechanical strain and the electrical field are defined as $\boldsymbol{\varepsilon} = \boldsymbol{\mathcal{D}}\mathbf{u}$, where $\boldsymbol{\mathcal{D}}$ is the differential operator and $\mathbf{E} = -\boldsymbol{\nabla}\Phi$ (see Section 2.3.2), respectively. With the ansatz shown in Equations (2.41) the element strain and the element electrical field can be derived directly

$$
\begin{aligned}
\boldsymbol{\varepsilon}^{(m)}(\mathbf{x}) &= \boldsymbol{\mathcal{D}}\mathbf{H}_u^{(m)}(\mathbf{x})\mathbf{U}_{\mathrm{N}} = \mathbf{B}_u^{(m)}(\mathbf{x})\mathbf{U}_{\mathrm{N}}\,, \\
\mathbf{E}^{(m)}(\mathbf{x}) &= -\boldsymbol{\nabla}\mathbf{H}_\phi^{(m)}(\mathbf{x})\boldsymbol{\phi}_{\mathrm{N}} = -\mathbf{B}_\phi^{(m)}(\mathbf{x})\boldsymbol{\phi}_{\mathrm{N}}\,.
\end{aligned}
\tag{2.42}
$$

If the approximation of the mechanical displacements (Equation (2.41)) and the strains (Equation (2.42)) as well as relations for the electrical potential and the electrical field is substituted in Equation (2.40) the equations for a dynamic piezomechanical model are obtained as

$$
\begin{aligned}
&\delta\mathbf{U}_{\mathrm{N}}^T \int_V \mathbf{H}_u^{(m)T}\rho\mathbf{H}_u^{(m)}\mathrm{dV}\ddot{\mathbf{U}}_{\mathrm{N}} + \delta\mathbf{U}_{\mathrm{N}}^T \int_V \mathbf{B}_u^{(m)T}\mathbf{C}^E\mathbf{B}_u^{(m)}\mathrm{dV}\mathbf{U}_{\mathrm{N}} \\
&+\delta\mathbf{U}_{\mathrm{N}}^T \int_V \mathbf{B}_u^{(m)T}\mathbf{b}^T\mathbf{B}_\phi^{(m)T}\mathrm{dV}\boldsymbol{\phi}_{\mathrm{N}} + \delta\boldsymbol{\phi}_{\mathrm{N}}^T \int_V \mathbf{B}_\phi^{(m)T}\mathbf{b}\mathbf{B}_u^{(m)T}\mathrm{dV}\mathbf{U}_{\mathrm{N}} \\
&-\delta\boldsymbol{\phi}_{\mathrm{N}}^T \int_V \mathbf{B}_\phi^{(m)T}\boldsymbol{\epsilon}^\sigma\mathbf{B}_\phi^{(m)T}\boldsymbol{\phi}_{\mathrm{N}}\mathrm{dV} = \delta\mathbf{U}_{\mathrm{N}}^T \int_V \mathbf{H}_u^{(m)T}\mathbf{F}_V\mathrm{dV} + \delta\mathbf{U}_{\mathrm{N}}^T \int_{S_1} \mathbf{H}_u^{(m)T}\mathbf{F}_{S_1}\mathrm{dS_1} \\
&+\delta\mathbf{U}_{\mathrm{N}}^T\mathbf{H}_u^{(m)T}\mathbf{F}_P - \delta\boldsymbol{\phi}_{\mathrm{N}}^T \int_{S_2} \mathbf{H}_\phi^{(m)T}q\mathrm{dS_2} - \delta\boldsymbol{\phi}_{\mathrm{N}}^T\mathbf{H}_\phi^{(m)T}\mathbf{Q}\,.
\end{aligned}
\tag{2.43}
$$

Equation (2.43) is valid for any arbitrary variation of the displacements $\delta\mathbf{U}_{\mathrm{N}}$ and the electrical potential $\delta\boldsymbol{\Phi}_{\mathrm{N}}$ and thus yields

$$
\mathbf{M}_{uu}\ddot{\mathbf{U}}_{\mathrm{N}} + \mathbf{K}_{uu}\mathbf{U}_{\mathrm{N}} + \mathbf{K}_{u\phi}\boldsymbol{\phi}_{\mathrm{N}} = \mathbf{f}_{ext}\,,
\tag{2.44a}
$$

$$
\mathbf{K}_{\phi u}\mathbf{U}_{\mathrm{N}} - \mathbf{K}_{\phi\phi}\boldsymbol{\phi}_{\mathrm{N}} = \mathbf{q}_{ext}\,.
\tag{2.44b}
$$

The abbreviations in common use are [51]:

$$
\begin{aligned}
&\text{- the mass matrix} && \mathbf{M}_{uu} = \rho \int_V \mathbf{H}_u^T\mathbf{H}_u\mathrm{dV}, \\
&\text{- the mechanical stiffness matrix} && \mathbf{K}_{uu} = \int_V \mathbf{B}_u^T\mathbf{C}^E\mathbf{B}_u\mathrm{dV}, \\
&\text{- the direct piezoelectric coupling matrix} && \mathbf{K}_{u\phi} = \int_V \mathbf{B}_u^T\mathbf{b}^T\mathbf{B}_\phi\mathrm{dV}, \\
&\text{- the inverse piezoelectric coupling matrix} && \mathbf{K}_{\phi u} = \int_V \mathbf{B}_\phi^T\mathbf{b}\mathbf{B}_u\mathrm{dV}, \\
&\text{- the dielectric stiffness matrix} && \mathbf{K}_{\phi\phi} = -\int_V \mathbf{B}_\phi^T\boldsymbol{\epsilon}^\sigma\mathbf{B}_\phi\mathrm{dV}, \\
&\text{- external mechanical forces} && \mathbf{f}_{ext} = \int_V \mathbf{H}_u^T\mathbf{F}_V\mathrm{dV} + \int_{S_1} \mathbf{H}_u^T\mathbf{F}_{S_1}\mathrm{dS_1} + \mathbf{H}_u^T\mathbf{F}_P, \\
&\text{- the electric charge} && \mathbf{q}_{ext} = -\int_{S_2} \mathbf{H}_\phi^T q\mathrm{dS_2} - \mathbf{H}_\phi^T\mathbf{Q}\,.
\end{aligned}
\tag{2.45}
$$

The indices uu, $\phi\phi$ and $u\phi$ denote the coupling between displacement - displacement, electrical potential - electrical potential and displacement - electrical potential, respectively, and $\mathbf{B}_u$, $\mathbf{B}_\phi$ are the strain-displacement matrix and the electric field-electric potential matrix [51].

The vectors $\mathbf{F}_V$, $\mathbf{F}_{S_1}$ and $\mathbf{F}_P$ contains forces applied to a node (P), a surface (S_1) and a volume (V), whereas the vector $\mathbf{Q}$ and the scalar q are charges applied to a node and a surface (S_2), respectively.

2.5 Non-uniform rational B-splines (NURBS)

In this section the basic principles and definitions of NURBS are explained. They are a widely used tool in computer aided design (CAD). I. J. Schoenberg coined the term "Spline" in 1946 [132]. The name is based on a drawing instrument which helps to interpolate the geometry in a geometrical way. The mathematical description of this instrument is the basic idea of splines [37]. There are different types, e.g. cubic splines, Bézier splines and B-splines. In the mathematical subfield of numerical analysis, a B-spline is a spline function that has minimal support with respect to a given degree, smoothness, and domain partition. A fundamental theorem states that every spline function of a given degree, smoothness, and domain partition can be represented as a linear combination of B-splines of that same degree and smoothness, and over that same partition [38].

The first published works on NURBS are from Versprille [154] and Tiller [149]. NURBS are a superset of all non-rational B-splines and non-rational Bèzier curves, surfaces and volumes. NURBS can be interpreted as projection of a B-spline from $\mathbb{R}^{n+1}$ in $\mathbb{R}^n$. For B-splines as well as NURBS a local control of the created polynomial curve is feasible, which make them attractive for CAD applications.

The NURBS functions are used as shape functions for the proposed finite piezomechanical element. The advantage are the exact description of the geometry and the smooth continuity over the element boundary [66].

2.5.1 One-dimensional B-spline

A B-spline basis is comprised of piece-wise polynomials joined with prescribed continuity. To define a B-spline of polynomial order p_{x_1} in one dimension one needs to understand the notion of a knot vector $\mathbf{V}$. A knot vector is a set of coordinates in a parametric space, written as

$$\mathbf{V} = [\beta_0,\ \beta_1,\ \beta_2,\ ..,\ \beta_{r-2},\ \beta_{r-1}] \quad \text{with} \quad \beta_i \le \beta_{i+1}\,, \tag{2.46}$$

where i is the knot index, $i = 0,\ 1,\ 2,\ ...,\ r - 1$, β_i is the ith knot, $r = n_{cont} + p_{x_1} + 1$ is the length of the knot vector and n_{cont} the total number of control points [12]. There are various ways to define B-spline basis functions, e.g. by blossoming [45, 87], by divided differences of truncated power functions [33, 132] and by recurrence formulae [32, 36]. For computer implementation the usage of the last possibility is the most useful way and therefore illustrated.

The first order B-spline basis functions $N(\beta)_{i,0}$ of polynomial order $p = 0$ are

$$N_{i,0}(\beta) = \begin{cases} 1, & \beta \in [\beta_i,\ \beta_{i+1}) \\ 0 \end{cases} \quad . \tag{2.47}$$

The B-spline basis functions $N_{i,p_{x_1}}(\beta)$ of higher order $p_{x_1} > 0$ are defined as [20]

$$N_{i,p_{x_1}}(\beta) = \frac{\beta - \beta_i}{\beta_{i+p_{x_1}} - \beta_i} N_{i,p_{x_1}-1}(\beta) + \frac{\beta_{i+p_{x_1}+1} - \beta}{\beta_{i+p+1} - \beta_{i+1}} N_{i+1,p_{x_1}-1}(\beta)\,, \frac{0}{0} \stackrel{def}{=} 0. \tag{2.48}$$

Figure 2.10 illustrates how higher order B-spline basis functions are created. Two B-spline basis functions of polynomial order p_{x_1} define the $(p_{x_1} + 1)$-B-spline basis function, e.g. two "triangles" of $N(\beta)_{i,1}$ define one dotted gray B-spline curve $N(\beta)_{i,2}$. Basis functions of

order p have $p-1$ continuous derivatives at the knots. Repeating a knot j times the number of continuous derivatives decreases by the same number j. If j is equal to the polynomial order p_{x_1} the B-spline becomes interpolatory (C^0-continuous) [112]. Basis functions form a partition of unity, each one is compactly supported on the interval $[\beta_i,\ \beta_{i+p_{x_1}+1}]$, and they are point-wise non-negative. Moreover, the sum of all function values at each knot value β is equal to one

$$\sum_{i=1}^{n_{cont}} N_{i,p_{x_1}}(\beta) = 1\,. \tag{2.49}$$

These properties make these functions attractive for use in analysis [9, 12].
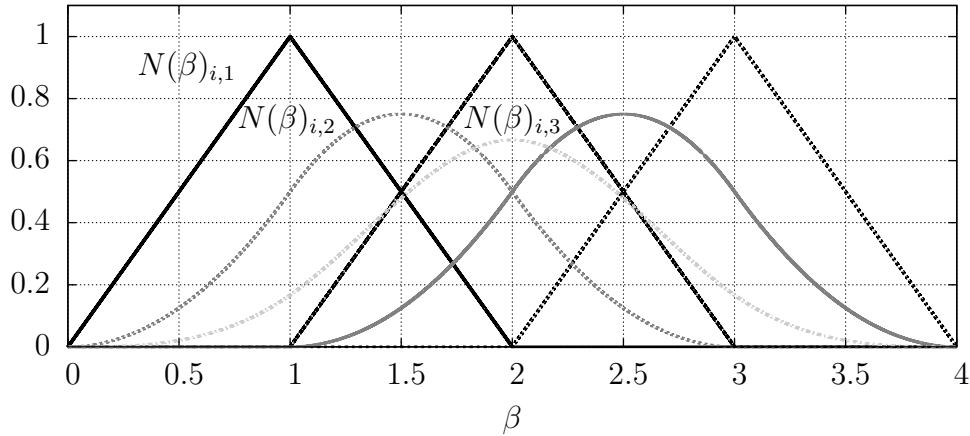

Figure 2.10: B-Spline basis functions $N(\beta)_{i,p_{x_1}}$ of different order p_{x_1} for $\mathbf{V} = [0,\ 1,\ 2,\ 3,\ 4]$.

2.5.2 Geometric approximation with B-splines

B-spline basis functions are used to describe curves, surfaces or volumes. A B-spline curve can be represented as

$$\mathbf{BC}(\beta) = \sum_{i=1}^{n_{cont}} \mathbf{N}_{i,p_{x_1}}(\beta)\mathbf{P}_i \quad \text{with} \quad \beta_0 \leq \beta \leq \beta_{n_{cont}+p+1}\,. \tag{2.50}$$

Where n_{cont} is the number of control points $\mathbf{P}_i$ and $\mathbf{N}_{i,p_{x_1}}(\beta)$ the piece-wise polynomial B-spline basis functions [112].
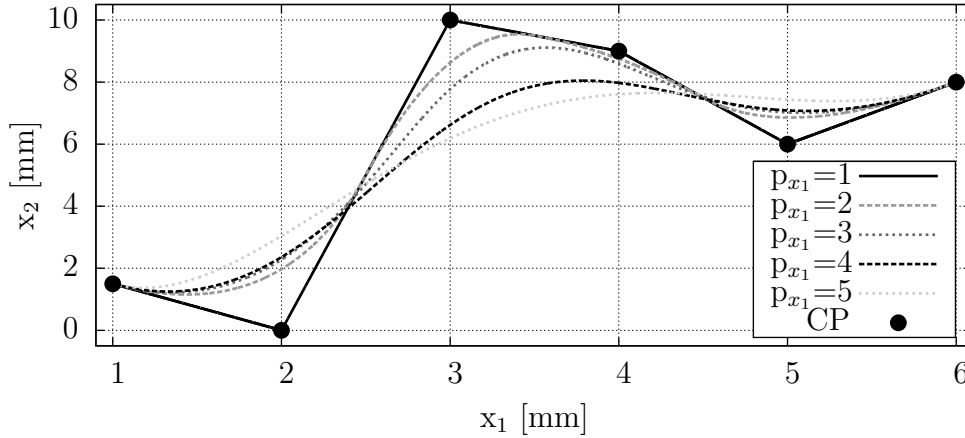
Figure 2.11: B-spline curves with different orders. The curve for $p_{x_1} = 1$ is equal to the control polygon (CP). The continuity between the polynomial curves and the smoothness increases with rising polynomial order.

It can be seen that control points can be located outside the curve. The shape of the curve in relation to the control points is influenced by the knot vector and the order of the polynomial. A reduction of continuity (reducing the order of p, or repeating a knot) shifts the curve more nearer to the control point. If C^0-continuity is reached the control point is interpolated by the curve.

In Figure 2.11 a so called open B-spline is used. The first and the last control point is interpolated. Therefore, the knot vector must be developed as

$$
\begin{aligned}
\beta_i &= \beta_0, & i &\leq p + 1, \\
\beta_{i+1} - \beta_i &\geq 0, & p_{x_1} &< i < n_{cont} + 1, \\
\beta_i &= \beta_{n_{cont}+p+1}, & i &\geq n_{cont} + 1 \,.
\end{aligned}
\tag{2.51}
$$

The Figures 2.12C and 2.12D show examples of an open uniform and open non-uniform B-spline. These types of B-spline are useful for FEM applications. The influence of the knot vector to the shape of the curve is shown in Figure 2.13. For the sake of completeness, the uniform and the non-uniform B-splines are plotted in Figure 2.12A - 2.12B.
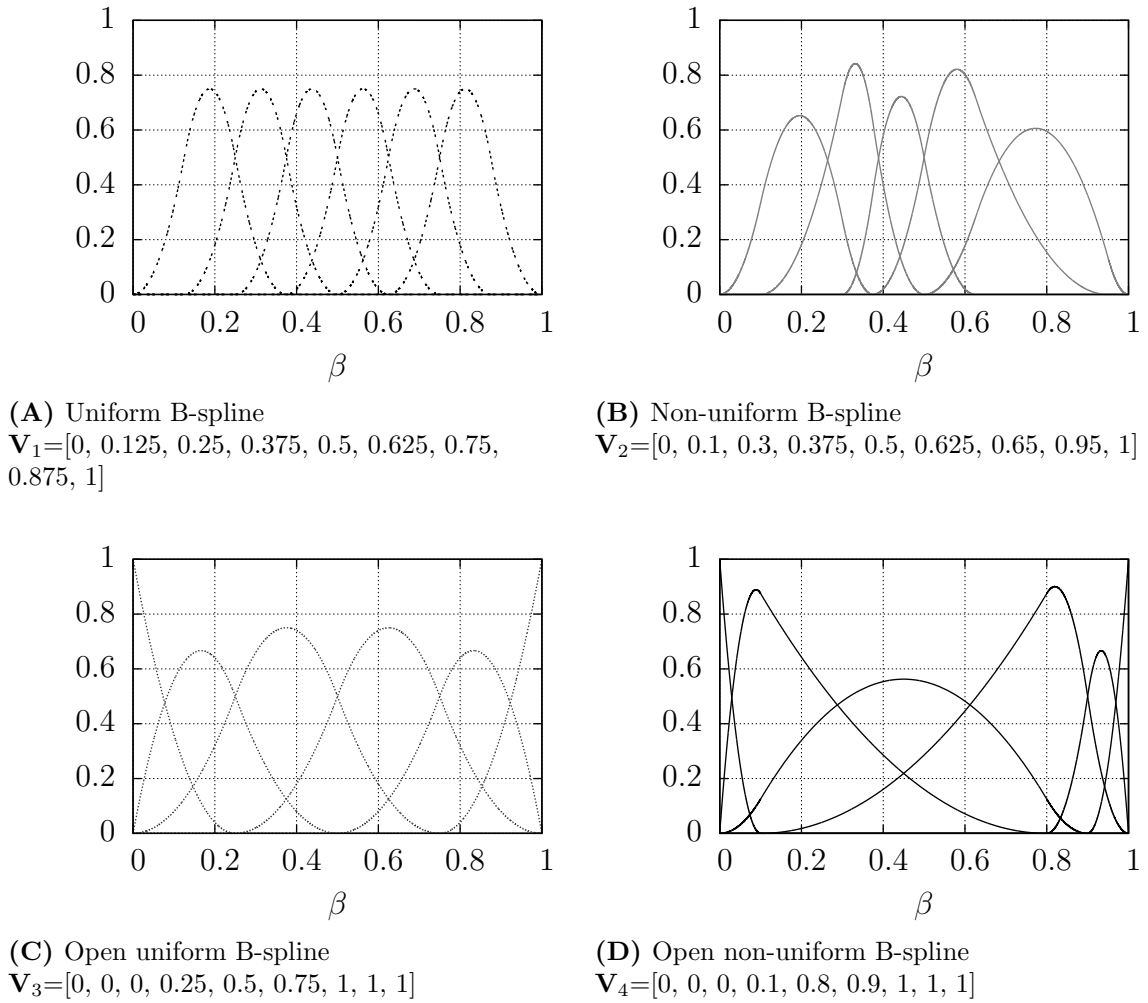
(A) Uniform B-spline
$\mathbf{V}_1$=[0, 0.125, 0.25, 0.375, 0.5, 0.625, 0.75, 0.875, 1]

(B) Non-uniform B-spline
$\mathbf{V}_2$=[0, 0.1, 0.3, 0.375, 0.5, 0.625, 0.65, 0.95, 1]

(C) Open uniform B-spline
$\mathbf{V}_3$=[0, 0, 0, 0.25, 0.5, 0.75, 1, 1, 1]

(D) Open non-uniform B-spline
$\mathbf{V}_4$=[0, 0, 0, 0.1, 0.8, 0.9, 1, 1, 1]

Figure 2.12: Influence on the basis functions of polynomial order $p_{x_1} = 2$ by the variation of the entry of the knots in $\mathbf{V}$.
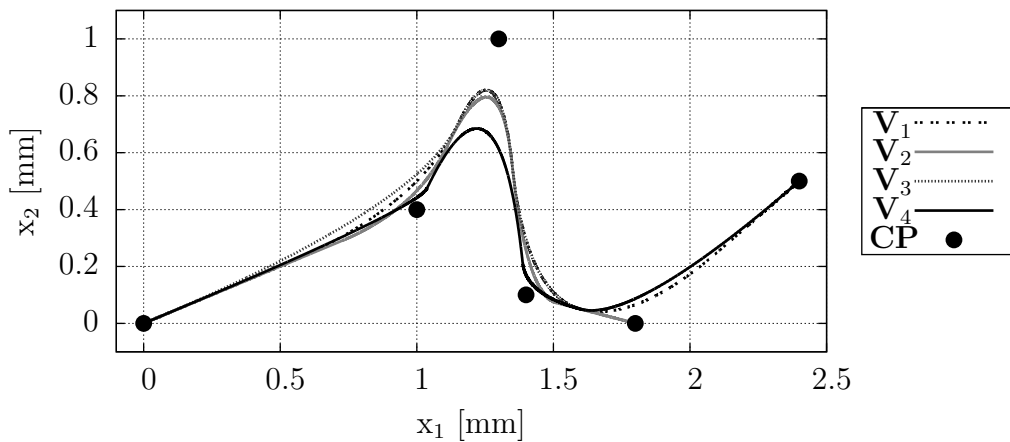

Figure 2.13: Influence of the entries of the knot vector $\mathbf{V}_{1..4}$ to B-spline curves of polynomial order $p_{x_1} = 2$ utilizing equal control points $\mathbf{CP}$. The B-spline basis functions are plotted in Figure 2.12.

2.5.3 Derivatives of a B-spline basis function and B-spline curve

The derivative of an arbitrary basis function is given by [112]

$$N'_{i,p_{x_1}}(\beta) = \frac{p_{x_1}}{\beta_{i+p_{x_1}} - \beta_i} N_{i,p_{x_1}-1}(\beta) - \frac{p_{x_1}}{\beta_{i+p_{x_1}+1} - \beta_{i+1}} N_{i+1,p_{x_1}-1}(\beta) \,. \tag{2.52}$$

In general terms the k-th derivative can be written as

$$N^{(k)}_{i,p_{x_1}}(\beta) = p_{x_1} \left(\frac{N^{(k-1)}_{i,p_{x_1}-1}}{\beta_{i+p_{x_1}} - \beta_i} - \frac{N^{(k-1)}_{i+1,p_{x_1}-1}}{\beta_{i+p_{x_1}+1} - \beta_{i+1}} \right) \,. \tag{2.53}$$

To calculate the derivative of a B-spline curve with respect to β Equation (2.53) can be inserted in Equation (2.50). The k-th derivative of a B-spline curve is defined as

$$\frac{\partial^k}{\partial \beta^k} \mathbf{BC} = \mathbf{BC}^{(k)}(\beta) = \sum_{i=1}^{n_{cont}} N^{(k)}_{i,p_{x_1}}(\beta) \mathbf{P}_i \,. \tag{2.54}$$

2.5.4 Surface or volume approximations using B-splines

Applying the curve description is not enough for creating a finite element in two or three dimensions. Thus, surface and volume interpolations are needed. A B-spline surface is obtained by taking a bidirectional net of control points $\mathbf{P}_{i,j}$, two knot vectors (with knots β, γ), and the products of the univariate B-spline functions of polynomial order p_{x_1} and p_{x_2} ($N_{i,p_{x_1}}$, $M_{j,p_{x_2}}$) [112]. For a B-spline volume the net of control points as well as the knot vectors are augmented with a third direction. The B-spline surface $\mathbf{BS}$ can be generated using

$$\mathbf{BS}(\beta,\gamma) = \sum_{i=1}^{n_{cont}} \sum_{j=1}^{m_{cont}} N_{i,p_{x_1}}(\beta) M_{j,p_{x_2}}(\gamma) \mathbf{P}_{i,j} \,, \tag{2.55}$$

and the B-spline volume $\mathbf{BV}$ given by

$$\mathbf{BV}(\beta,\gamma,\zeta) = \sum_{i=1}^{n_{cont}} \sum_{j=1}^{m_{cont}} \sum_{k=1}^{o_{cont}} N_{i,p_{x_1}}(\beta) M_{j,p_{x_2}}(\gamma) O_{k,p_{x_3}}(\zeta) \mathbf{P}_{i,j,k} \,. \tag{2.56}$$

The derivatives of both B-spline surface and volume can be written as

$$\frac{\partial^{u+v}}{\partial \beta^u \partial \gamma^v} \mathbf{BS}(\beta,\gamma) = \sum_{i=1}^{n_{cont}} \sum_{j=1}^{m_{cont}} N^{(u)}_{i,p_{x_1}}(\beta) M^{(v)}_{j,p_{x_2}}(\gamma) \mathbf{P}_{i,j} \,, \tag{2.57}$$

and

$$\frac{\partial^{u+v+w}}{\partial \beta^u \partial \gamma^v \partial \zeta^w} \mathbf{BV}(\beta,\gamma,\zeta) = \sum_{i=1}^{n_{cont}} \sum_{j=1}^{m_{cont}} \sum_{k=1}^{o_{cont}} N^{(u)}_{i,p_{x_1}}(\beta) M^{(v)}_{j,p_{x_2}}(\gamma) O^{(w)}_{k,p_{x_3}}(\zeta) \mathbf{P}_{i,j,k} \,. \tag{2.58}$$

The derivatives of the univariate B-spline functions can be calculated separately for each knot direction (β, γ, ζ) using Equation (2.53).

2.5.5 Rational B-spline curves, surfaces and volumes

As mentioned before a NURBS curve can be interpreted as the projection of a B-spline curve from $\mathbb{R}^{n+1}$ on a defined surface in $\mathbb{R}^n$, illustrated in Figure 2.14A. NURBS are projective invariant and if the weights are non-negative the curve lies in the convex hull of the control polygon. This projection is controlled by weight parameters w_i.
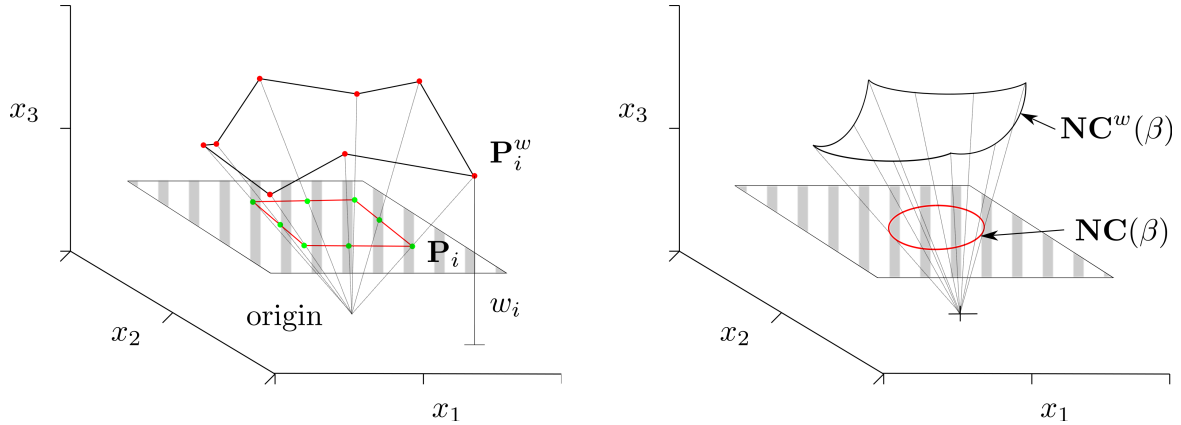
(A) Projective transformation of "projective control point" $\mathbf{P}_i^w$ yields control point $\mathbf{P}_i$. The weight w_i is the x_3-component of $\mathbf{P}_i^w$

(B) Projective transformation of the B-spline curve $\mathbf{NC}^w(\beta)$ yields NURBS curve $\mathbf{NC}(\beta)$

Figure 2.14: Example for a creation of a NURBS curve. A NURBS curve in $\mathbb{R}^2$ is constructed by the projective transformation of a B-spline in $\mathbb{R}^3$ [29].

Depending on the weights an improved geometry approximation can be achieved, e.g. exact description of a circle. The NURBS basis functions $R_{i,p_{x_1}}$ of polynomial order p_{x_1} are defined via the B-spline basis functions $N_{i,p_{x_1}}$ and weights w_i as

$$R_{i,p_{x_1}}(\beta) = \frac{N_{i,p_{x_1}}(\beta)w_i}{\sum\limits_{j=1}^{n_{cont}} N_{j,p_{x_1}}(\beta)w_j} \, . \tag{2.59}$$

The NURBS curve is given as [29]

$$\mathbf{NC}(\beta) = \sum_{i=1}^{n_{cont}} R_{i,p_{x_1}}(\beta)\mathbf{P}_i \, . \tag{2.60}$$

The definition of the derivative of a NURBS curve $\mathbf{NC}'(\beta)$ is quite similar to the derivative of a B-spline curve [112] and can be written as

$$\mathbf{NC}'(\beta) = \sum_{i=1}^{n_{cont}} R'_{i,p_{x_1}}(\beta)\mathbf{P}_i \, . \tag{2.61}$$

The derivative of $R_{i,p_{x_1}}(\beta)$ can be determined utilizing the given as quotient rule [29]

$$R'_{i,p_{x_1}}(\beta) = w_i \frac{W(\beta)N'_{i,p_{x_1}}(\beta) - W'(\beta)N_{i,p_{x_1}}}{W(\beta)^2} \, , \tag{2.62}$$

with

$$W(\beta) = \sum_{j=1}^{n_{cont}} N_{j,p_{x_1}}(\beta)w_j \, .$$

(2.63)

Analogous to a B-spline surface and volume a NURBS surface and volume and their derivatives can be derived. The equations are given in appendix B.

2.5.6 Refinement strategies

In the finite element method refinements of the model are important to reach a converged solution. Typically two different approaches are used to achieve convergence. The first one increases the number of degrees-of-freedom by using a finer discritization (h-refinement). The second one elevates the order of the polynomials (p-refinement). Both refinements result in a better approximation of the underlying mathematical problem. In isogeometric analysis a third method, the increase of the continuity between adjacent finite elements (k-refinement) is described [29, 30, 66]. In this section the algorithms to calculate new control points and weights are presented. These methods are needed to realize the required accuracy of the finite element solution. Table 2.2 gives an overview about the implemented methods.

Table 2.2: Different methods of refinement.

Refinement	Method	Example
h-refinement	increasing the number of control points	Figure 2.15A to 2.15B
p-refinement	increasing the polynomial order between two knots	Figure 2.15B to 2.15D
k-refinement	increasing the polynomial order and the continuity between two knots	Figures 2.15A to 2.15C to 2.15E

In Figures 2.15A and 2.15B a typical h-refinement is performed by inserting an extra knot ($\beta_3 = 0.5$). The polynomial order does not change, but the degrees-of-freedom are increased. The Figures 2.15B and 2.15D illustrate a p-refinement. The polynomial order increases but only C^0-continuity is obtained at the knot boundary shown in Figure 2.15D, because of the double entry $\beta_3 = \beta_4 = 0.5$.

The Figures 2.15A, 2.15C and 2.15E show a k-refinement strategy. The order of the polynomial is elevated and then the knot vector is refined. It must be noted that the knot vector after the k-refinement has less knots compared to a p-refinement achieving the same accuracy [13]. This results in a reduction of the degrees-of-freedom, compared to the other refinement strategies using NURBS as shape functions for finite elements. It must be noted that the p-refinement and the k-refinement schemes are equal if the strategies are applied to a single finite element.
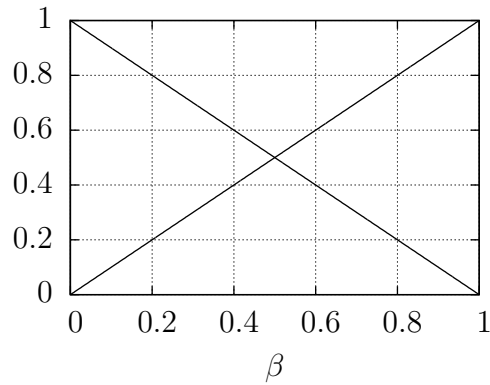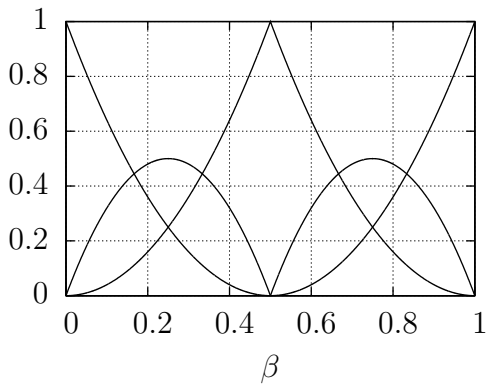
(A) Linear B-spline basis function
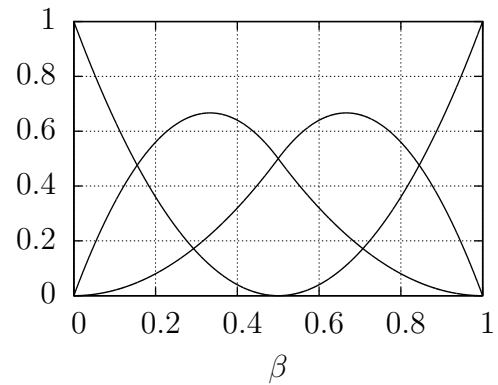$\mathbf{V}_{Knot} = [0, 0, 1, 1]$
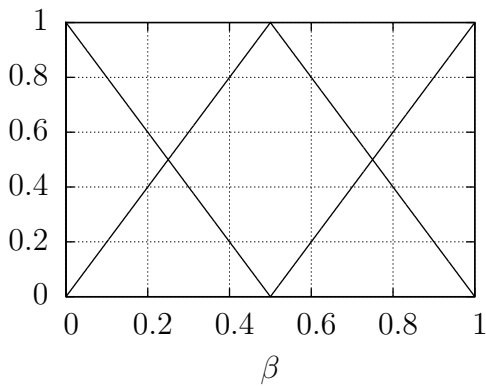
(B) h-refinement
$\mathbf{V}_{Knot} = [0, 0, 0.5, 1, 1]$
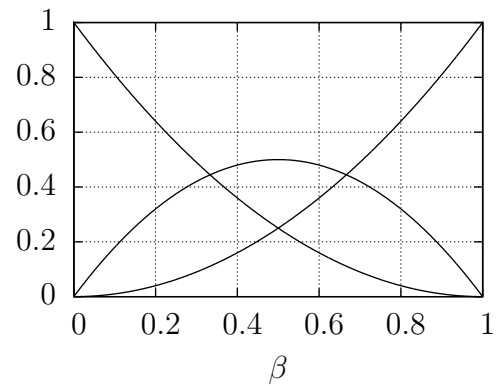
(C) p-refinement
$\mathbf{V}_{Knot} = [0, 0, 0, 1, 1, 1]$

(D) p-refinement
$\mathbf{V}_{Knot} = [0, 0, 0, 0.5, 0.5, 1, 1, 1]$

(E) k-refinement
$\mathbf{V}_{Knot} = [0, 0, 0, 0.5, 1, 1, 1]$

Figure 2.15: Refinement methods of NURBS elements.

The insertion of a knot or the increase of the polynomial order changes the NURBS basis functions. A set of new control points and weights to obtain an equal geometric approximation is needed. The knot insertion of an h-refinement and a p-refinement for a NURBS curve is typically done by converting the given NURBS curve in three dimensions to a B-spline curve in four dimensions (4D). There the knot insertion (or polynomial order el-

evation) is performed and the new curve is projected back in the three-dimensional space. Exemplarily the algorithm is explained in Figure 2.14. If a knot should be inserted the 2D curve $\mathbf{NC}(\beta)$ must be projected to the 3D curve $\mathbf{NC}^w(\beta)$. There the new set of control points is calculated. Using new weights an identical geometry approximation can be realized with a higher number of control points. Let $\mathbf{P}_i(^ix_1, {}^ix_2, {}^ix_3)$ be the control points in 3D, then the control points in 4D are $w_i\mathbf{P}_i(^ix_1, {}^ix_2, {}^ix_3)$. Thus the new control point $\mathbf{P}_i^{new}$ is calculated as follows [26, 118]

$$\mathbf{P}_i^{new} = \frac{(1 - \alpha_i^h)w_{i-1}\mathbf{P}_{i-1} + \alpha_i^h w_i \mathbf{P}_i}{w_i^{new}}, \tag{2.64}$$

with

$$\alpha_i^h = \begin{cases} 1, & 1 \leq i \leq k - p \\ \frac{\overline{\beta} - \beta_i}{\beta_{i+p} - \beta_i}, & k - p + 1 \leq i \leq k \\ 0, & k + 1 \leq i \leq n + p + 2, \end{cases} \tag{2.65}$$

where the knot $\overline{\beta}$ lies within the knot span $[\beta_k, \beta_{k+1}]$ [66]. With the factor α_i^h the new weights w_i^{new} of the NURBS interpolated geometry are calculated by applying

$$w_i^{new} = (1 - \alpha_i^h)w_{i-1} + \alpha_i^h w_i. \tag{2.66}$$

Following Piegl [112] the new control points can be determined by increasing the polynomial order in an analogous way. With the factor α_i^p

$$\alpha_i^p = \frac{i}{p_{x_1} + 1} \quad i = 0, ..., p_{x_1} + 1, \tag{2.67}$$

and the new weights

$$w_i^{new} = \alpha_i^p w_{i-1} + (1 - \alpha_i^p)w_i. \tag{2.68}$$

The new control point $\mathbf{P}_i^{new}$ can be estimated

$$\mathbf{P}_i^{new} = \frac{\alpha_i^p w_{i-1}\mathbf{P}_{i-1} + (1 - \alpha_i^p)w_i\mathbf{P}_i}{w_i^{new}}. \tag{2.69}$$

2.6 Summary

In this chapter the analytical solution of *Lamb*s problem has been developed. It must be noted only waves decoupled from the shear horizontal waves can be called *Lamb* waves, as originally described by *Lamb* [4]. However, in the available literature and in this thesis, waves in anisotropic composite plates are also named as *Lamb* waves even with the coupling. The dispersion curves of a specific isotropic material could be determined applying the mathematical description. However, the analytical approach is limited to simple geometries. The excitation of the *Lamb* waves has to be modeled by applying forces. To investigate and to design real SHM applications one needs actuators and sensors as well as a mathematical description which allows to model these devices and complex structures. Therefore, the piezoelectric material has been introduced. The actuators are used to excite *Lamb* waves. To model complex geometries as well as the piezoelectric actuator or sensor, the finite element method was introduced. The basic equations for a dynamic piezoelectric

finite element have been derived. To develop the element one needs shape functions which describe the domain of the finite element. In this thesis non-uniform rational B-splines are used as shape functions. The geometrical description, properties, refinement strategies, derivatives, etc. have been illustrated.

In the following chapter 3 the introduced general piezoelectric finite element and the NURBS functions are combined to develop an isogeometric element. This element is tested with help several benchmarks.

In chapter 4 the group velocity of an aluminum plate obtained by the analytical model is used as an exact model solution to compare the convergence rate of different higher order finite element approaches.

3 Development of a 3D piezomechanical isogeometric finite element

3.1 Introduction

In chapter 1 it has been mentioned that the simulation of ultrasonic *Lamb* wave propagation is a highly demanding task from a computational point of view. Since high frequencies are required and thus, the wavelength is rather short in comparison to the spatial dimensions considered, the spatial discretization as well as the temporal one have to be very fine when FEM procedures are considered. Due to the fact that conventional low order finite elements quickly reach their limit when dealing with ultrasonic guided waves, an alternative discretization approach is studied. In this chapter a three-dimensional coupled electromechanical isogeometric finite element is developed. This element can be used to model the structure and the piezoceramic actuators and the sensors of a *Lamb* wave based SHM system. It is expected that the structures to be monitored are of complex geometry, e.g. aircraft fuselages, rotor blades of helicopters, etc. For this reason, it is advantageous to use NURBS as shape functions.
In the first part of the chapter the element formulation is developed. Next, static and dynamic benchmarks are applied to test the finite element. In the third part the locking phenomenon is studied. The knowledge gained in this chapter is used in chapter 5.3 to investigate the adhesive layer to determine a critical limit for the element aspect ratio.

3.2 Isogeometric analysis

The principles to develop a piezoelectric finite element are given in section 2.4.2. For isogeometric finite elements the geometry is described as in standard finite elements with a node vector (control points) multiplied by a matrix of interpolation functions (NURBS basis functions)

$$\mathbf{x} = \sum_{i=1}^{n_{el}} \sum_{j=1}^{m_{el}} \sum_{k=1}^{o_{el}} R_{i,j,k}^{p_{x_1}, p_{x_2}, p_{x_3}}(\beta, \gamma, \zeta) \mathbf{P}_{i,j,k}^{(m)} \tag{3.1}$$

with $\mathbf{P}^{(m)}$ as the element control points and $R_{i,j,k}^{p_{x_1}, p_{x_2}, p_{x_3}}$ as NURBS basis functions which are defined in appendix B. Here p_{x_1}, p_{x_2} and p_{x_3} are the polynomial orders of the NURBS basis function in $[\beta, \gamma, \zeta]$-direction in knot space. In contrast to standard finite elements the degrees-of-freedom of NURBS based isogeometric finite elements have no physical meaning. The displacements of the geometry $\mathbf{u}$ and the electric potential ϕ in one element can be

expressed as [152]

$$\mathbf{u} = \sum_{i=1}^{n_{cont}} \sum_{j=1}^{m_{cont}} \sum_{k=1}^{o_{cont}} R_{i,j,k}^{p_{x_1},p_{x_2},p_{x_3}}(\beta,\,\gamma,\,\zeta)\mathbf{U}_{i,j,k}^{(m)} \tag{3.2}$$

and

$$\phi = \sum_{i=1}^{n_{cont}} \sum_{j=1}^{m_{cont}} \sum_{k=1}^{o_{cont}} R_{i,j,k}^{p_{x_1},p_{x_2},p_{x_3}}(\beta,\,\gamma,\,\zeta)\Phi_{i,j,k}^{(m)}. \tag{3.3}$$

Here $\mathbf{U}^{(el)}$ and $\Phi^{(el)}$ are the displacements and the electric potential of the element control points $\mathbf{P}^{(el)}$. The results of the simulation are the time the movement of the control points from which the displacements at the related geometry can be derived. Defining a NURBS element it is started from

$$\mathbf{u} = \mathbf{H}_u^{(m)}\mathbf{U}^{(m)} \qquad \text{and} \qquad \phi = \mathbf{H}_\phi^{(m)}\Phi^{(m)}. \tag{3.4}$$

The interpolation matrices $\mathbf{H}_u^{(m)}$ and $\mathbf{H}_\phi^{(m)}$ for one element are defined as

$$\mathbf{H}_u^{(m)} = \begin{bmatrix} N_1 & 0 & 0 & N_2 & 0 & 0 & & N_{el} & 0 & 0 \\ 0 & N_1 & 0 & 0 & N_2 & 0 & \cdots & 0 & N_{el} & 0 \\ 0 & 0 & N_1 & 0 & 0 & N_2 & & 0 & 0 & N_{el} \end{bmatrix} \tag{3.5}$$

and

$$\mathbf{H}_\phi^{(m)} = \begin{bmatrix} N_1 & N_2 & \cdots & N_{el} \end{bmatrix}. \tag{3.6}$$

There the abbreviations N_i are defined as follows

$$\begin{aligned} N_1 &= R_{(1,1,1)}^{p_{x_1},p_{x_2},p_{x_3}}, \\ N_2 &= R_{(2,1,1)}^{p_{x_1},p_{x_2},p_{x_3}}, \\ N_{k+(l-1)(p_{x_1}+1)+(m-1)(p_{x_1}+1)(p_{x_2}+1)} &= R_{(k,l,m)}^{p_{x_1},p_{x_2},p_{x_3}} \qquad \text{with} \quad k,l,m = 1,\ldots,p_{x_i}+1, \\ N_{el} &= R_{p_{x_1}+1,p_{x_2}+1,p_{x_3}+1}^{p_{x_1},p_{x_2},p_{x_3}}, \end{aligned} \tag{3.7}$$

where el is the number of element control points. As illustrated in section 2.4.2 the NURBS basis functions $R_{i,j,k}^{p_{x_1},p_{x_2},p_{x_3}}$ of order $(p_{x_1},p_{x_2},p_{x_3})$ are defined in the parameter knot space $[\beta,\gamma,\zeta]$. For the numerical implementation one has to map the coordinates between the cartesian and the knot space and from there to the integration domain [21]. Figure 3.1 exemplarily displays the procedure for a two-dimensional example. The element domain Ω^e in the cartesian space is transformed to the parametric knot space $\overline{\Omega}^e$. The mapped parametric domain $\overline{\Omega}^e$ has to be transformed in the local coordinate space $\tilde{\Omega}^e$. There the quadrature is executed on the domain $\tilde{\Omega}^e$.
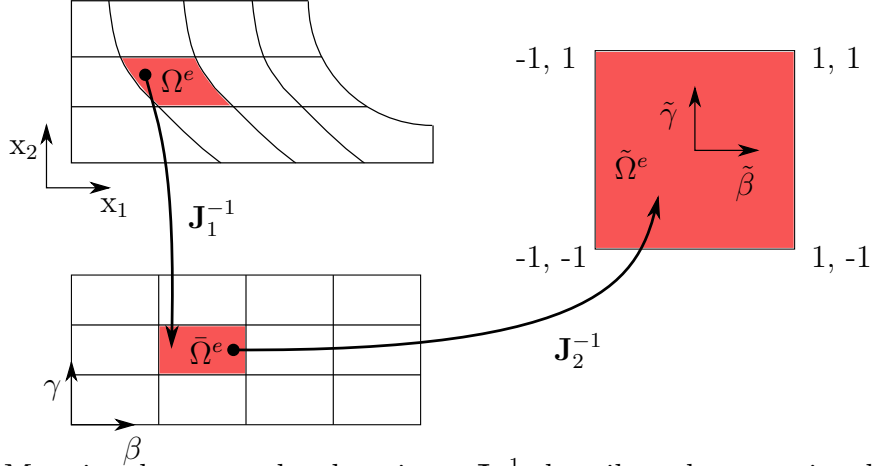
Figure 3.1: Mapping between the domains. $\mathbf{J}_1^{-1}$ describes the mapping between the geometry and the knot coordinates and $\mathbf{J}_2^{-1}$ describes the mapping between the knot space and the integration domain [29].

The *Jacobian* $\mathbf{J}_1$ is given in Equation (3.8a). The domain integration (volumes, surfaces) to obtain the system matrices shown in Equations (2.45) utilizes a *Gauss*ian quadrature scheme in a local coordinate space [125]. The mapping between the knot space and the local integration coordinate space is done using the *Jacobian* $\mathbf{J}_2$ given in Equation (3.8b).

$$\mathbf{J}_1 = \frac{\partial \mathbf{x}}{\partial \boldsymbol{\beta}} = \begin{pmatrix} \frac{\partial x_1}{\partial \beta} & \frac{\partial x_1}{\partial \gamma} & \frac{\partial x_1}{\partial \zeta} \\ \frac{\partial x_2}{\partial \beta} & \frac{\partial x_2}{\partial \gamma} & \frac{\partial x_2}{\partial \zeta} \\ \frac{\partial x_3}{\partial \beta} & \frac{\partial x_3}{\partial \gamma} & \frac{\partial x_3}{\partial \zeta} \end{pmatrix} \tag{3.8a}$$

$$\mathbf{J}_2 = \frac{\partial \boldsymbol{\beta}}{\partial \tilde{\boldsymbol{\beta}}} = \begin{pmatrix} \frac{\partial \beta}{\partial \tilde{\beta}} & 0 & 0 \\ 0 & \frac{\partial \gamma}{\partial \tilde{\gamma}} & 0 \\ 0 & 0 & \frac{\partial \zeta}{\partial \tilde{\zeta}} \end{pmatrix} \tag{3.8b}$$

Using the volume differentials

$$\mathrm{d}V = \mathrm{d}x_1 \, \mathrm{d}x_2 \, \mathrm{d}x_3 = \det \mathbf{J}_1 \, \mathrm{d}\beta \, \mathrm{d}\zeta \, \mathrm{d}\gamma = \det \mathbf{J}_1 \det \mathbf{J}_2 \, \mathrm{d}\tilde{\beta} \, \mathrm{d}\tilde{\gamma} \, \mathrm{d}\tilde{\zeta} \tag{3.9}$$

the matrices given in Equations (2.45) can be expressed as

$$\tilde{\mathbf{A}} = \int\limits_{-1}^{1} \int\limits_{-1}^{1} \int\limits_{-1}^{1} \tilde{\mathbf{Q}}_1^T \tilde{\mathbf{T}} \tilde{\mathbf{Q}}_2 \det(\mathbf{J}_1) \det(\mathbf{J}_2) \mathrm{d}\tilde{\beta} \, \mathrm{d}\tilde{\gamma} \, \mathrm{d}\tilde{\zeta} \,. \tag{3.10}$$

Here $\tilde{\mathbf{A}}$ is replaceable by the element matrices $\mathbf{K}_{uu}$, $\mathbf{K}_{u\phi}$, $\mathbf{K}_{\phi u}$, $\mathbf{K}_{\phi\phi}$ or $\mathbf{M}_{uu}$. The matrices $\tilde{\mathbf{Q}}_1$ and $\tilde{\mathbf{Q}}_2$ denote $\mathbf{H}_u$, $\mathbf{H}_\phi$, $\mathbf{B}_u$ or $\mathbf{B}_\phi$. The matrix $\tilde{\mathbf{T}}$ correspond to the required material matrices $\mathbf{C}^E$, $\mathbf{b}$, $\mathbf{b}^T$, $\boldsymbol{\epsilon}^\sigma$ or ρ. Equally the surface or line integrals are to be dealt with. There the *Jacobian*s are reduced to a lower dimension and only a surface or line integral has to be solved.

A single element which approximates a circular disc is illustrated in Figure 3.2. The control points can be connected and describe a control polynomial. The displacements and electric potential of each element are calculated at the control points. This points can be outside

the geometry. To obtain the displacements and potentials of the real geometry the solution at the control points has to be inserted in the following relation

$$\mathbf{x}_{new} = \sum_{i=1}^{n_{cont}} \sum_{j=1}^{m_{cont}} \sum_{k=1}^{o_{cont}} R_{i,j,k}^{p,q,r}(\beta,\,\gamma,\,\zeta)(\mathbf{x}_{i,j,k} + \mathbf{U}_{i,j,k})\,. \tag{3.11}$$

Typically the inter-element-continuity and the continuity within an isogeometric finite element is C^{p-1}. Therefore, neighbor elements influence each other. A multi-layer material has no clear boundary and also perpendicular corners could not be described. To solve this problems so called "patches" are used [66]. Patches have only C^0-continuity at the boundaries and could be understand as p-element which is defined by piecewise NURBS polynomial. They are helpful to describe the geometry and can be used to model clear material boundaries, e.g. the layers in a composite plate.
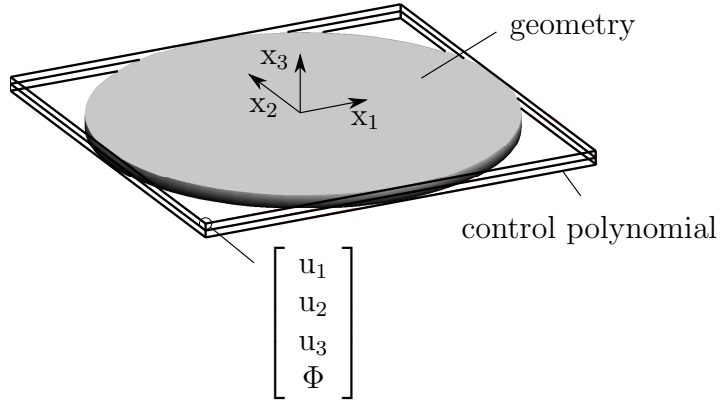

Figure 3.2: Piezoelectric finite element using NURBS shape functions.

3.3 Patch test

In this section the so called patch test is utilized [176]. From a mathematical point of view this test is not a compelling proof of convergence, but it is still advisable to execute this test. An arbitrary mesh of distorted finite elements is established. An external load is applied to the model, e.g. to create a constant strain state, which has to be reproduced exactly. If the specified strain states are calculated exactly, then the convergence of the element is assured [65]. Figure 3.3 illustrates a two-dimensional example. All three possible uniform stress states are plotted. For a three-dimensional piezoelectric finite element three additional stress states as well as two uniform electrical field states have to be applied.
A cube with edge length ($l = 1$ mm) with a randomly distorted mesh is used to calculate uniform stress states. To add the uniform strain states the displacements u are prescribed at the surfaces of the cube.
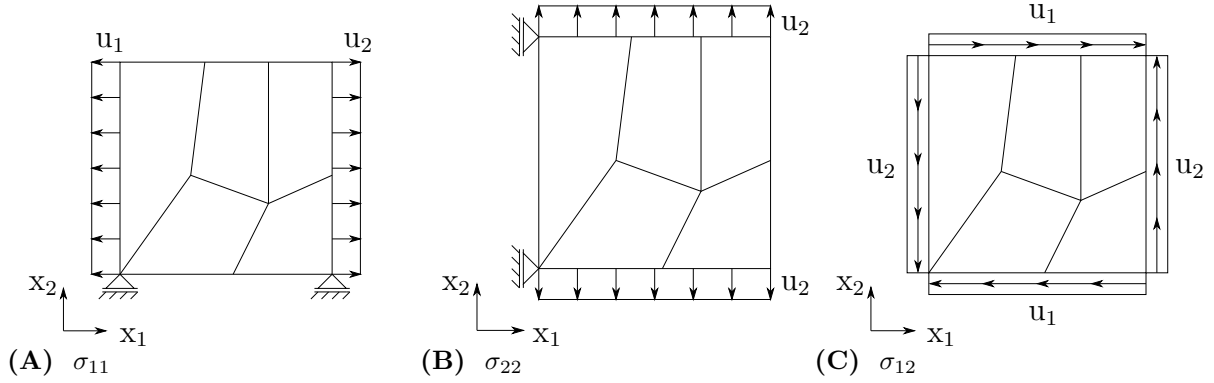
Figure 3.3: Two-dimensional patch test.

Table 3.1. shows the applied displacements for the six different stress states. The *Young*s modulus and the *Poisson*s ratio are chosen as $Y = 10\,\text{N/mm}^2$ and $\nu = 0.3$. The element polynomial order in all directions is $p_{x_i} = 2$ and 16 elements are applied to mesh the cuboid.

Table 3.1: Boundary conditions and prescribed displacements u_i [mm] at the surfaces of the cuboid for the different patch tests.

Test	$x_1 = 0$	$x_1 = 1\,\text{mm}$	$x_2 = 0$	$x_2 = 1\,\text{mm}$	$x_3 = 0$	$x_3 = 1\,\text{mm}$
1	$u_1 = -0.05$	$u_1 = 0.05$	$u_2 = 0$	free	$u_3 = 0$	free
2	$u_1 = 0$	free	$u_2 = -0.05$	$u_2 = 0.05$	$u_3 = 0$	free
3	$u_1 = 0$	free	$u_2 = 0$	free	$u_3 = -0.05$	$u_3 = 0.05$
4	$u_2 = -0.025$	$u_2 = 0.025$	$u_1 = -0.025$	$u_1 = 0.025$	$u_3 = 0$	free
5	$u_3 = -0.025$	$u_3 = 0.025$	$u_2 = 0$	free	$u_1 = -0.025$	$u_1 = 0.025$
6	$u_1 = 0$	free	$u_3 = -0.025$	$u_3 = 0.025$	$u_2 = -0.025$	$u_2 = 0.025$

The tests 1-3 in Table 3.1 cause a one-dimensional strain state and 4-6 represent uniform shear states. Figure 3.4 plots two examples of an uniform stress state.
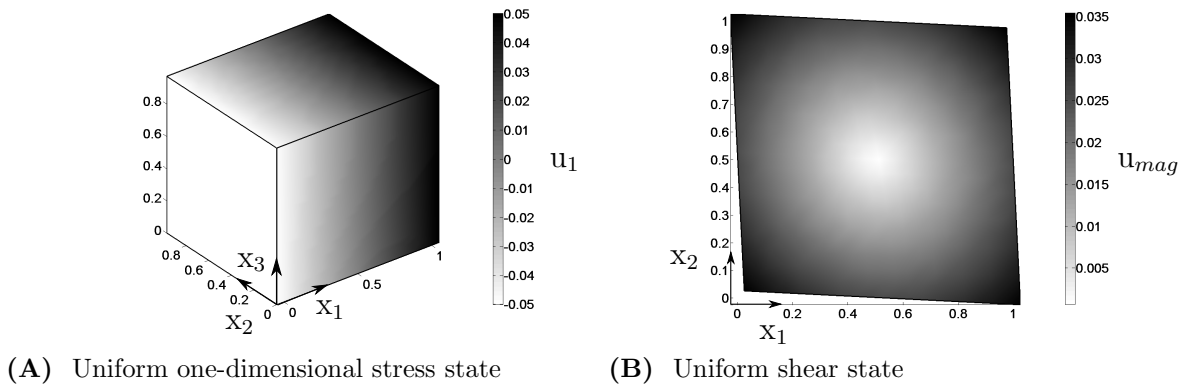

(A)   Uniform one-dimensional stress state   **(B)**   Uniform shear state

Figure 3.4: Examples for the patch test models.

In Figure 3.4A the u_1-displacements for test 1 and in Figure 3.4B the magnitude displacement $u_{mag} = \sqrt{u_1^2 + u_2^2 + u_3^2}$ of test 5 are plotted, respectively. The other four patch tests show similar results.

Table 3.2 shows the mechanical stresses $\boldsymbol{\sigma}$ of the cuboid for the different patch tests. The exact solutions for the defined uniform one-dimensional stress states (tests 1-3) are $\sigma_{ii} = 1$ N/mm^2 and for uniform shear stress states (test 4-6) $\sigma_{ij} = 0.38759$ N/mm^2.

All patch test solutions, also with different polynomial orders, show a good agreement with the expected solution, which agrees with the findings from Lipton et al. [92]. The maximal discrepancy between the expected result and the calculated solution of the figured examples is $2.875 \cdot 10^{-14}$. This is in the range of the computer accuracy.

Table 3.2: Maximal absolute values in [N/mm^2] of all stresses ($Y = 10$ N/mm^2, $\nu = 0.3$ and $G = 3.87596$ N/mm^2).

Test	σ_{11}	σ_{22}	σ_{33}	σ_{12}	σ_{13}	σ_{23}
1	1.0000	$3.0 \cdot 10^{-15}$	$5.1 \cdot 10^{-15}$	$11.2 \cdot 10^{-15}$	$5.8 \cdot 10^{-15}$	$9.7 \cdot 10^{-15}$
2	$2.0 \cdot 10^{-15}$	1.0000	$2.3 \cdot 10^{-15}$	$10.3 \cdot 10^{-15}$	$10.1 \cdot 10^{-15}$	$0.1 \cdot 10^{-15}$
3	$4.1 \cdot 10^{-15}$	$3.7 \cdot 10^{-15}$	1.0000	$22.3 \cdot 10^{-15}$	$28.8 \cdot 10^{-15}$	$8.0 \cdot 10^{-15}$
4	$1.0 \cdot 10^{-15}$	$0.8 \cdot 10^{-15}$	$0.1 \cdot 10^{-15}$	0.38759	$0.6 \cdot 10^{-15}$	$0.5 \cdot 10^{-15}$
5	$4.1 \cdot 10^{-15}$	$2.4 \cdot 10^{-15}$	$3.1 \cdot 10^{-15}$	$1.4 \cdot 10^{-15}$	0.38759	$1.1 \cdot 10^{-15}$
6	$1.9 \cdot 10^{-15}$	$2.6 \cdot 10^{-15}$	$5.7 \cdot 10^{-15}$	$0.9 \cdot 10^{-15}$	$0.8 \cdot 10^{-15}$	0.38759

For completeness, Table 3.3 illustrates the boundary condition of the patch test applying a constant electrical field, and Table 3.4 shows the constant dielectric displacement. In agreement with the previous patch test analysis the distorted elements are able to describe a constant electrical field - dielectrical displacement state.

Table 3.3: Boundary conditions and prescribed electrical potential ϕ_i [V] at the surfaces of the cuboid for the different patch tests.

Test	$x_1 = 0$	$x_1 = 1$ mm	$x_2 = 0$	$x_2 = 1$ mm	$x_3 = 0$	$x_3 = 1$ mm
1	$\phi_1 = 1$	$\phi_1 = 0$	free	free	free	free
2	free	free	$\phi_2 = 1$	$\phi_2 = 0$	free	free
3	free	free	free	free	$\phi_3 = 1$	$\phi_3 = 0$

Table 3.4: Maximal absolute values in [As/m^2] of all stresses ($\epsilon = 1$ F/m).

Test	D_1	D_2	D_3
1	1	0	0
2	0	1	0
3	0	0	1

3.4 Influence of the geometrical mapping

The representation of the geometry of a structure is an important quantity that has to be considered when thinking about finite element models. Although standard isogeometric finite elements based on quadratic *Lagrange* polynomials are in theory able to exactly describe boundaries with an quadratic variation other issues may arise. These elements are for example not capable to resolve a quadratic displacement field accurately if the geometry is varying quadratically as well. In this section the behaviour of NURBS elements is studied with respect to the mentioned phenomenon. Figure 3.5 illustrates the numerical model setup ($l/h = 1/10$). A two-dimensional plain-strain model is deployed and discretized using two finite elements. Only the interior boundary is described by a quadratic function. As *Dirichlet* boundary condition a linear displacement field is prescribed at the end of the beam. These displacements results in a quadratic u_2-displacement function with respect to x_1.
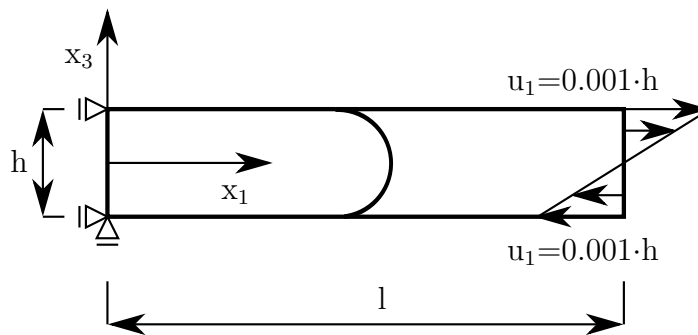

Figure 3.5: Geometrical mapping test with two two-dimensional NURBS elements with a quadratic element boundary with $l/h = 10$.

Generally speaking, every quadratic polynomial can be exactly determined using three arbitrary points on this curve. Hence, a linear system of equations has to be solved in order to compute the unknowns of the polynomial. In this respect the polynomial type does not have an influence to evaluate this function. The graphs of every representation may be different in terms of their representation but nonetheless both functions must coincide.
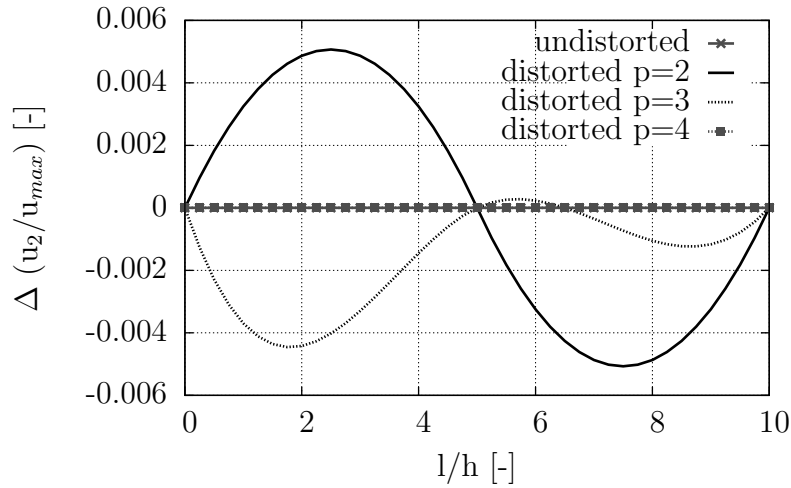Figure 3.6A shows the results of the undistorted case, where both isogeometric elements are of rectangular shape. For this example, the curves of the isogeometric and the quadratic polynomial curve of the normalized u_3-displacement coincide. In contrast to the aforementioned behaviour, Figure 3.6B shows that the displacements calculated by the isogeometric finite elements do not coincide with the quadratic function. For the sake of visualization, Figure 3.6C shows the difference between both results in a detailed view.
From the results given, it can be concluded that the geometrically undistorted elements are able to capture the displacement field accurately, whereas the distorted elements, with the interior boundary described by a quadratic function are not able to exactly compute the displacements. If the polynomial degree is increased the displacement field is still incorrect if $p = 3$ is used. Only if $p = 4$ both the quadratic geometry and the quadratic displacement field are exactly captured.
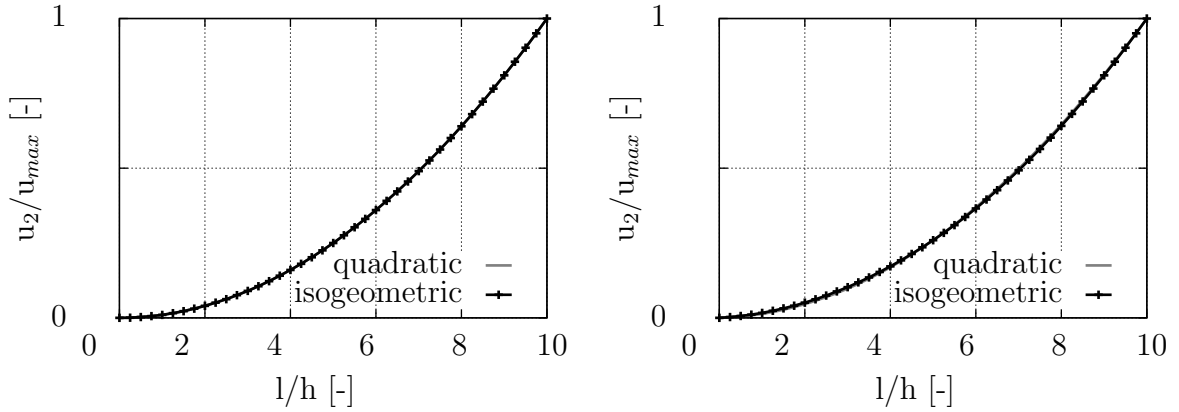
(A) Normalized displacement u_3 at $x_3 = -h/2$ of the undistorted elements

(B) Normalized displacement u_3 at $x_3 = -h/2$ distorted elements

(C) Difference of the undistorted and distorted normalized displacement in x_3-direction

Figure 3.6: Results of the geometrical mapping test with two two-dimensional elements with a quadratic element boundary.

This conclusion agrees with the mathematical description. A general two-dimensional quadratic displacement function

$$u = \delta_1 + \delta_2 x_1 + \delta_3 x_3 + \delta_4 x_1 x_3 + \delta_5 x_1^2 + \delta_6 x_3^2 \tag{3.12}$$

is assumed. To approximate the geometry Equation (3.1) given here in matrix form

$$x_1 = \mathbf{H}_1(\beta, \gamma) x_{1P} \qquad \text{and} \qquad x_2 = \mathbf{H}_1(\beta, \gamma) x_{3P} \tag{3.13}$$

is used. Substituting Equation (3.13) into Equation (3.12) results in

$$u = \delta_1 + \delta_2 \mathbf{H}_1(\beta, \gamma) x_{1P} + \delta_3 \mathbf{H}_1(\beta, \gamma) x_{3P} + \mathbf{H}_1^2(\beta, \gamma)(\delta_4 x_{1P} x_{3P} + \delta_5 x_{1P}^2 + \delta_6 x_{3P}^2). \tag{3.14}$$

If a quadratic geometry approximation is assumed $\mathbf{H}_1(\beta, \gamma)$ includes shape functions up to order $p = 2$. The highest polynomial order in Equation (3.14) is four. The displacement interpolation of the finite element can be written as

$$u = \mathbf{H}_2(\beta, \gamma) u_P. \tag{3.15}$$

It can be clearly seen that the highest polynomial order is quadratic if $\mathbf{H}_2(\beta, \gamma)$ is chosen as quadratic NURBS function. The necessary higher order terms to describe the general displacement function in Equation (3.14) do not exist. Therefore, the elements are not able to describe the displacement function accurate in all cases. For the undistorted or linear distorted elements only the constant or linear terms of $\mathbf{H}_1(\beta, \gamma)$ have to be used to describe the geometry correctly. In that case the quadratic NURBS elements are able to describe a displacement function exactly, because the highest polynomial order in Equation (3.14) is equal to the one in $\mathbf{H}_2(\beta, \gamma)$. If the order of the NURBS elements is increased to $p = 4$ both the quadratic geometry approximation and the quadratic displacement field can be described, because the highest polynomial order terms in Equation (3.14) and $\mathbf{H}_2(\beta, \gamma)$ are equal.

It can be seen that quadratic isogeometric finite elements are able to describe a quadratic geometry exact, but this results in an inability to resolve a quadratic displacement field. This agrees with standard *Lagrange* finite elements as shown in [176].

3.5 Numerical examples

Several tests are conducted to check the performance of the NURBS element. The tests are divided in two types. First it is started with static calculations, e.g. the piezoelectric bimorph beam. In the next section two different dynamic calculations are performed. The eigenfrequency solution of the NURBS element is compared with different reference solutions. Moreover, a three-dimensional plate with a conical hole is calculated and compared with an ABAQUS reference solution.

3.5.1 Piezoelectric bimorph beam

The first benchmark test is a piezoelectric bimorph beam (see Figure 3.7) described in [48, 95, 146, 165]. One side ($x_1 = 0$) of the beam is clamped. The length, width and height are $l = 100\,\text{mm}$, $b = 5\,\text{mm}$ and $h = 1\,\text{mm}$, respectively. Table A-2 shows the material properties of the homogeneous beam [95].
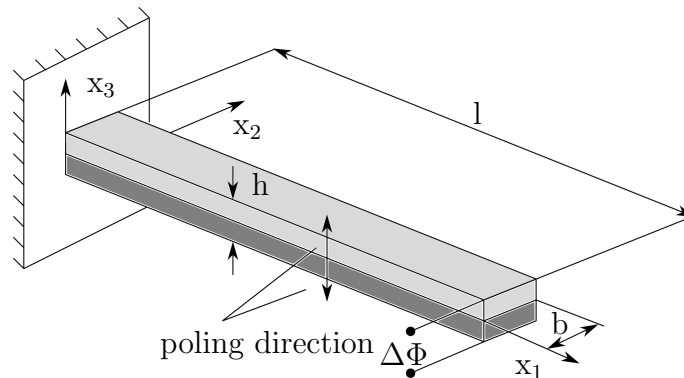

Figure 3.7: Model of a piezoelectric bimorph beam.

The material properties and the thickness of the top (gray) and the bottom (dark gray) layer are equal and both plies are polarized in x_3-direction but with opposite orientation. The beam is modeled with two patches. A patch contains a number of NURBS elements with C^{p-1}-continuity between the element boundaries inside the patch, where $p > 1$. Each patch is defined with a separate knot vector $\mathbf{V}$, and between two patches C^0-continuity exists.

With a constant electrical field in x_3-direction, the upper part of the beam shrinks and the lower part extends. Thus, a constant bending moment is introduced. Using the *Euler-Bernoulli* beam theory, the bending moment can be derived as [95]

$$M = \frac{bh^2}{4} b_{31} Y \,, \tag{3.16}$$

and the displacements are

$$u_3(x_1) = \frac{3}{2} \frac{b_{31} \Delta \Phi}{Y h^2} x_1^2 \,. \tag{3.17}$$

Figure 3.8 shows the displacements in u_3-direction for three simulations with different isogeometric NURBS elements in comparison to the analytical solution calculated by Equation (3.17). The description ($p = 2, 2, 2$) denotes the polynomial degree in x_1-, x_2-, x_3-directions and "dof" is the number of degrees-of-freedom.
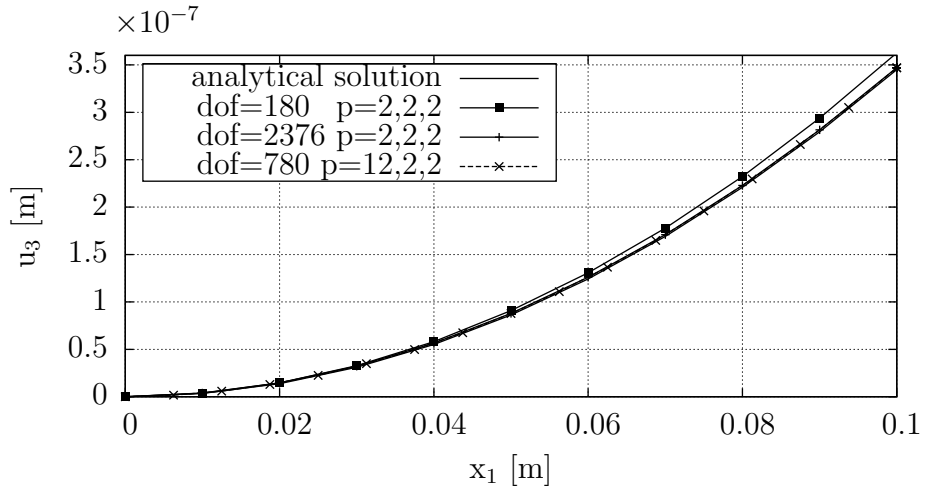

Figure 3.8: Calculated displacement u_3 at $(x_1, x_2 = b/2, x_3 = h/2)$ under constant external electrical field for $\Delta \Phi = 1\,\text{V}$.

Table 3.5 illustrates the relative displacement error of the FEM solution with respect to the analytical solution of the deflection at the free end of the beam. Each finite element patch is discretized with one element over the thickness. Three refinement methods (p-refinement, h-refinement and k-refinement) can be applied to increase the quality of the solution. Only the h-refinement and the k-refinement are presented here. A k-refinement involves much fewer degrees-of-freedom than a p-refinement, which increases the polynomial order inside an element only without influencing the continuity between the elements [30]. Therefore, the p-refinement is not considered.

It must be noted that the p-refinement and the k-refinement schemes are equal if only a single element is used. As starting point a model with 180 degrees of freedom and an

Table 3.5: Relative error of the displacement at $x_1 = 0.1\,\mathrm{m}$.

Model	$dof = 180$	$dof = 780$	$dof = 2376$
rel. Error	5.1%	0.582%	0.547%

uniform polynomial order of $p_{x_{1,2,3}} = 2$ is chosen. The relative error of this solution is around 5.1%. Increasing the polynomial order to 12 (using a k-refinement scheme [66]) the error is reduced to 0.582%. The number of degrees-of-freedom is 780. The polynomial order elevation is done only in x_1-direction. Using different polynomial orders in different directions allows a reduction of the degrees-of-freedom without loosing accuracy.

For the h-refinement the elements are divided into smaller ones. The number of degrees-of-freedom increases, but the polynomial order $p_{x_{1,2,3}} = 2$ is not changed. A higher number of degrees-of-freedoms (dof=2376) has to be used to reach the same accuracy in the solution which has been obtained with the k-refinement. It must be remarked that the effort to solve the system of equations is less using higher polynomial degrees, but the assembling of the system matrices requires more effort in relation to the total computational time. The effort can be reduced by applying efficient quadrature rules ("half-point rule"), which make higher order NURBS elements more attractive [67]. However, an efficient integration schema is not in the focus of this thesis and therefore not studied. Different polynomial degrees for different directions can be used to increase the quality considerably with less required assembling time, e.q. a mixed polynomial ansatz ($p_{x_1} = 8, p_{x_2} = 2, p_{x_3} = 2$) with 540 dof results in almost the same accuracy as an equal polynomial ansatz in all directions ($p_{x_1} = 8, p_{x_2} = 8, p_{x_3} = 8$) with 5508 dof. The relative error for the mixed polynomial ansatz is 0.93% and for the equal polynomial ansatz 0.94%, respectively. In simple structures, this mixed polynomial formulation is easy to implement. It should be guaranteed that at the coupling surfaces between different parts of a structure equal polynomial degrees are used.

It can be seen that the solution improves when increasing the polynomial order and also with an increasing number of degrees-of-freedom. It is obvious that the numerical solution never reaches the analytical solution, because the 3D solution does not fulfill the assumptions introduced in the *Euler-Bernoulli* beam theory exactly.

In Table 3.6 the accuracy of the solution is compared with other methods. Five elements are used to calculate the solution proposed by Marinković et al. [95]. The Abaqus solution is calculated with fully integrated, quadratic, piezoelectrical elements (C3D20E). To obtain comparable results the polynomial degree of the NURBS elements are chosen uniform as $p = 2$. Table 3.6 conveys that NURBS elements are more accurate for the chosen example than the Abaqus solution. Abaqus needs 432 degrees-of-freedoms and with isogeometric elements only 360 degrees-of-freedoms are required to receive the same accuracy. In the solution given by Gabbert et al. [48] the calculated displacements are smaller, than in the analytical solution. The accuracy of both elements, Gabbert and isogeometric, is similar.

Table 3.6: Static deflection in 10^{-7} m of the piezoelectric bimorph beam.

Distance [m]	0.02	0.04	0.06	0.08	0.1
Analytical	0.138	0.522	1.242	2.208	3.450
Sze [146]	0.138	0.522	1.242	2.208	3.450
Gabbert [48]	0.136	0.545	1.229	2.189	3.424
ABAQUS	0.150	0.586	1.294	2.277	3.534
Present	0.142	0.560	1.257	2.23	3.479

Sze et al. [146] have used solid-shell elements, which are based on the assumptions of the *Kirchhoff* plate theory. The solution of the beam deflection given by Gabbert et al., ABAQUS and the presented isogeometric element does not reach the analytical as well as the solid-shell solution given by Sze. The reason is, that the three-dimensional volume elements do not fulfill the *Kirchhoff* hypothesis used for the calculation of the analytical solution. This results in a small discrepancy between the three solutions and the analytical solution. The solid-shell element proposed by Sze fulfills the *Kirchhoff* hypothesis. Therefore, the solution obtained with these elements reproduces the analytical solution exactly. Nevertheless, the tests have shown that the NURBS elements give equal or better results than conventional volume elements without the need to introduce special assumptions.

3.5.2 Shape control of an active plate

The second benchmark problem deals with an active composite plate. It illustrates the combination of an active and a passive structure. An active piezoelectric patch applied to a structure can be used to reduce the deflection of the plate caused by an external load.
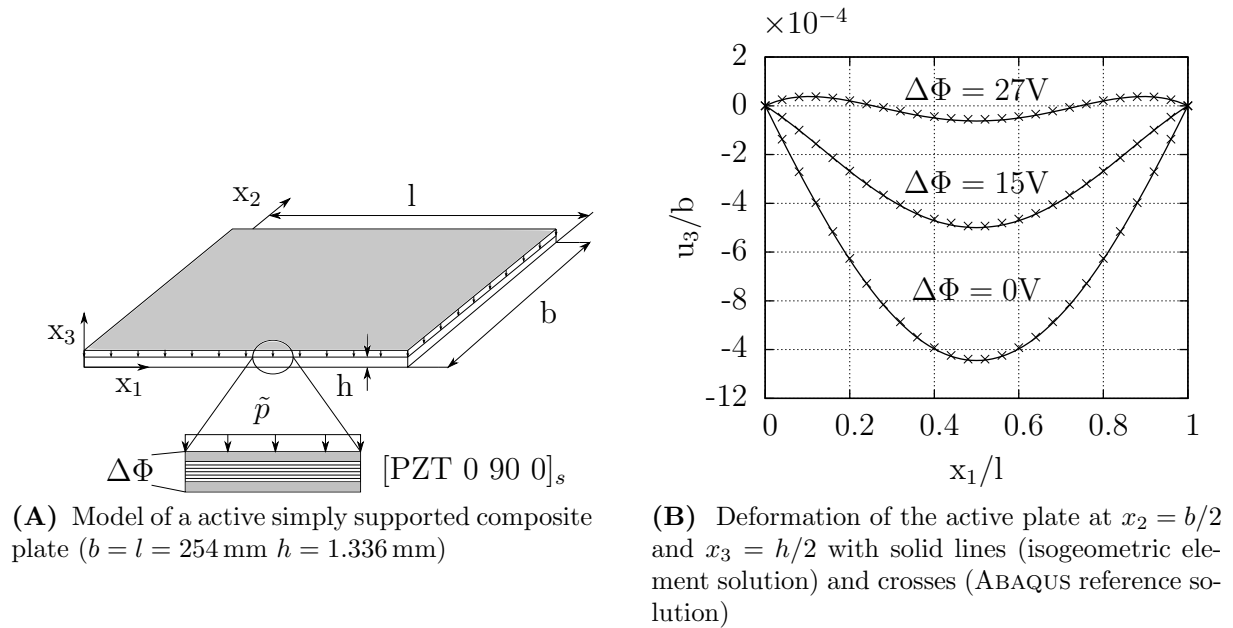

(A) Model of a active simply supported composite plate ($b = l = 254$ mm $h = 1.336$ mm)

(B) Deformation of the active plate at $x_2 = b/2$ and $x_3 = h/2$ with solid lines (isogeometric element solution) and crosses (ABAQUS reference solution)

Figure 3.9: Active multi-layer plate.

The plate model is shown in Figure 3.9A. The top and the bottom layer of the plate consist the piezoceramic material PZT G1195. The material parameters are taken from Kioua and Mirza [74]. The layers in between the top and the bottom layers are made of T300/976. They are stacked together as a symmetric cross ply laminate $[0\,,90\,,0]_S$. The properties of both materials are given in Table A-3.

The plate is simply supported at the edges of the central plane of the plate and a constant pressure of $\tilde{p} = 200\,\text{N/mm}^2$ is applied at the top surface. Each lamina layer is modeled with three-dimensional finite elements. Each layer is approximated in thickness direction (x_3-direction) with linear shape functions to minimize the numerical effort. Tests have shown that significant locking phenomena do not occur and a higher polynomial degree in x_3-direction does not improve the solution significantly. In x_1- and x_2-directions higher order polynomials are used. For the calculation, the in-plane polynomial degrees are chosen as $p_{x_1} = 4$ and $p_{x_2} = 4$. Each layer is discretized equally. When applying different electrical boundary conditions ($\Delta\Phi = 0\,\text{V}$, $\Delta\Phi = 15\,\text{V}$, $\Delta\Phi = 27\,\text{V}$) which are proposed by Kioua and Mirza [74], the deformation of the plate is reduced.

The normalized displacement u_3/b is shown in Figure 3.9B. The results are compared with an ABAQUS reference solution, where fully integrated elements with quadratic shape functions are used to simulate a quarter of the plate (C3D20, C3D20E, dof=191823). The solid lines denote the isogeometric finite element solution and the crosses describe the results obtained using ABAQUS. Both solutions coincide with solutions given by Marinkovìc et al. [96].

Figures 3.10A and 3.10B show the deformed shape of the plate for $\Delta\Phi = 0\,\text{V}$ and $\Delta\Phi = 27\,\text{V}$. Both deformed shapes coincide with the solutions obtained by ABAQUS as well as by Marinkovìc [96].
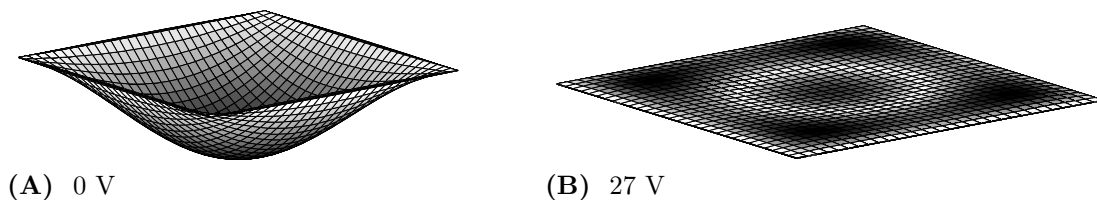

(A) 0 V   **(B)** 27 V

Figure 3.10: Deformed shape $(u_3(x_1/l, x_2/b)/b)$ of a composite plate under a constant surface load $(\tilde{p} = 200\,\text{N/mm}^2)$.

3.5.3 Bimorph ring actuator

The third example is a clamped bimorph ring actuator consisting of two piezoelectric layers. This type of actuator is used, e.g. to build piezoelectric linear motors [69]. The material of both layers is PIC-151. The properties are given in Table A-5 and Figure 3.11 shows the setup.

The height of each layer is $h/2 = 0.254\,\text{mm}$. Both layers are poled in opposite directions and an electrical potential difference of $\Delta\Phi = 200\,\text{V}$ between the top and the bottom surface is applied. The opposite polarization introduces a bending moment in the same manner as the bimorph beam presented in section 3.5.1. Due to the symmetry of the

problem only a quarter of the ring is modelled with NURBS elements as well as with standard finite elements (C3D20E).
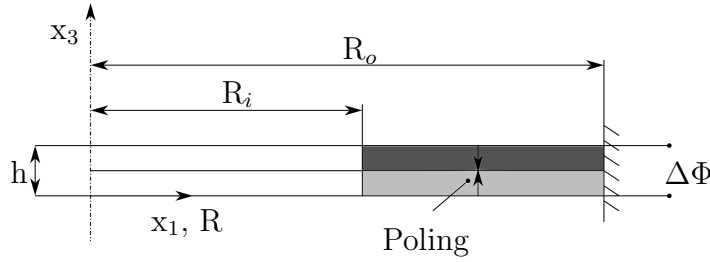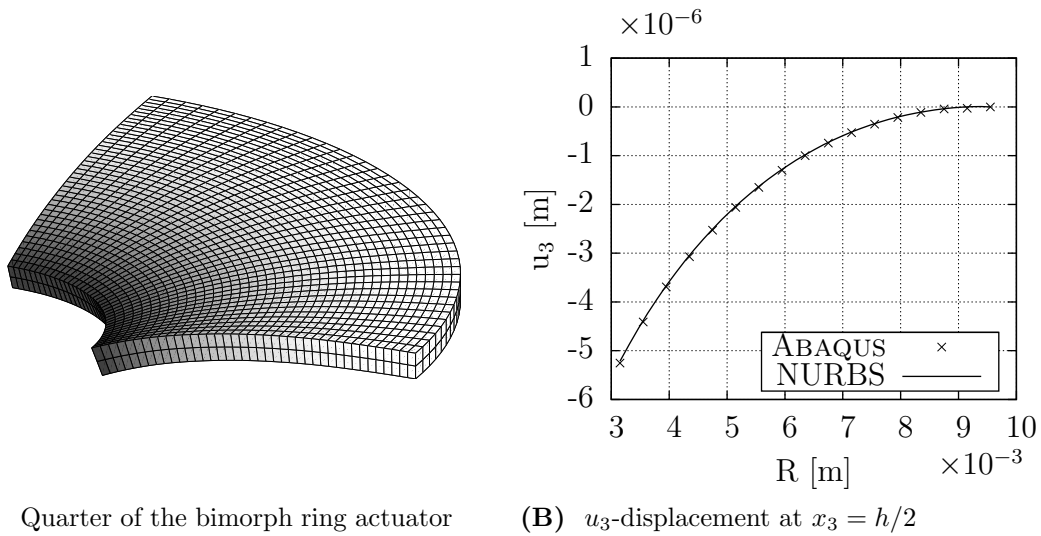

Figure 3.11: Cross section of the clamped piezoelectric ring-type bending actuator with clamped outer edge ($R_i = 3.1\,\text{mm}$, $R_o = 9.555\,\text{mm}$).

This simplifies the application of the boundary conditions in comparison to any smaller segment, which could also be used. Results calculated with ABAQUS by applying a very fine mesh (C3D20E, dof=676404) are taken as reference values.

(A) Quarter of the bimorph ring actuator

(B) u_3-displacement at $x_3 = h/2$

Figure 3.12: Bimorph ring actuator $\Delta\Phi = 200\,\text{V}$

The deformation of a calculated quarter of the bimorph ring is illustrated in Figure 3.12A. Figure 3.12B shows the u_3-displacements of the ring at the position (x_1, $x_2 = 0$, $x_3 = h/2$). The ABAQUS reference solution (crosses) as well as the converged solution calculated with the new isogeometric NURBS element (solid line) are plotted in Figure 3.12B. Both results are in a good agreement.

In Figure 3.13 the evolution of the relative error of the maximum u_3-displacement with respect to the degrees-of-freedom is illustrated. The simulations utilizing the isogeometric piezoelectrical element concept are performed with three different polynomial degree templates. The polynomial degree is changed only in x_1- and x_2-direction ($p_{x_1} = p_{x_2} = p$). In x_3-direction for all isogeometric NURBS elements a quadratic polynomial ($p_{x_3} = 2$) has been prescribed.
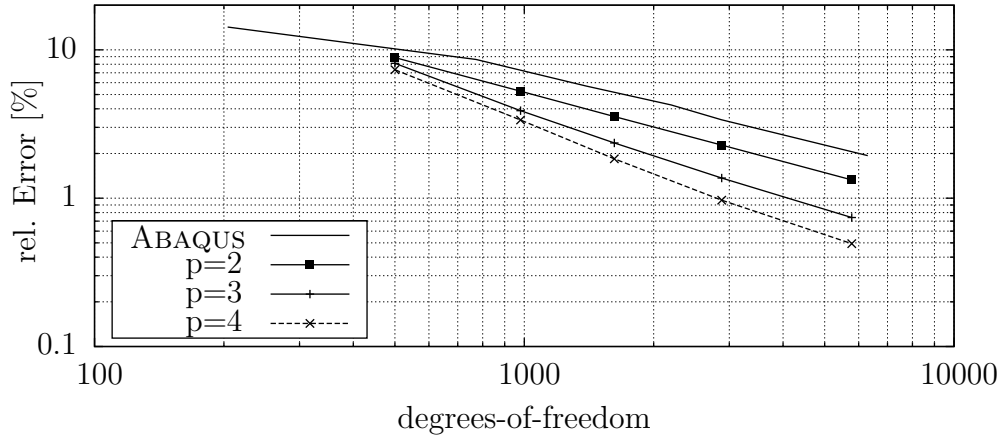
Figure 3.13: Convergence of one ABAQUS and three NURBS ($p_{x_1} = p_{x_2} = p$, $p_{x_3} = 2$) solutions compared to an ABAQUS reference solution.

Increasing the number of degrees-of-freedom results in a decreasing error for both numerical models. As expected, the accuracy increases using higher polynomial degrees. The convergence rate of the quadratic ABAQUS elements and the quadratic NURBS elements are identical, because an equal polynomial order of the shape functions is used. The convergence rate only depends on the polynomial degree and not on the polynomial type [13]. However, NURBS elements reach a better accuracy of the solution due to the exact approximation of the geometry [73]. This can also be seen in Figure 3.13, where the NURBS curve ($p_{x_{1,2,3}} = 2$) and the ABAQUS solution have the same convergence rate, but the NURBS solution is more accurate due to the exact description of the geometry. The solution calculated with isogeometric NURBS elements needs only 50% of the degrees-of-freedom to obtain the same accuracy as the ABAQUS solution.

3.5.4 Piezoelectric circular plate

After verifying the NURBS element in several static tests an eigenvalue problem is solved, where the eigenfrequencies and the eigenforms of a free-free circular plate are computed (see Figure 3.14). The plate consists of the piezoceramic material PIC-151 and the material properties are specified in Table A-5. The diameter and the height of the plate are $d = 0.03\,\mathrm{m}$ and $h = 0.001\,\mathrm{m}$, respectively.
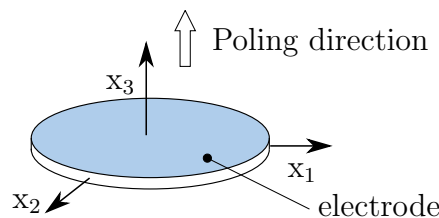

Figure 3.14: Coordinate system of a free-free circular piezoelectric plate. The electrical potential at the bottom electrode is set to zero.

The circular plate is metalized on top and bottom and it is modeled with two different electrical potential boundary conditions. The first calculation assumes that the electrical

potential of the whole structure is set to zero (ideal short circuit). In this case no piezoelectric coupling exists and the plate behaves like an elastic plate. With this assumption the analytical solution of a free-free circular plate, e.g. given by Giurgiutiu [49], can be used to verify the solution. In the second calculation there is no electrical connection between the top and the bottom surface. In this case a charge separation takes place which results in a difference of the electrical potential between the top and the bottom surface. To calculate the eigenfrequencies of the system a separation ansatz of the form

$$
\begin{bmatrix} \mathbf{U}_{\text{cont}} \\ \boldsymbol{\Phi}_{\text{cont}} \end{bmatrix} = e^{i\omega_0 t} \begin{bmatrix} \hat{\mathbf{U}} \\ \hat{\boldsymbol{\phi}} \end{bmatrix}
\tag{3.18}
$$

is used and inserted in Equation (2.44a) and (2.44b), which results in

$$
\left(-\omega_0^2 \begin{bmatrix} \mathbf{M}_{uu} & 0 \\ 0 & 0 \end{bmatrix} + \begin{bmatrix} \mathbf{K}_{uu} & \mathbf{K}_{u\phi} \\ \mathbf{K}_{\phi u} & -\mathbf{K}_{\phi\phi} \end{bmatrix} \right) \begin{bmatrix} \hat{\mathbf{U}} \\ \hat{\boldsymbol{\phi}} \end{bmatrix} = \begin{bmatrix} 0 \\ 0 \end{bmatrix} .
\tag{3.19}
$$

From the second equation one receives

$$
\hat{\boldsymbol{\phi}} = \mathbf{K}_{\phi\phi}^{-1} \mathbf{K}_{\phi u} \hat{\mathbf{U}} .
\tag{3.20}
$$

Substituting Equation (3.20) in the first equation of Equation (3.19) the eigenvalue problem is derived as

$$
(\mathbf{K}_{uu} + \mathbf{K}_{u\phi} \mathbf{K}_{\phi\phi}^{-1} \mathbf{K}_{\phi u} - \omega_0^2 \mathbf{M}_{uu}) \hat{\mathbf{U}} = 0 .
\tag{3.21}
$$

In the short circuit case the electric potential $\hat{\boldsymbol{\phi}}$ is set to zero, which results in

$$
(\mathbf{K}_{uu} - \omega_0^2 \mathbf{M}_{uu}) \hat{\mathbf{U}} = 0 .
\tag{3.22}
$$

In Table 3.7 the solutions are illustrated. The short circuit case is presented in columns (1) to (3) and the open circuit case in columns (4) and (5). Results of the short circuit model are calculated with three different approaches, the analytical solution (1), the ABAQUS finite element solution (2) and the proposed new isogeometric finite element solution (3). The open circuit results are calculated with ABAQUS finite elements (4) and again with the new isogeometric finite elements (5). The ABAQUS reference solution uses fully integrated, quadratic elements (C3D20, C3D20E). The NURBS element solution is calculated with the polynomial order $p_{x_1} = p_{x_2} = 5$ in x_1- and x_2-direction and with $p_{x_3} = 2$ in x_3-direction (see Figure 3.14).

The solutions (1)-(3) of Table 3.7 show a good agreement between the analytical solution (1) and both numerical solutions (2) and (3). The small discrepancy with the analytical solution results from the assumption of material isotropy, because only in-plane material properties can be used in this case. Therefore, the transversal isotropic behavior of the plate is not represented correctly in the analytical solution. Both, the ABAQUS and the isogeometric solution are in a good agreement.

The results (4)-(5) of the first eight eigenfrequencies of the ABAQUS (4) and the isogeometric (5) solution also coincide very well. It should be noted that not all eigenfrequencies are equally influenced by the piezoelectric coupling. Mainly the second and the eighth eigenmode show a strong influence. The ABAQUS as well as the isogeometric solutions predict the same behavior. Due to the stiffening effect caused by the electromechanical coupling, the eigenfrequencies of the open circuit case are generally higher compared to the short circuit case.

Table 3.7: First eight non zero transversal eigenfrequencies in kHz and mode shapes of a circular plate (1 - analytical solution, 2 - Abaqus elastic, 3 - NURBS elastic, 4 - Abaqus piezoelectric, 5 - NURBS piezoelectric).

Number	Modeshape	different models				
		1	2	3	4	5
1		3.13	3.11	3.1	3.17	3.17
2		5.4	5.41	5.41	6.25	6.26
3		7.3	7.2	7.21	7.37	7.34
4		12.23	12.08	12.1	12.91	12.93
5		12.84	12.53	12.56	13.64	13.65
6		19.7	19.04	19.11	19.69	19.74
7		21.02	20.45	20.51	22.79	22.86
8		22.97	22.38	22.44	25.14	25.22

3.6 Influence of locking

In this section the influence of the so called locking effect to the accuracy of the numerical solution computed with isogeometric finite elements is studied. The focus is on the shear locking effect. However, material induced locking is not in the scope of the current work. Geometrical locking is caused if the shape functions are not able to describe the solution of the model problem adequately. This effect worsens if the elements are distorted. If the influence of the adhesive layer between actuator and host structure is to be studied, highly distorted finite elements are useful. Otherwise the required fine discretization ($d_{actuator} \geq 5$ mm and $h_{adhesive} \leq 100$ μm) would result in numerical costs which are disproportionate for the considered task.
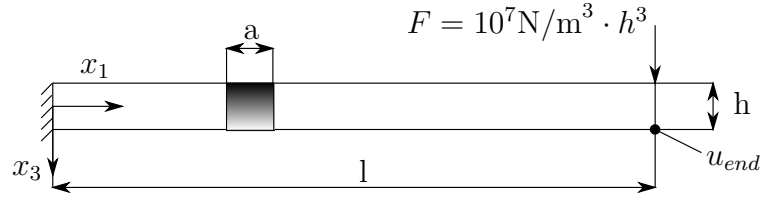
Figure 3.15: Two-dimensional aluminum beam model to study the geometrical locking effect of isogeometric elements ($l = 20$ mm, $a = 2$ mm, $b = 1$ mm).

Higher order finite elements have a better ability to approximate complex displacement fields. Therefore, the locking effect plays a minor role [14]. Figure 3.15 shows the consulted problem. A two-dimensional cantilever beam with a point force at the free end is modeled with isogeometric finite elements of different polynomial order.

The beam length, beam width and the element length are chosen as $l = 20$ mm, b=$1mm$ and $a = 2$ mm. The element and the beam thickness are equal and arbitrary. The displacement u_{end} is calculated for different aspect ratios a/h, while the element length a remains constant whereas the thickness h is successively decreased. If the shape functions can not describe the displacement field exactly higher values of a/h result in an artificial stiffening effect.

Using the *Euler-Bernoulli* beam theory the deflection of the free end is given as

$$u_3(x_1) = \frac{4Fx_1^3}{Ybh^3}, \qquad u_{end}(x_1 = l) = \frac{4Fl^3}{Ybh^3}. \tag{3.23}$$

If the magnitude of the force is $F = \hat{F} \cdot h^3 = 10^7 \text{N/m}^3 h^3$ is chosen

$$u_3(x_1) = \frac{4\hat{F}x_1^3}{Yb}, \tag{3.24}$$

the displacement field is independent from the change of the thickness of the beam. All changes in the calculated displacement field can then be attributed to the geometrical locking effect. Doing so, the beam deflection at the free end of the aluminum beam (see Table A-1) is given as $u_3(l) = 4.57142 \cdot 10^{-6}$ m.

Figure 3.16A illustrates the first result for $p_{x_1} = 2$ in x_1-direction and a variable polynomial degree in x_3-direction $p_{x_3} = 1 \ldots 5$. As illustrated in Equation 3.23 the displacement field of the problem is of order three in x_1-direction. Therefore, the solution gained using the polynomial degree $p_{x_1} = 2$ tends to be corrupted by geometrical locking for higher aspect ratios a/h. Higher polynomial degrees in x_3-direction lead to a reduction of this effect.
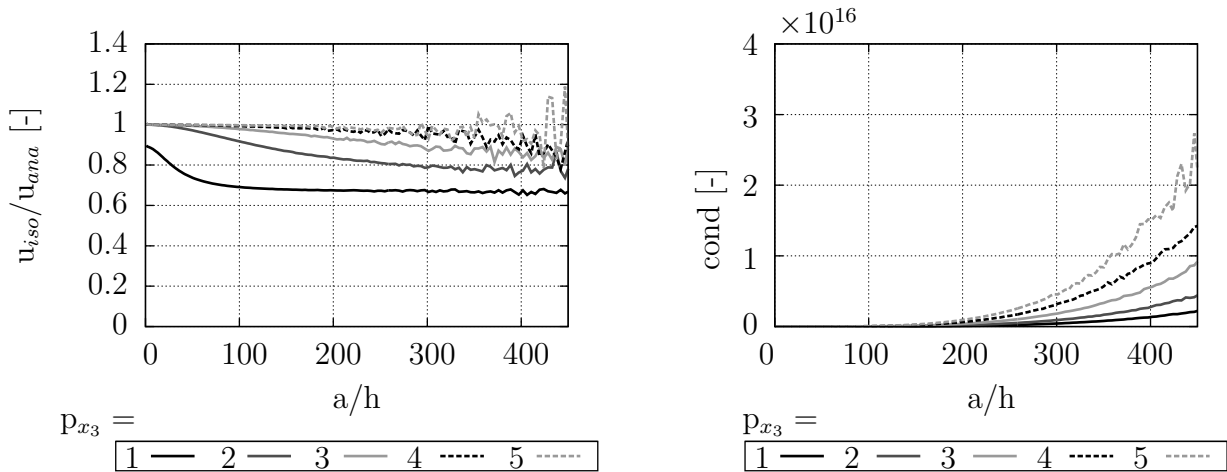
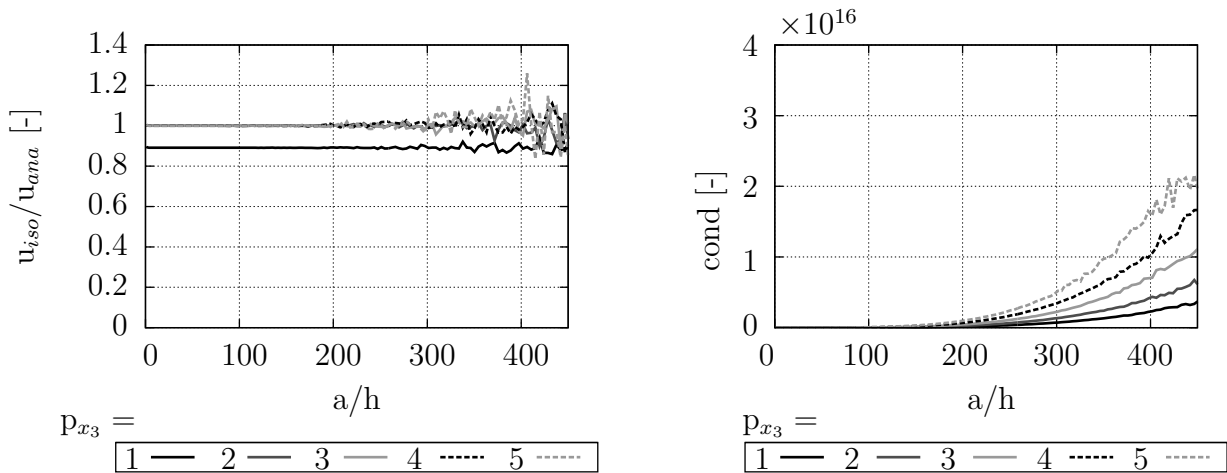**(A)** Normalized beam deflection of the free end (u_{iso} - isogeometric finite element; u_{ana} - analytical solution)

(B) Condition number of the stiffness matrix

Figure 3.16: $p_{x_1} = 2$, $p_{x_3} = 1 \ldots 5$.

For aspect ratios of $a/h > 180$ the solution starts to oscillate. The effect is caused by the drastic increase of the condition number (see Figure 3.16B). The absolute accuracy of the Matlab is $eps = 1.110223024625157e^{-016}$. A condition number higher than 10^{16} means

(A) Normalized beam deflection of the free end (u_{iso} - isogeometric finite element; u_{ana} - analytical solution)

(B) Condition number of the stiffness matrix

Figure 3.17: $p_{x_1} = 3$, $p_{x_3} = 1 \ldots 5$.

that the problem is badly stated and no numerical solution can be found. However, the bound of the condition number to gain an exact solution is much lower [39].

Element distortions for aspect ratios $a/h > 180$ should be avoided even for higher order approaches to obtain an acceptable quality of the numerical solution. The results of the simulations with a polynomial degree $p_{x_1} = 3$ in x_1-direction are plotted in Figure 3.17A. The polynomial degree in x_1-direction coincides with the order of the displacement field in x_1. Besides the results for polynomial degree $p_{x_3} = 1$ all solutions do not change until the

condition number is too high (around $a/h > 180$ in Figure 3.17B), no locking effect occurs. However, the linear ansatz over the thickness does not fulfill the exact model displacement function in this direction, which is of quadratic order.
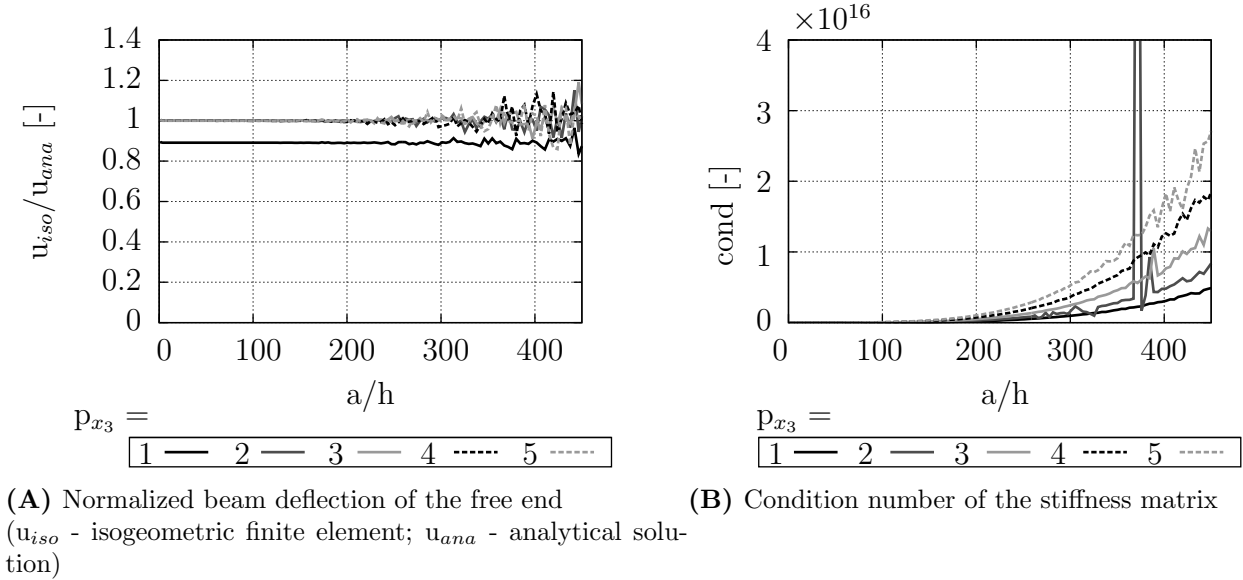

(A) Normalized beam deflection of the free end (u_{iso} - isogeometric finite element; u_{ana} - analytical solution)

(B) Condition number of the stiffness matrix

Figure 3.18: $p_{x_1} = 5$, $p_{x_3} = 1 \ldots 5$.

In Section 4.4 the optimal polynomial degree combination for *Lamb* wave simulation is found to be $p_{x_1} = 5$ and $p_{x_3} = 4$. The numerical investigation of adhesive layer influence is done using this optimal definition of the isogeometric elements. In Figure 3.18A the solution is plotted. As expected no locking phenomenon occurs. Also the condition numbers in Figure 3.18B show a similar change in comparison to $p_{x_1} = 3$. Therefore, an element aspect ratio $a/h < 180$ guarantees a good accuracy of the solution. However, in the further work a time-integration schema has to be applied. If so, a high condition number reduces the overall accuracy of the solution of a dynamic problem. Therefore, an aspect ratio of $a/h < 180$ is recommended. Furthermore distorted elements lead to a reduction of the required explicit time-integration step width which leads to a higher computation time.

3.7 Summary

The developed finite element has been tested by solving several benchmark problems and a good agreement has been shown with analytical and ABAQUS reference solutions. The coupling between piezoelectric structural elements and passive structures can be easily implemented by using equal order polynomials in the bonding area between both parts. The tests have demonstrated that the use of higher order polynomial degrees in isogeometric elements results in a reduction of the required total number of degrees-of-freedom. Furthermore, it is shown that a better geometrical approximation with isogeometric elements, e.g. if circular piezoelectric patches are used, results in more accurate solutions in comparison to standard isoparametric finite elements.

Since real passive and active structures are very complex, e.g. special phased array designs [134], comb-type transducer comprised of multiple piezoelectric elements, which are

piezoelectric fiber composites sandwiched between electrodes [89] or complex electrode configurations [106], the proposed isogeometric finite elements can lead to a significant reduction of the required degrees-of-freedom in order to obtain a sufficiently accurate solution. Moreover, in this chapter the influence of locking has been studied. The results show, that moderately distorted elements $a/h < 180$ do not influence the quality of the solution noticeably. Therefore, these three-dimensional isogeometric finite elements are appropriate to analyse thin structures as well as the coupling between actuator and structure in the presented chapter 5.3. Despite the advantages presented, no conclusion about the ability to simulate *Lamb* waves can be made. Therefore, the isogeometric finite element is compared to two other high order finite element approaches in the next chapter. The convergence rate of the three numerical finite element approaches to solve a *Lamb* wave propagation problem is studied.

4 Comparison and evaluation of the NURBS element with alternative approaches for *Lamb* wave simulation

4.1 Introduction

In this chapter the isogeometric elements are used to model *Lamb* wave propagation problems. The chapter starts with a three-dimensional problem. A plate with a conical hole is modelled and the results are used to illustrate the ability of the isogeometric finite elements to describe the physical behavior of *Lamb* waves.

Furthermore, the isogeometric elements are compared to two other higher order finite element approaches based on *Lagrange* and *Legendre* polynomials. These three different approaches are tested utilizing a simple two-dimensional benchmark setup. The reference solution to evaluate the performance of the higher order schemes is found using an adapted analytical solution (see section 2.2) [156]. The goal of this chapter is to describe the convergence properties of the three numerical approaches. Thus, it is possible to quantify which method provides the best performance regarding *Lamb* wave propagation problems. While different spatial discretization techniques are tested, the same time integration scheme is applied to all analysed cases, ensuring a good comparability of the results. Meaning, the computational times are not directly taken into account, since the considered temporal discretization technique is not necessarily well suited for each of the analysed finite element schemes. The number of degrees-of-freedom required, for a certain level of accuracy are compared. In addition, the number of non-zero elements in the system matrices is examined, measuring the memory storage requirements of each method. Moreover, the effect of higher order inter-element-continuity is tested, which is a specific feature of isogeometric finite elements.

In the last part of this chapter the results gained from the two-dimensional test are used to model a three-dimensional plate with a conical hole. This model is seen as an example of a more complex geometry and allows for both reflections at the boundaries of the structure and a mode conversion at the defect. The more advanced test structure is used to show that the guideline for an optimal discretization obtained in the previous section can easily be generalized even to three-dimensional problems involving more complex parts, like conical holes.

4.2 A brief overview of the shape functions

The isogeometric elements are compared with two other higher order finite element types. The section provides a brief summary of the two shape function types, namely the *Lagrange* polynomials and the normalized integrals of the *Legendre* polynomials. For more details its refer to [40, 130].

4.2.1 Spectral finite element method and Lagrange polynomials

Spectral finite elements are based on a set of *Lagrange* polynomials utilizing a specific nodal distribution on the interval $[-1, +1]$. The $(p + 1)$ one-dimensional basis functions are formally defined by

$$N_n^{\text{Lagrange}, p}(\xi) = \prod_{j=1,\, j\neq n}^{p+1} \frac{\xi - \xi_j}{\xi_n - \xi_j}, \quad n = 1, 2, \ldots, p+1. \tag{4.1}$$

Therein the nodal distribution is described by ξ_i with $i = 1, \ldots, (p+1)$ as

$$\xi_i = \begin{cases} -1 & \text{if} & i = 1 \\ \xi_{0,i-1}^{Lo,p-1} & \text{if} & 2 \leq i < p+1 \\ +1 & \text{if} & i = p+1 \end{cases}. \tag{4.2}$$

Determined by the set of roots $\xi_{0,a}^{Lo,p-1}$ with $a = 1, \ldots, (p-1)$ of the $(p-1)$-order *Lobatto* polynomial

$$Lo_{p-1}(\xi) = \frac{1}{2^p p!} \frac{d^{p+1}}{d\xi^{p+1}} \left[\left(\xi^2 - 1 \right)^p \right]. \tag{4.3}$$

This nodal distribution, referred to as *Gauss-Lobatto-Legendre* (GLL) grid, offers in conjunction with the GLL-quadrature rule the possibility to diagonalize the mass matrix in an elegant way [76, 130]. This lumping procedure provides significant savings in computational time if an explicit time integration scheme is used, while much less memory is required to save the inverted mass matrix.

4.2.2 p-Version of the finite element method and normalized integrals of the Legendre polynomials

To construct higher order ansatz functions according to the p-version of FEM Szabó and Babuška have favored a hierarchical basis, meaning that all shape functions of lower order are included in the set of higher order shape functions. The presentation of those shape functions follows [43] and [145] closely. Generally speaking, hierarchic shape functions are based on the normalized integrals of the *Legendre* polynomials.

Following the approach first established by Szabó and Babuška [145] it is shown how hierarchic basis functions can be generated up to any desired polynomial degree. The p-version of the finite element method presented here is based on *Legendre* polynomials $L_n(x)$. They satisfy *Bonnets* recursion formula

$$L_{n+1}(x) = \frac{1}{(n+1)} \left[(2n+1)x L_n(x) - n L_{n-1}(x) \right], \quad n = 1, 2, 3, \ldots \quad -1 \leq x \leq 1 \tag{4.4}$$

which is very well suited for a computer implementation. Here n denotes the polynomial degree. If Equation (4.4) is used to generate the *Legendre* polynomials, the recursion must start with the first two polynomials

$$L_0(x) = 1, \tag{4.5}$$
$$L_1(x) = x. \tag{4.6}$$

In order to construct shape functions for p-elements the following normalized integrals of the *Legendre* polynomials $\Phi_n(\xi)$ (modified *Legendre* polynomials) are used

$$\Phi_n(\xi) = \sqrt{\frac{2n-1}{2}} \int\limits_{x=-1}^{\xi} L_{n-1}(x)dx = \frac{1}{\sqrt{4n-2}} \left[L_n(\xi) - L_{n-2}(\xi) \right], \quad n = 2, 3, \dots. \tag{4.7}$$

Thus, the value of the modified *Legendre* polynomials is equal to zero at the boundaries $\xi = \mp 1$. The linear *Lagrange* polynomials constitute the first two shape functions $N_1^{\text{Legendre}}(\xi)$ and $N_2^{\text{Legendre}}(\xi)$ as

$$N_1^{\text{Legendre}}(\xi) = N_1^{\text{Lagrange}, 1}(\xi) = \frac{1-\xi}{2}, \tag{4.8a}$$

$$N_2^{\text{Legendre}}(\xi) = N_2^{\text{Lagrange}, 1}(\xi) = \frac{1+\xi}{2}. \tag{4.8b}$$

They are commonly called nodal modes or nodal shape functions. They can be thought of as being external, since they are responsible for ensuring C_0-continuity between adjacent elements. Higher order ansatz functions $N_n(\xi)$ of polynomial degree p are generated from Equation (4.7) in the following way

$$N_n^{\text{Legendre}}(\xi) = \Phi_{n-1}(\xi), \qquad n = 3, 4, \dots, p+1. \tag{4.9}$$

They are also referred to as internal modes or bubble modes, because the corresponding degrees-of-freedom are not directly related to the internal degrees-of-freedom of adjacent finite elements

$$N_n^{\text{Legendre}}(\mp 1) = 0, \quad n = 3, 4, \dots, p+1. \tag{4.10}$$

An important property of the hierarchical set of shape functions, which derives from the orthogonality of the *Legendre* polynomials, is the condition

$$\int\limits_{-1}^{+1} \frac{dN_n^{\text{Legendre}}}{d\xi} \frac{dN_m^{\text{Legendre}}}{d\xi} d\xi = \begin{cases} 1 & \text{if } n = m, \\ 0 & \text{if } n \neq m. \end{cases} \tag{4.11}$$

This property results in a sparse structure of the stiffness matrix, which is the reason why the normalized integrals and not the polynomials themselves are used to construct shape functions for higher order finite element approaches.

4.2.3 Comparison of the ansatz functions

The plots in Figure 4.1 illustrate the presented shape functions of a one-dimensional element corresponding to the polynomial degrees 2, 3 and 4. While the *Lagrange* and modified *Legendre* graphs only cover the domain of one element, the NURBS plots involve two elements in order to show their transition behavior at the element boundary. One easily notes the higher order of continuity (C^{p-1}) at the boundary.

(A) *Lagrange* $p = 2$ **(B)** modified *Legendre* $p = 2$ **(C)** NURBS $p = 2$

(D) *Lagrange* $p = 3$ **(E)** modified *Legendre* $p = 3$ **(F)** NURBS $p = 3$

(G) *Lagrange* $p = 4$ **(H)** modified *Legendre* $p = 4$ **(I)** NURBS $p = 4$
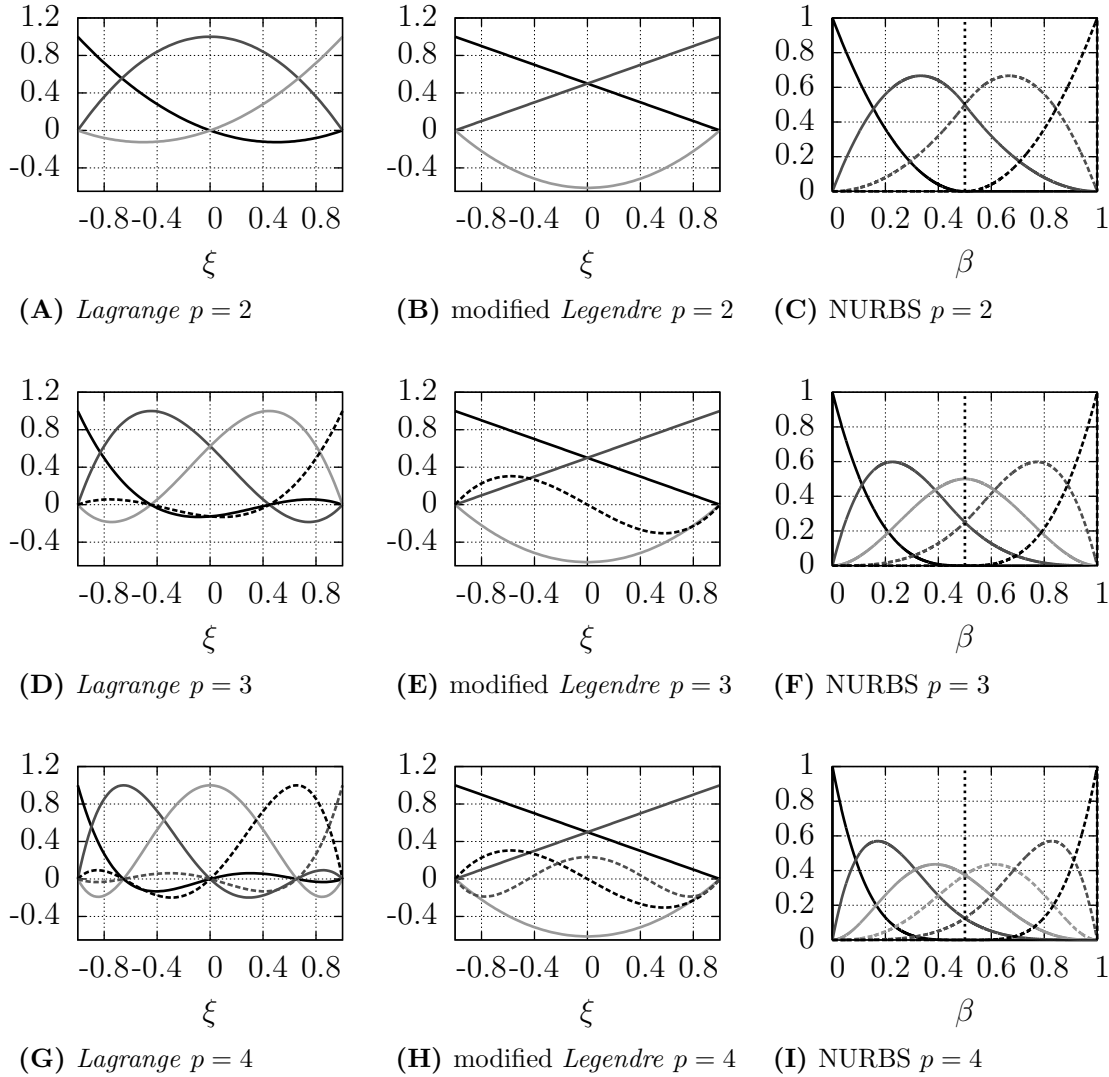
Figure 4.1: Comparison of different order of ansatz function sets. The dashed central line in the figures of the third column concerning the NURBS shape functions, marks the boundary of two adjacent elements. Observe the higher continuity (C^{p-1}) between adjacent isogeometric finite elements, while spectral- and p-element shape functions exhibit only C^0-continuity at their element boundaries.

On the left column, it can be seen that the standard *Lagrange* polynomials using a GLL nodal distribution do not exceed the value of $+1$. For both *Lagrange* and NURBS elements this is the reason why no *Runge*-phenomenon is encountered. The approach based on *Lagrange* polynomials is commonly referred to as SEM. The modified *Legendre* polynomials, constituting the basis for the p-FEM presented, in the middle column of Figure 4.1 are constructed using a hierarchical basis. Shape functions of lower polynomial degrees are also present in higher order approaches. This is an attractive feature of this shape functions set, since the hierarchy of the basis functions has also an immediate consequence on the structure of the resulting system matrices.

All system matrices corresponding to the polynomial orders 1 to $p - 1$ are sub-matrices of the system matrix corresponding to polynomial degree p. The right column displays the NURBS basis functions, which have higher order continuity between element boundaries

as can be seen at $\beta = 0.5$. In addition, all function values are positive in the element domain and each graph has at most one local maximum while the sum of all polynomials at an arbitrary location β is equal to one.

In contrast to the SEM-approach, the degrees-of-freedom of the p-version of FEM and N-FEM do not describe nodal displacements. Hence, for these two methods a more involved post-processing is needed to evaluate the mechanical displacement field, for instance. In Table 4.1 a comparison regarding the properties of the presented one-dimensional shape function sets is summarized.

Table 4.1: Comparison of the properties of different types of ansatz functions for the one-dimensional case.

	SEM	p-FEM	N-FEM
Inter-element-continuity	C^0	C^0	C^{p-1} or less
Standard element domain	$[-1, 1]$	$[-1, 1]$	$[0, 0.5]$ or $[0.5, 1]$
Physical interpretation of the degrees-of-freedom	yes mechanical displacements	none unknowns of shape function ansatz	none control point displacements
Common degrees-of-freedom of adjacent elements	1	1	p or less
Function values can be negative	Yes	Yes	No

4.3 Model and methodology of the convergence study

4.3.1 Model definition

In order to compute ultrasonic wave propagation efficiently, it is essential to have a guideline of how to choose the polynomial degree and/or the mesh density for a given problem. In the following convergence studies the influence of the discretization on the quality of the numerical solution is shown.

For this purpose, a two-dimensional plane strain model is considered. The geometry and the boundary conditions are depicted in Figure 4.2. The length of the aluminum plate is given as $l_p = 0.5\,\mathrm{m}$, the thickness as $h = 2\,\mathrm{mm}$. The material properties are summarized in Table A-1. The length of the plate guarantees that no reflections from the right boundary are effecting the signals at the points of measurement during the simulation time. *Lamb* waves are excited using a pair of concentrated line loads on both, the top and the bottom surfaces of the plate. In the two-dimensional model these loads are modeled as point forces acting in the x_3-direction. Their time-dependent amplitudes follow a sine burst signal given in Equation (4.17). This kind of pulse has the advantage that the frequency content is narrow-banded. The number of cycles within the signal n determines the width of the excited frequency band around the central frequency f. The higher n, the narrower the bandwidth becomes. Applying concentrated loads at the top and bottom surfaces allows us to exploit the advantages of a mono-modal excitation, which means that only a single mode is present at a time if $f \cdot h < 1.5\,\mathrm{MHzmm}$ (see Figure 2.2B). In order to generate a

signal containing only the A_0-mode both forces have to act in the same direction, meaning they have to be in-phase. If the two loads are out-of-phase a pure S_0-mode is generated. An excitation frequency of $f = 477.5\,\mathrm{kHz}$ is chosen because around this frequency value the dispersion-effect is comparatively low for both modes regarding a plate thickness of $h = 2\,\mathrm{mm}$ (see Figure 2.2A).
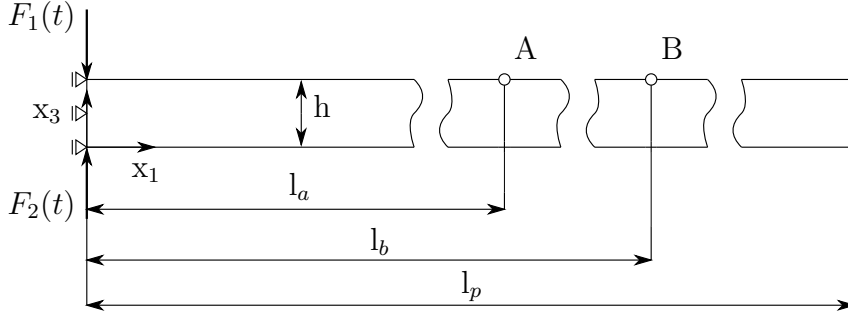

Figure 4.2: Two-dimensional model with loads and boundary conditions for the convergence study. Two point forces $F_1(t) = \hat{F} \sin \omega t \sin^2\left(\frac{\omega t}{2n}\right)$ and $F_2(t) = aF_1(t)$ are applied, with $a = 1$ for the excitation of a purely symmetric *Lamb* wave mode (S_0) and $a = -1$ if the anti-symmetric mode (A_0) is considered. The dimensions of the aluminium (see Table A-1) plate are : $l_a = 100\,\mathrm{mm}$, $l_b = 200\,\mathrm{mm}$, $l_p = 500\,\mathrm{mm}$, $h = 2\,\mathrm{mm}$.

At the left boundary ($x_1{=}0$) of the model symmetric boundary condition are applied in order to exploit the symmetry of the problem. With this set up the assumptions of the analytical solution presented in section 2.2 are fulfilled. The convergence behavior of the numerical results is evaluated with respect to the analytical reference solution [167]. The time history of the displacement field is saved at the location of the two points A (u_A) and B (u_B) at the top surface (Figure 4.2). The first one is located at $x_1 = l_a$ and the second at $x_1 = l_b$.

4.3.2 Methodology to evaluate the quality of the numerical results

To determine the quality of the finite element solution the time of flight t_c of the propagating *Lamb* wave packet between the points A and B is utilized (Figure 4.3). The time of flight computed using the finite element method ($t_{c_{num,type}}$) is compared to the value given by the analytical solution ($t_{c_{ana}}$). In order to extract this value from the finite element or analytical solution, the time signal of the displacement at the regarded point (A or B) is subjected to an *Hilbert* transform

$$H_{A,B}(u_{A,B}(t)) = \frac{1}{\pi} \int_{-\infty}^{\infty} u_{A,B}(\tau) \cdot \frac{1}{t - \tau} \, d\tau. \tag{4.12}$$

Using the *Hilbert* transform $H_{A,B}$ the envelope $e_{A,B}$ of the time displacement history $u_{A,B}$ can be computed. The time-of-flight is then evaluated by comparing the position of the centroid of the envelop of the time signal at these two points. The envelop can be computed

deploying the following relation

$$e_{A,B}(t) = \sqrt{H_{A,B}(u_{A,B}(t))^2 + u_{A,B}(t)^2} \qquad (4.13)$$

and the coordinate of its centroid is obtained computing the statical moment of the envelop

$$t_{A,B} = \frac{\int\limits_0^{t_{end}} e_{A,B}(t) \cdot t \, dt}{\int\limits_0^{t_{end}} e_{A,B}(t) \, dt} . \qquad (4.14)$$

The time-of-flight t_c between points A and B serves as a measure of the quality of the numerical results. It can be computed as the difference [41, 164]

$$t_c = t_B - t_A . \qquad (4.15)$$

This method is quite well suited to determine the convergence behavior of *Lamb* wave propagation problems since the dispersion is taken into account. Because the time-of-flight of the analytical reference ($t_{c_{ana}}$) as well as the time-of-flight of the numerical solution ($t_{c_{num,type}}$) are equally dependent on the dispersion of the *Lamb* wave packet, no additional errors are introduced through the method applied to evaluate the computed results.
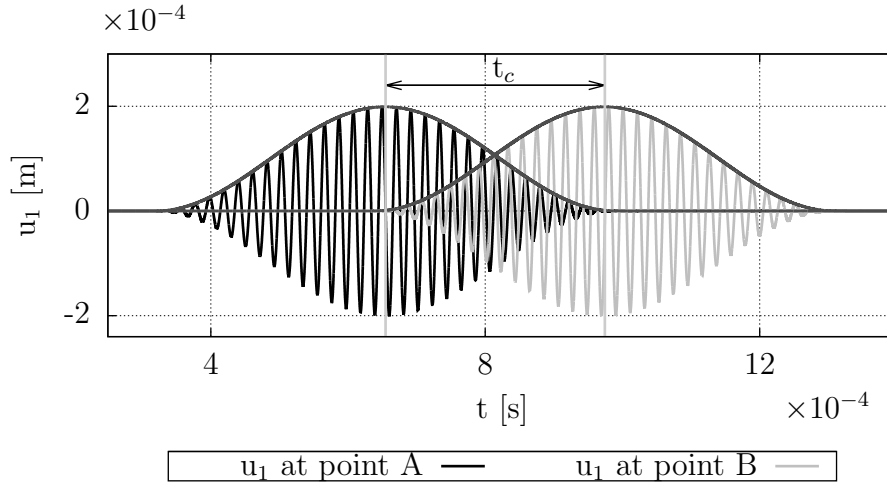

Figure 4.3: Time-of-flight as difference of the centroid of two Hilbert envelopes at point A and B for the S_0-mode. Example for the described model (Figure 4.2) for $f = 477.5\,\text{kHz}$.

4.3.3 Discretization set up

In order to isolate the influence of the discretization in x_1- and x_3-direction with respect to the quality of the results, two different convergence studies are executed.

Firstly, the discretization in the direction of the traveling wave is investigated (see section 4.4.1) using a variable number of degrees-of-freedom in x_1-direction and a fixed amount in x_3-direction. In our experience it is sufficient to discretize the thickness of the plate utilizing one finite element with a fixed polynomial degree of $p_{x_3} = 4$ [130]. Thus, the discretization over the thickness of the plate will not noticeable pollute the computed time

signal, as the displacement field through the thickness of the plate is well resolved by utilizing a quartic polynomial. To determine the influence of the discretization in x_1-direction the number of finite elements in this direction is varied using a h-refinement for the spectral and p-elements and a k-refinement [30] for the isogeometric elements. This refinement is repeated for various polynomial degrees $p_{x_1} = 2, 3 \ldots, 6$. To evaluate the quality of the numerical solution of the different finite element approaches the relative error depending on the number of "nodes" per wavelength (χ) is computed. For the case of SEM these "nodes" correspond to actual nodes at known locations. When dealing with N-FEM or p-FEM they do not represent geometrical nodes. These "nodes" do not retain any physical meaning (see Table 4.1) and they are only a distinct measure of the mesh density. For a given model discretized with a regular mesh the value of χ is determined using [41]

$$\chi_{S_0, A_0} = \frac{\text{degrees-of-freedom}}{2(p_{x_3+1})l_p} \cdot \lambda_{S_0, A_0}. \tag{4.16}$$

p_{x_3} denotes the polynomial degree in x_3-direction, l_p stands for the length of the plate and λ_{S_0} or λ_{A_0} are the wavelength of the symmetric and anti-symmetric *Lamb* wave mode, respectively. The wavelengths of the A_0- and S_0-mode are taken from the phase velocity curves (Figure 2.2A) at $fh_p = 0.955\,\text{MHzmm}$. The relative error is determined comparing the numerical to the analytical solution. Secondly, the impact of the discretization in x_3-direction is investigated (see section 4.4.2). In order to quantify the influence of the discretization over the thickness of the plate, the numerical model is discretized utilizing a fixed number of elements both in x_1- and x_3-direction. The discretization in the direction of the traveling wave is chosen according to the results of the first convergence study such that it ensures an unaffected evaluation of the computed results. Thus, a discretization utilizing more than 20 "nodes" per wavelength and a polynomial degree of $p_{x_1} = 6$ is chosen. The convergence study is performed conducting a p-refinement with $p_{x_3} = 1, \ldots, 8$. To evaluate the quality of the numerical solution of the different finite element approaches the relative error depending on the polynomial degree p_{x_3} is computed.

After determining the optimal discretization parameters of the three presented finite element approaches these methods are compared with standard linear elements, utilizing both fully integrated and selectively reduced integrated elements (see section 4.4.3).

The numerical time integration scheme is only adjusted such that the effects of an inaccurate time integration are negligible and thus barely contribute to the numerical errors. In this context, preliminary studies concerning different time integration schemes have shown that an explicit fourth order *Runge-Kutta* type time integration method offers the best accuracy compared to a central difference or a standard *Newmark* method. Thus, for our convergence studies the ode45-solver provided in MATLAB is used. Hence, only the quality of the spatial discretization is evaluated.

The results and conclusion are discussed in detail in the following section where also guidelines are derived to estimate the quality of the numerical solution using different higher order approaches a priori.

4.4 Results and discussion

4.4.1 Discretization in the direction of the wave propagation

(A) $p_{x_1}=2$

(B) $p_{x_1}=3$

(C) $p_{x_1}=4$

(D) $p_{x_1}=5$
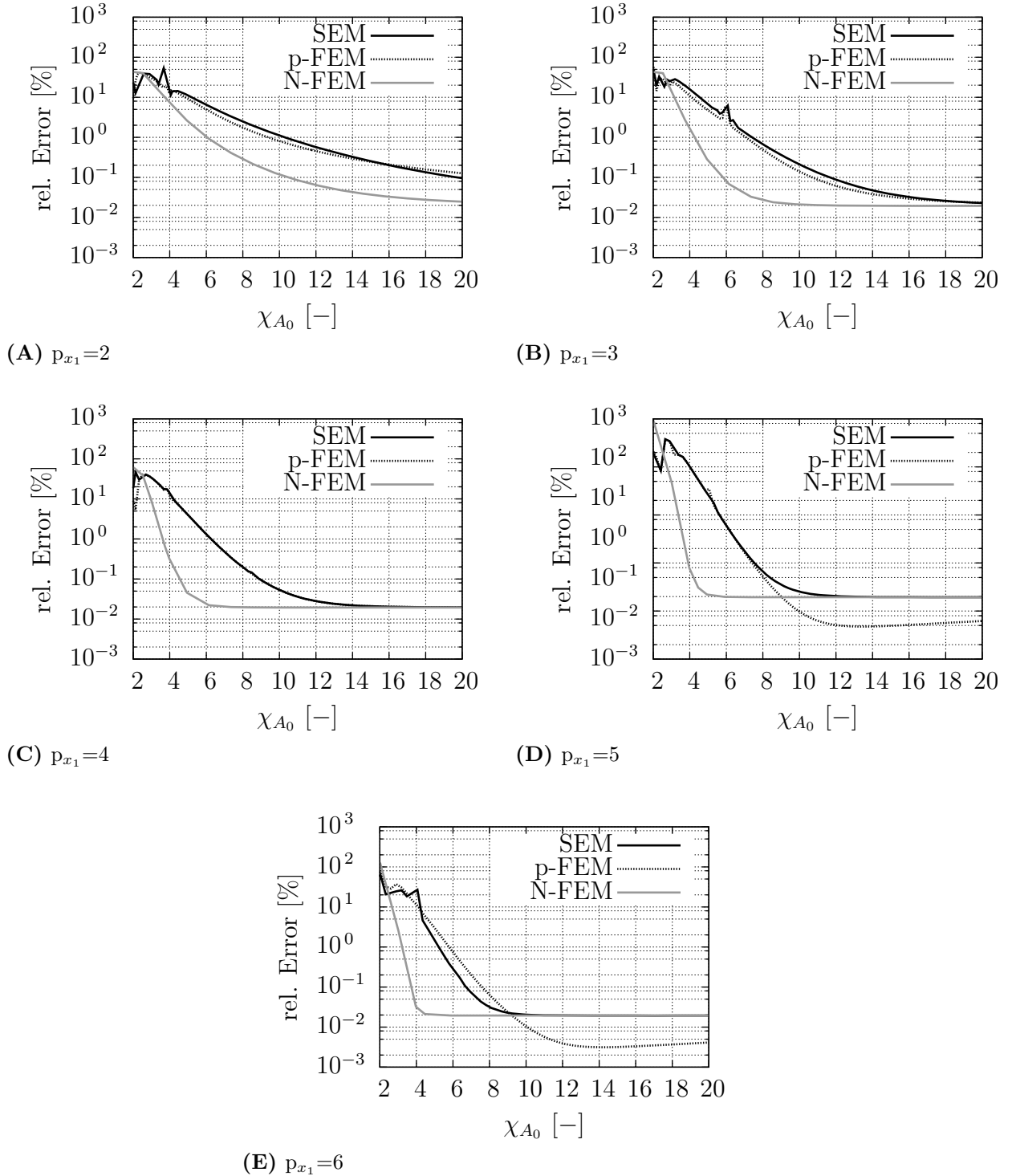
(E) $p_{x_1}=6$

Figure 4.4: Convergence curve for the A_0-mode.

The Figures 4.4 and C–1 (see Appendix C) display the results of the convergence study with respect to a varying polynomial degree in global x_1-direction.

The Figures 4.4 the findings obtained for the A_0- and the Figures C–1 for the S_0-mode. The curves are steady except for small peaks experienced in the convergence curves of SEM and p-FEM. This behavior can be attributed to local element eigenfrequencies, as conclusively explained in [130]. All curves converge faster for higher polynomial orders.

It has to be noted that the convergence rate of the N-FEM elements is significantly higher than for SEM and p-FEM ones. The latter two approaches show a very similar convergence behavior. Additional studies concerning the convergence rate of C^1- and C^0-continuous isogeometric finite elements are conducted in section 4.4.4.

Considering the accuracy of the solution it is observed that the relative error reaches the same order of magnitude for all three higher order finite element approaches. However, the p-elements offer the highest absolute accuracy.

Assuming that a relative error threshold of 1% is acceptable from an engineering point of view all proposed higher order finite element approaches need considerably less than 20 "nodes" per wavelength, typically mentioned in literature [101]. Since the wavelength of the S_0-mode is longer as that of the A_0-mode the convergence curves of the anti-symmetric mode are more relevant when judging the quality of the overall solution. Normally, both types of *Lamb* waves are excited if collocated actuators cannot be used. Then the mesh parameters have to be chosen such that the anti-symmetric mode is resolved.

In Figure 4.5 the number of non-zero elements (nnz) of the system matrices $\mathbf{K}$ and $\mathbf{M}$, for each polynomial degree when reaching the mentioned threshold for the anti-symmetric mode case, are displayed. All values are normalized with respect to the spectral element solution for the polynomial degree $p_{x_1} = 2$. The number of non-zero elements serves as a measure of the memory storage requirements for each method. As can be inferred from the graphs $p_{x_1} = 3$ is optimal for all spectral, p-version and isogeometric finite elements. Due to their fast convergence N-FEM elements require the least degrees-of-freedom which results in a reduced demand of memory to store the system matrices. The storage requirements of the spectral finite elements and the p-elements do not differ significantly.
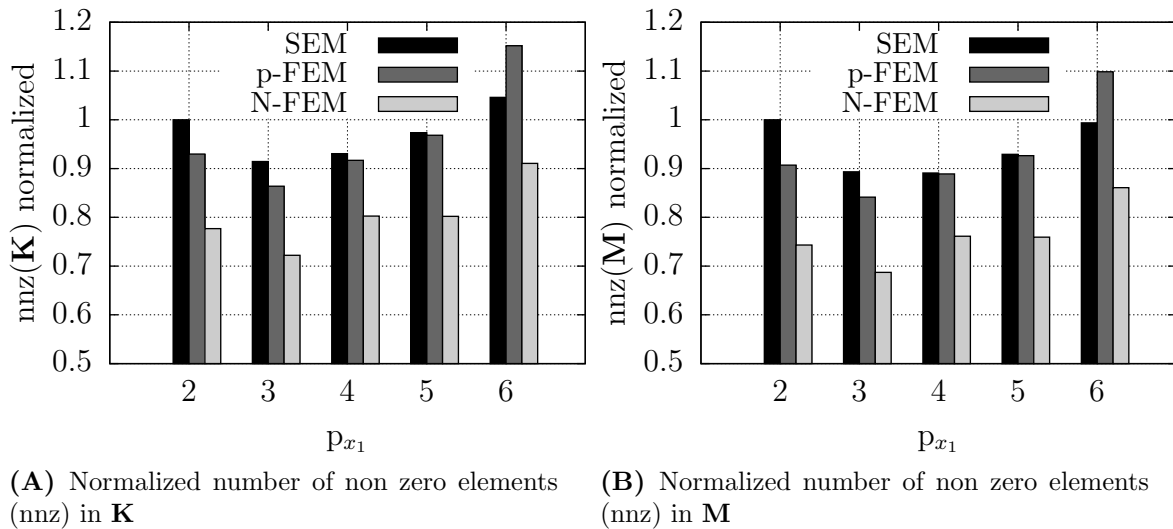

(A) Normalized number of non zero elements (nnz) in $\mathbf{K}$

(B) Normalized number of non zero elements (nnz) in $\mathbf{M}$

Figure 4.5: Normalized memory storage requirements for the models reaching the relative error threshold of 1%.

4.4.2 p-Refinement over the thickness of the plate

After the optimal polynomial degree in the direction of the traveling wave has been determined a second convergence study is conducted in order to determine the optimal polynomial order in thickness direction of the plate. The discretization is set up as described in section 4.3.3. The results of the simulations are depicted in Figure 4.6. The curves are steady except for a small overshoot for spectral and isogeometric finite elements.
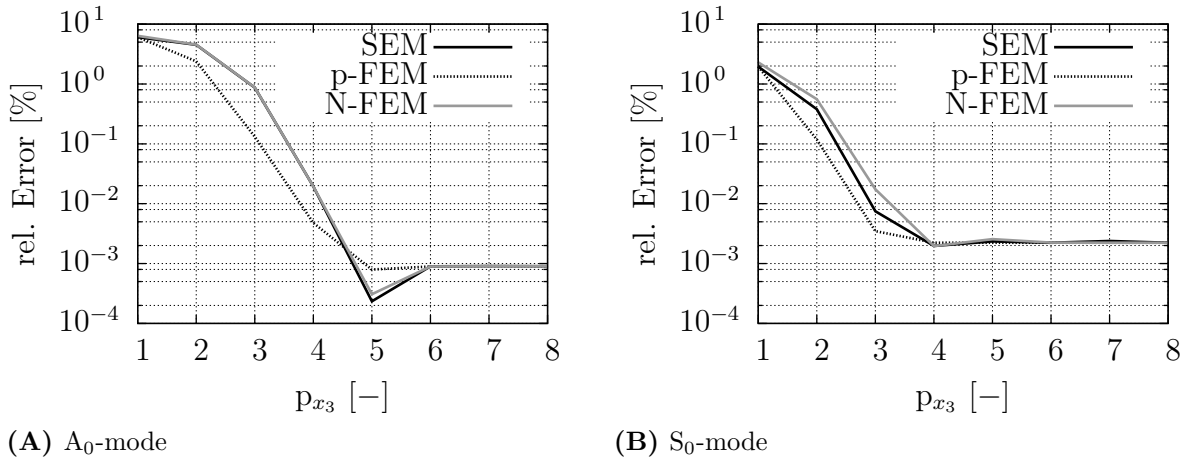

(A) A_0-mode **(B)** S_0-mode

Figure 4.6: Convergence study concerning the discretization in thickness direction of the plate

It can be seen that the convergence rate of the p-version finite elements is for both the A_0- and S_0-mode the highest. The SEM and N-FEM have an equal convergence behavior for the A_0-mode. For the S_0-mode the isogeomtric finite element shows the lowest rate of convergence. This behavior agrees with the findings in section 4.4.4. The advantage of the higher inter-element-continuity to the convergence behavior of the isogeometric finite element cannot be used because only one element is deployed over the thickness the plate.

Regarding the accuracy all elements reach a similar relative error at $p_{x_3} = 6$. Taking a tolerance limit of 1% into account the anti-symmetric mode is resolved with a polynomial order $p_{x_3} = 3$ (Figure 4.6A), while the symmetric mode demands a value of $p_{x_3} = 2$ (Figure 4.6B). Since, the A_0-mode is primarily a flexural wave, higher polynomial degrees are needed to avoid stiffening effects caused by the locking phenomenon, still present in the model for the lower order approximations.

The combined results taken from Figure 4.4 - 4.6, provide a good foundation to formulate a guideline about how an appropriate discretization is to be generated. The solution depicted in Figure 4.6A is dependent on both polynomial degrees used ($p_{x_1} = 6$, $p_{x_3} = 1, \ldots, 8$). The results obtained utilizing $p_{x_3} = 3$ barely meet the relative error threshold. Since the higher order mixed product terms of the shape functions, depending on both powers m, n of the one-dimensional ansatz functions [167], influence the accuracy of the computed results, $p_{x_3} = 4$ is chosen as optimal degree instead of $p_{x_3} = 3$. Additionally, the effects of locking are kept to a minimum.

Surprisingly, for all tested finite elements a configuration of $p_{x_1} = 3$ and $p_{x_3} = 4$ is a suitable choice to meet the chosen error criterion for both the A_0- and the S_0-mode and minimizing the amount of non-zero elements in the system matrices.

4.4.3 Comparison of the higher order approaches to conventional linear finite elements

In this section the results obtained using the proposed higher order finite elements are compared to the results computed deploying conventional linear 4-noded quadrilateral finite elements. In literature it is widely accepted that 20 nodes per wavelength are sufficient to obtain good accuracy even for conventional low order finite elements [10, 101]. In the course of this section this statement is examined and its validity is checked. The relative error curves obtained utilizing the optimal polynomial degree template for the higher order approaches (SEM: $p_{x_1} = 3$, $p_{x_3} = 4$; p-FEM: $p_{x_1} = 3$, $p_{x_3} = 4$; N-FEM: $p_{x_1} = 3$, $p_{x_3} = 4$) are contrasted with the solutions computed deploying conventional fully or selectively reduced integrated linear finite elements. The model depicted in Figure 4.2 is discretized with different types of linear finite elements and the obtained results are scrutinized. Type one has been labeled "linear undistorted fully integrated". This is to say that neither an hourglass control scheme nor linear finite elements having an aspect ratio of higher than 1.4 are utilized. If the aspect ratio exceeds a value of 1.4 the number of elements in thickness direction is increased by one. Thus, up to 14 elements over the thickness are deployed to prevent element distortion (high aspect ratios). The second numerical model using linear finite elements is termed "linear distorted fully integrated". This model is similar to the first one, only that now aspect ratios of 5 or higher are allowed. In this case a mesh density of 4 linear elements over the thickness is chosen. This corresponds to 5 nodes in thickness direction of the plate, which is identical to the higher order approaches utilizing $p_{x_3} = 4$. The third model deploying conventional 4-noded quadrilateral elements is labeled "linear undistorted reduced integrated". In comparison to the first type the element matrices are numerically integrated utilizing a selective reduced integration scheme. That is to say, that only those terms of the total elastic potential referring to the shear energy are reduced integrated. This prevents the shear energy from being overestimated. Due to this numerical trick the stiffness matrix becomes rank-deficient and displacement modes, needing no energy, can evolve. To avoid these zero energy modes an hourglass control algorithm based on the artificial stiffness method as proposed in [47] is chosen. The solutions for this special type of integration are computed using the commercial software package ABAQUS 6.7-2.

The results of the verification process are depicted in Figure 4.7A (A_0-mode) and 4.7B (S_0-mode). The convergence curves of the three linear finite element models are steady, except for a peak for the selectively reduced integrated case. An error-reducing influence of low aspect ratios as well as linear finite element using a selectively reduced integration in conjunction with a suitable hourglass control scheme is to be seen in the convergence characteristics of the anti-symmetric *Lamb* wave mode.

Since the A_0-mode resembles a flexural wave and linear finite elements are prone to shear locking effects a significant improvement in the relative error can be observed when using linear finite elements that are either "undistorted" and/or selectively reduced integrated. Utilizing those approaches the shear energy is not significantly overestimated. Regarding the convergence curves of the anti-symmetric mode, only undistorted linear finite elements are able to reach the designated error criterion of 1 % (see Figure 4.7A).

Although up to 14 finite elements are deployed over the thickness of the plate the solution does still suffer from the locking effect and cannot reach an accuracy similar to the higher order schemes. The error in the case of 20 nodes per wavelength is equal to 3.63 % for the

"distorted" linear fully integrated finite elements and 2.24 % for the "undistorted" ones. Considering the anti-symmetric mode the reduced integration of the shear energy term pays off and a clear improvement of the results can be seen in Figure 4.7A. The relative error compared to the fully integrated linear FE-model is drastically reduced to 0.51 %. However, the accuracy of all higher order finite element approaches is still superior. By using a selectively reduced integrated linear finite element the 1 % relative error bound is reached for round about 14 nodes per wavelength.

Scrutinizing the S_0-mode neither a positive influence of low aspect ratios nor of an improvement due to selectively reduced integration can be observed. In the contrary the chosen hourglass control deteriorates the results with less than 17 nodes per wavelength. The convergence behavior of the symmetric mode is almost equivalent for both fully integrated linear finite element approaches. For the reduced integrated elements the results for the symmetric *Lamb* wave mode in the range of 5-17 nodes per wavelength are even worse than for fully integrated linear elements. The explanation for this behavior is based on the default hourglass control ABAQUS employs. If different schemes than the artificial stiffness method proposed in [47] are used, the relative error can be reduced even further. Preliminary studies have shown that an enhanced hourglass control algorithm is an appropriate choice. This approach is based on the enhanced assumed strain and physical hourglass control methods proposed by Belytschko and Bindeman [15]. Then all three curves corresponding to the finite elements being available in commercial software packages are virtually coincident. But the difference between a converged solution for 30 nodes per wavelength and the analytical reference solution is not altered significantly. The relative error in the case of 20 nodes per wavelength of both distorted and undistorted elements is equal to 1.91 %. This behavior was to be expected since the S_0-mode is merely a longitudinal wave which is not significantly influenced by locking effects. The 1 % error boundary is reached at 26 nodes per wavelength in all three cases.

Regardless of the improved accuracy in comparison to the fully integrated finite elements the convergence rate of the A_0- and S_0-mode is still low. It is not enough to specify a certain number of nodes per wavelength, because the discretization over the thickness of the plate has to be considered as well. Additionally, if conventional low order finite elements are to be deployed a specification of the numerical integration method as well as the hourglass control algorithm is required. In general, higher order finite elements are in any case significantly more accurate than conventional low order approaches.
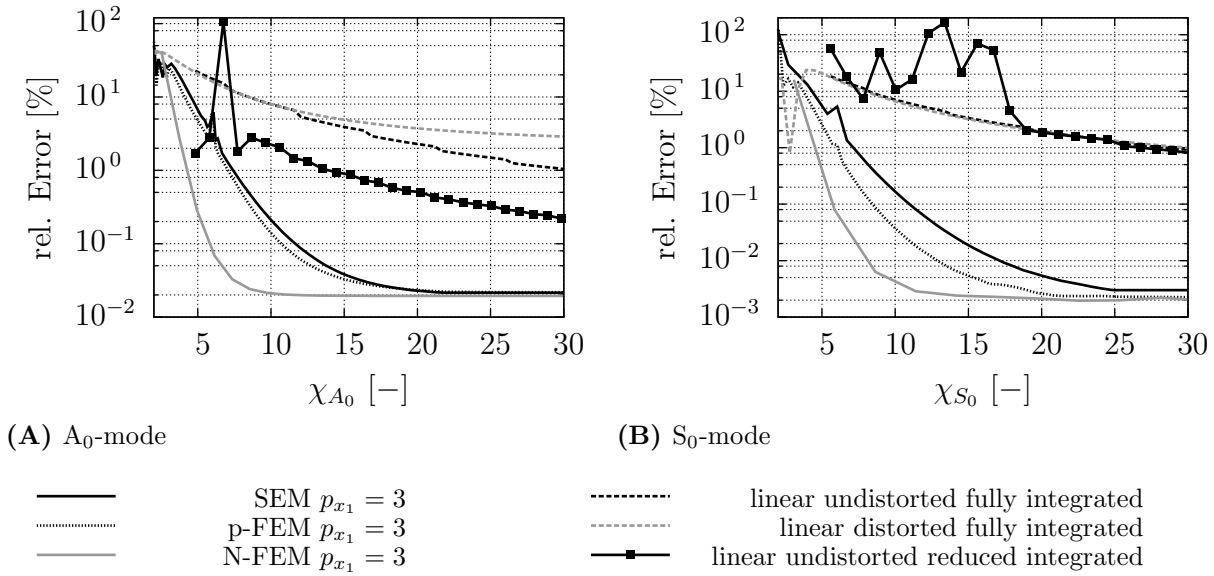
(A) A_0-mode   **(B)** S_0-mode

——————	SEM $p_{x_1} = 3$	- - - - - -	linear undistorted fully integrated
··············	p-FEM $p_{x_1} = 3$	- - - - - -	linear distorted fully integrated
——————	N-FEM $p_{x_1} = 3$	—■—■—	linear undistorted reduced integrated

Figure 4.7: Comparison of the convergence curves for the proposed higher order finite
element method schemes ($p_{x_3} = 4$) and conventional linear finite elements.

4.4.4 Influence of the inter-element-continuity to the convergence rate

In this section the influence of the inter-element-continuity on the convergence rate is
investigated. The model setup is equal to the previous studies. The polynomial order
in thickness direction is chosen as $p_{x_3} = 4$. Two different inter-element-continuities in
x_1-direction are chosen; C^1- and C^0-continuity. The C^0-continuity corresponds to the
standard finite element inter-element-continuity.

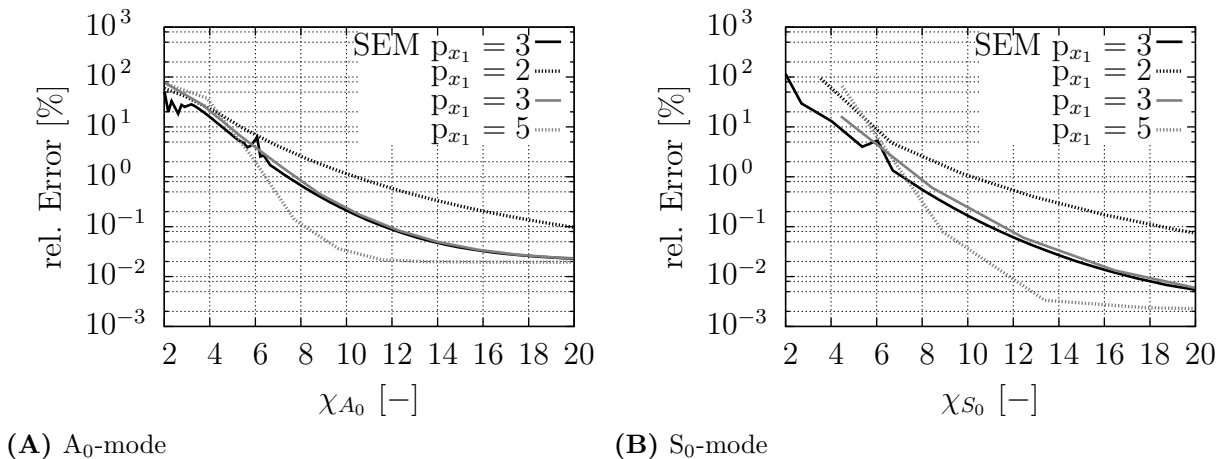**(A)** A_0-mode   **(B)** S_0-mode

Figure 4.8: Convergence curve of isogeometric elements with C^1-continuity ($p_{x_3} = 4$).

Figure 4.8 shows the result of the convergence test for the C^1-continuous isogeometric finite
elements. As reference the convergence curve of the SEM with the optimal polynomial

degree $p_{x_1} = 3$ is plotted. The convergence rate for the A_0- as well as the S_0-mode are lower in comparison to C^{p-1}-continuous isogeometric elements. They are steady and have no peaks. The convergence of the isogeometric elements of order $p_{x_1} = 3$ are almost equal to the reference curve of SEM of the same order. The accuracy of the isogeometric element in comparison to the SEM elements is lower. For the polynomial degree $(p_{x_1} = 5)$ above the reference solution the accuracy is higher. However, the maximum accuracy is equal for both the N-FEM and SEM $(p_{x_1} = 3)$.

Figure 4.9 illustrates the results of the C^0-continuous isogeometric elements. The curves are steady except the peak for $p_{x_1} = 3$ in the A_0-mode curve. This behavior can be attributed to local element eigenfrequencies and correlate to the peak in the SEM curve [130]. Again the convergence rate of order $p_{x_1} = 3$ of the A_0- and S_0-mode is almost similar to the reference SEM convergence, but the accuracy of the isogeometric finite elements is lower until they reach the maximum accuracy.
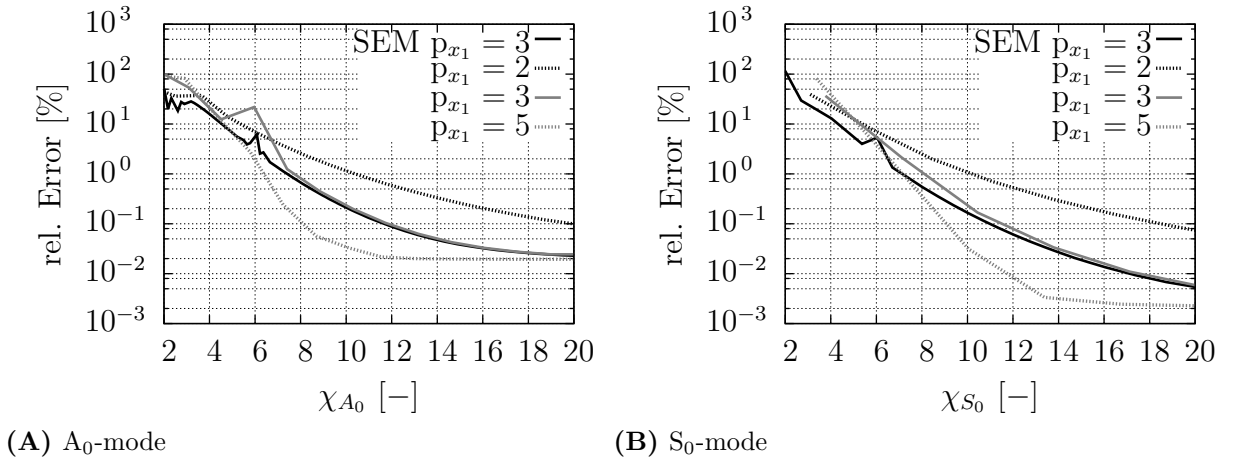

(A) A_0-mode

(B) S_0-mode

Figure 4.9: Convergence curve of isogeometric elements with C^0-continuity $(p_{x_3} = 4)$.

Generally, isogeometric finite elements with a lower inter-element-continuity exhibit worsened convergence compared to a C^{p-1}-continuous element. The maximums achievable accuracy of lower inter-element-continuity elements is not improved and equal to C^{p-1}-continuity elements. Therefore, C^{p-1}-continuity isogeometric finite elements are to be preferred when dealing with *Lamb* wave propagation. This statement agrees with Evans et al. [44] which said that "*a numerical comparison of the classical finite element and k-refinement methods revealed that the k-method has better approximation properties than the classical finite element method on a per degree-of-freedom basis, further suggesting that the k-refinement method is an accurate and robust scheme for approximating solutions to partial differential equations. These results are consistent with observations made previously based on discrete Fourier analysis and the numerical solutions of boundary value problems*".

4.5 *Lamb* wave propagation in a three-dimensional plate

A three-dimensional plate is modeled to study *Lamb* wave propagation as well as mode conversion. To this end, a conical hole is introduced to the plate at a distance of $l_h = 50$ mm from the excitation source. The plate's thickness is $h_{pl} = 2$ mm. The diameters of the hole are $d_t = 20$ mm and d_b=15 mm at the top and bottom surface. Figure 4.10 illustrates the geometry of the aluminum plate (material parameters are given in Table A-1).
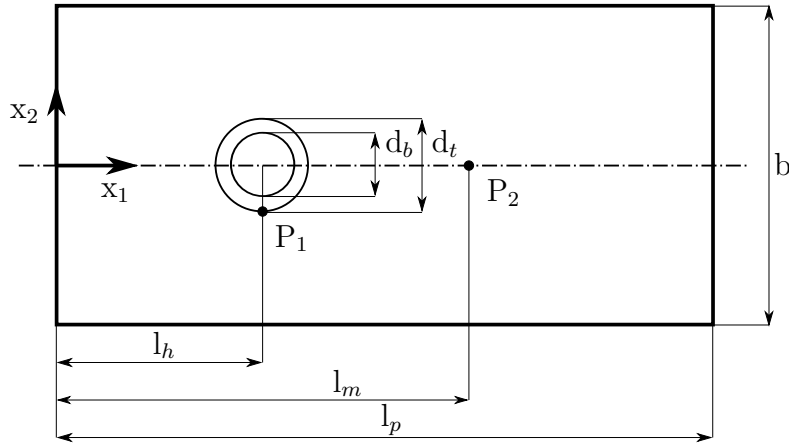
Figure 4.10: Three-dimensional aluminum plate with a conical hole (l_p =0.07 m, l_m =0.1 m, $l_h = 0.05$ m, $d_t = 0.025$ m, $d_b = 0.02$ m, $b = 0.2$ m and $h_{pl} = 2$ mm).

The plate is discretized utilizing optimal scheme which has been found in the previous section (C^{p-1}-continuous elements: 4.5 "nodes-per-wavelength", $p_{x_1} = p_{x_2} = 3$, $p_{x_3} = 4$). At the origin of the coordinate system the external loads are modeled as collocated point forces acting in x_3-direction of the plate. Their time-dependent amplitudes follow a sine burst signal

$$F(t) = \kappa \hat{F} \sin \omega t \sin^2 \left(\frac{\omega t}{2 n_P} \right), \tag{4.17}$$

where $\omega = 2 \pi f$ denotes the central circular frequency. The number of cycles is chosen as $n_P = 3$, the central frequency as 175 kHz and the force amplitude as $\hat{F} = 10^{-4}$ N. To obtain a pure S_0-mode excitation parameter κ is chosen as $\kappa = 1$ at the top and $\kappa = -1$ the bottom side, respectively. As reference solution an ABAQUS model has been created with 5 million degrees-of-freedom utilizing the linear reduced integrated finite element (C3D8R).
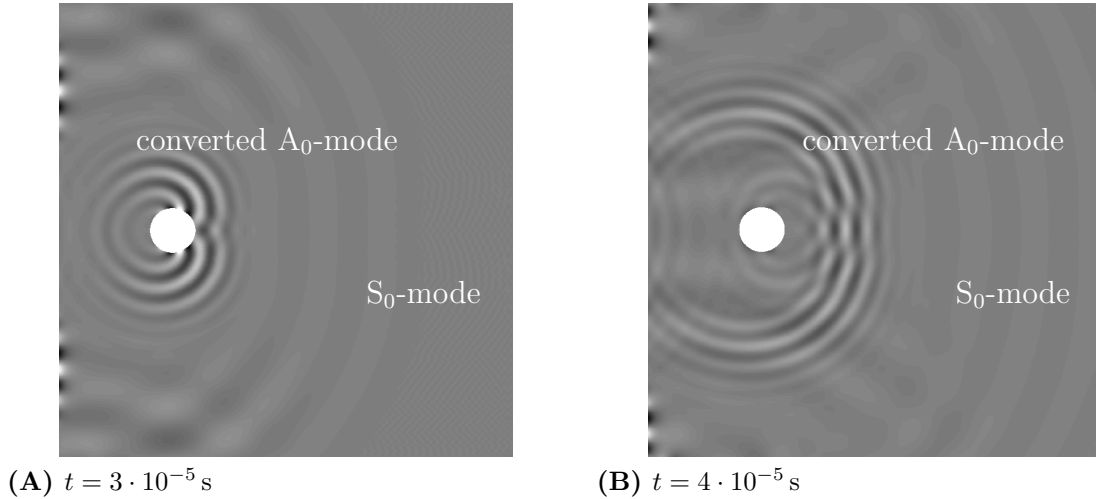
(A) $t = 3 \cdot 10^{-5}$ s

(B) $t = 4 \cdot 10^{-5}$ s

Figure 4.11: Plot of the bottom surface of a three-dimensional plate with a conical hole calculated utilizing isogeometric finite elements ($p_{x_1} = p_{x_2} = 3; p_{x_3} = 4$, $n_{dof} \approx 170000$).

Figure 4.11A and 4.11B show the u_3-displacement of the bottom surface of the plate at the time $t = 3 \cdot 10^{-5}$ s and $t = 4 \cdot 10^{-5}$ s calculated with isogeometric finite elements. After the S_0-mode mode reaches the conical hole it partially converts into an anti-symmetric A_0-mode. The center of the A_0-mode wavefront coincides with the conical hole. After the mode conversion both modes propagate separately through the plate. The isogeometric and the
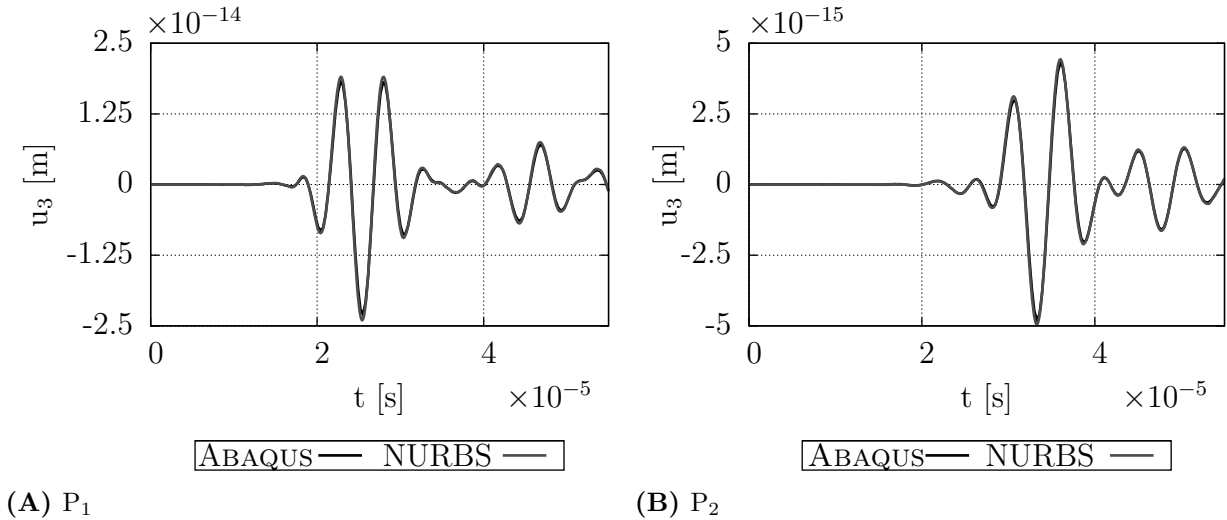

(A) P_1

(B) P_2

Figure 4.12: Time-amplitude plot at point P_1 and P_2.

ABAQUS solution are able to describe this effect. The comparison of the displacements at the point P_1 and P_2 is shown in Figure 4.12. Both points are on the bottom surface. The curves of the isogeometric and ABAQUS reference solution are in very good agreement.

The example illustrates that the new isogeometric finite elements are capable to simulate *Lamb* wave based problems. However, a recommendation for an efficient discretization has to be found and the efficiency of the NURBS element compared to other finite element approaches has to be studied. Therefore, in the next sections alternative approaches are presented and a benchmark is conducted.

4.6 Summary

In this chapter three different higher order finite element schemes have been compared
with respect to their suitability concerning *Lamb* wave propagation analysis. The accuracy which can be achieved deploying these approaches is much improved compared to
conventional lower order finite element methods. Almost no locking effects are to be noticed for polynomial degrees of $p_{x_3} = 3$, 4 over the thickness of the plate. Furthermore,
it can be seen that the number of degrees-of-freedom can be reduced significantly when
higher order schemes are applied.

For all studied finite element approaches the optimal polynomial degree in x_1-direction
has been found as $p_{x_1} = 3$. Nonetheless, considering all results it has to be noted that
p-elements promise the best accuracy for a low discretization in x_3-direction ($p_{x_3} \leq 4$).
Spectral and isogeometric elements reach an equal quality of the results for $p_{x_3} \geq 5$. Isogeometric elements offer the highest convergence rates and reach an acceptable accuracy
of less than one percent earlier than the compared methods.

When scrutinizing isogeometric finite elements the order of continuity is another variable
which has also an influence on the accuracy of the solution. The study shows that a
higher order of inter-element-continuity influences the convergence rate in a positive way.
Therefore, it is recommended to use the highest possible inter-element-continuity. So far,
if we neglect the computational time and study the obtained results isogeometric elements
would have to be recommended due to their high convergence rates and therefore the low
need of memory.

For the three-dimensional example the proposed guideline has been applied to a more
complex geometry and it has been found that the results are in good agreement with an
ABAQUS reference solution, computed on a very fine grid.

5 Application of the NURBS finite elements to SHM problems

5.1 Introduction

In the previous two chapters (3 & 4) the derivation and validation of the isogeometric piezoelectric finite element has been in the center of attention. The findings of these chapters are now used to study SHM based problems. In this chapter the dynamic behavior of the piezoceramic actuator is investigated utilizing the developed piezomechanical finite element.

Piezoceramic transducers, acting as actuators and/or sensors, are attractive for the generation and the reception of *Lamb* waves in SHM systems. To gain a deeper insight into the source mechanisms of *Lamb* waves, the vibrations of piezoceramic actuators are initially treated for the free and bonded state. The contributions of the out-of-plane and in-plane vibrations to the generation of the A_0- and S_0-mode are experimentally recorded via laser vibrometry and impedance measurements and theoretically explained by isogeometric finite element analysis.

SHM systems using *Lamb* waves require effective means for generating and receiving *Lamb* wave modes. The use of embedded or surface attached piezoceramic elements as actuators and sensors for the generation and the reception of *Lamb* waves is an attractive way for designing smart SHM structures [18, 49, 121, 144]. For creating effective SHM systems it is necessary to understand the generation process of *Lamb* waves in detail. The multi-modal, frequency-dependent properties of *Lamb* waves [155], the complexity of the modal behavior of piezoceramic elements and the influence of the coupling conditions complicate this task. The objective of the chapter is to study these effects experimentally as well as numerically. First, the basic principles of scanning laser vibrometry are introduced. This measurement method is used for the experimental investigations. Second, the experimentally determined eigenfrequencies and eigenforms of a free-free piezoelectric disc are compared to simulations. This is directly connected to the contents of section 3.5.4 where the isogeometric finite element has been compared to other numerical tools. In the third part the influence of the resonance of the coupled piezoceramic actuator on the excited *Lamb* wave field is studied. It is found that the resonance of the actuator has a huge impact on the amplitudes of the *Lamb* wave modes [54, 64, 116]. In the last part of this chapter the effect of resonance to the excited modes are investigated experimentally as well as numerically by varying several parameters.

5.2 Laser *Doppler* vibrometry

SHM based systems will use only a low number of measurement points to observe the structure. To study *Lamb* wave specific problems, e.g. damage interaction, mode conversion, etc., it is useful to know how the complete wave field behaves within the structure. Therefore, alternative measurement methods are used to break the limitation of applied piezoceramic sensors, which are essentially a failure when one is dealing with wave propagation problems and thus interact with the traveling waves. For that reason contact less methods are widely in use to observe the *Lamb* wave field, e.g. speckle interferometry [82], ultrasonics [60] and scanning laser vibrometry [140]. Particularly, the scanning laser vibrometry has a high spatial resolution and does not need a coupling medium. Therefore, the method is used for several investigations to understand the physical properties as attenuation of the wave amplitudes or studies on damage detection, interaction, etc. [115, 122, 127, 134, 137, 140, 141, 158].
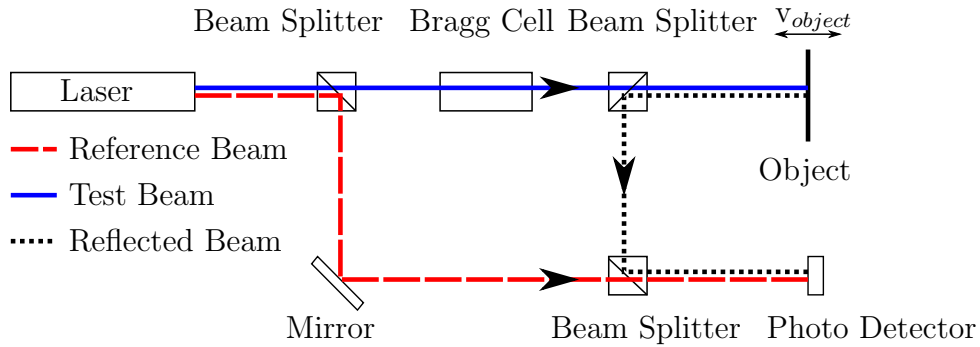

Figure 5.1: Principle of laser doppler vibrometry.

The Laser *Doppler* vibrometry is based on the *Doppler* effect [126]. The first systems for measuring small velocities[1] has been described by Yeh in 1964 [174]. If an object moves with a velocity v_{object} the frequency of the laser is shifted by the *Doppler* shift. The frequency shift Δf_D is determined by a measurement setup, shown in Figure 5.1. The laser is excited and split in two parts at the first beam splitter. One beam is used as reference and is routed to the photo detector (red beam). The second laser beam is focused on the measurement object, where it is reflected and lead to the photo detector. Both the reference and the measurement beam are superposed. Because the reference beam does not change the frequency shift of the measurement beam caused by the movement of the object creates a interferometric pattern. The pattern correlates with the objects movement. Both the movements towards the laser and away from it generate an equal interferometric pattern. Therefore, an acousto-optical modulator (bragg cell) is used to shift the original frequency by f_s. The interferometric pattern of this modulated frequency defines the non-movement of the object. If the object moves towards the laser source the modulated frequency Δf_D is reduced, vice versa. With this measurement setup it is possible to determine the velocity of the measurement point as well as its direction.

---

[1]In astrophysics the effect is in use for the measurement of high velocities (redshift)

With Equation (5.1) the velocity of the measured point can be determined

$$\Delta f_D = \frac{2 f_{laser} v_{object}}{c} = 2 \frac{v_{object}}{\lambda_{laser}} \,. \tag{5.1}$$

The parameters f_{laser}, v_{object} and c are the frequency of the He-Ne Laser, the velocity of the reflection point and the light speed.
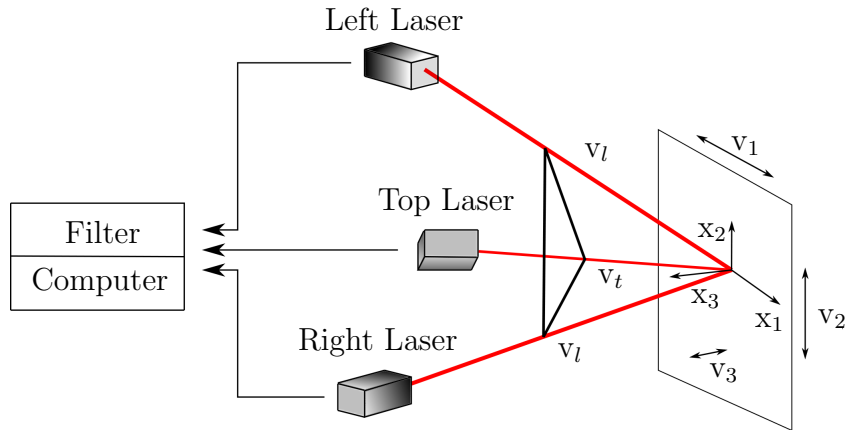

Figure 5.2: Principle of 3D laser doppler vibrometry.

The setup with a one-dimensional scanning laser vibrometer can be extended to three dimensions. Previous work in that topic has been done by Staszewski et al. [141, 142]. With three lasers which are not in the same plane (linearly independency) and some geometrical calculations the components of the velocity in x_1-, x_2- and x_3-direction are measurable. All three laser scanners work with the same principle as illustrated in Figure 5.1 and Equation (5.1). Figure 5.2 shows a sketch of the experimental setup. Three laser sources have to be placed in space with a defined position. With the known distances of all heads to the measurement object, the angle between the laser and the object can be calculated. All three laser points must be at the same position, in which the laser measures the velocity in beam direction. With the information of the beam-object angle the measured velocities v_t, v_l and v_r of each laser beam can be transformed into the velocities of defined orthogonal coordinates (v_1, v_2, v_3). For the measurements of all components of the *Lamb* waves a 3D scanning laser vibrometer (PSV-400 3D) was used.

5.3 Actuator behavior

5.3.1 Vibration of free-free piezoceramic actuator

The eigenfrequencies of a coupled piezoceramic actuator-structure system influence the effectiveness of *Lamb* wave excitation [116]. The vibration of a free-free piezoceramic discs is measured and compared with an analytical and an isogeometric finite element solution. The resonance frequency as well as the modeshape is compared. A frequency range $10\,\text{kHz} \leq f \leq 300\,\text{kHz}$ is chosen.

The eigenmodes of a general circular plate can be separated in different types. Tangential

modes, which are described by Huang et al. [63] are excluded here since they have a weak appearance. Also the thickness modes are not considered. For piezoceramic plates with thicknesses less than 2 mm considered here they occur at frequencies higher than 1 MHz [2]. These frequencies are outside the frequency domain where only the A_0- and the S_0-mode exist and higher *Lamb* modes occur. Therefore, the investigation does not take them into account. Only bending and radial modes are studied in this investigation. If the piezoceramic is applied to a structure these types of eigenmodes will primarily activate *Lamb* waves. Moreover, both mode types exist in the regarded frequency domain where only the two basic *Lamb* wave modes arise. Figure 5.3A displays the used coordinate system and the direction of the polarization of the piezoceramic discs. To measure the eigenfrequencies a linear chirp signal is generated utilizing the piezoceramic actuator. The piezoceramic disc is mounted on foam (free) and the response of the structure is measured at the bottom surface. Figure 5.3B shows an example of a free disc made of PIC-181 with the wire and the soldering points at the top surface and a diameter $d = 10$ mm and a thickness $h = 0.5$ mm.
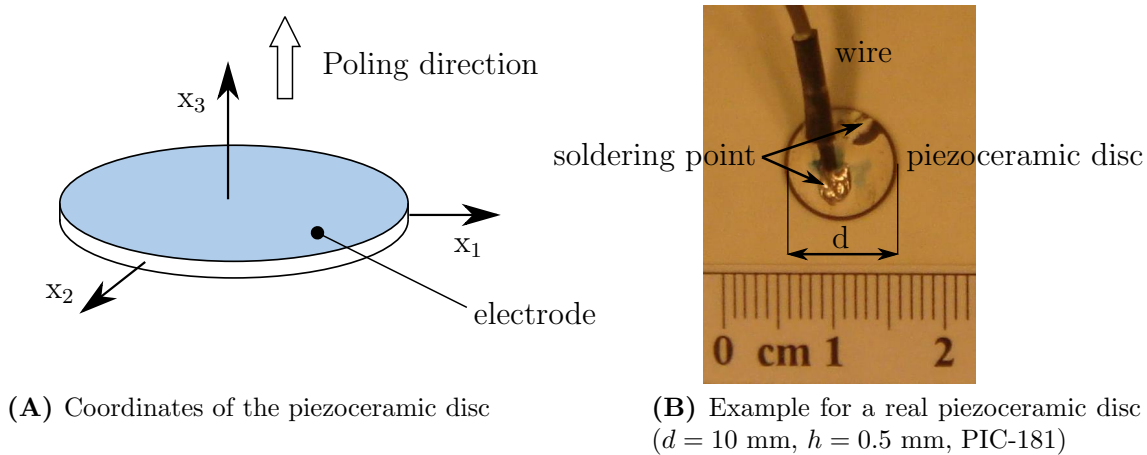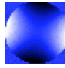

(A) Coordinates of the piezoceramic disc

(B) Example for a real piezoceramic disc ($d = 10$ mm, $h = 0.5$ mm, PIC-181)
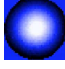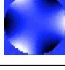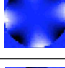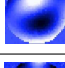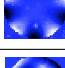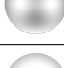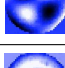
Figure 5.3: Uncoupled piezoceramic disc.

5.3.2 Bending modes of the piezoelectric circular plate

Seven piezoceramic discs are studied with different material properties as well as different geometries. The material properties of PIC-151 and PIC-181 are given in Table A-5. The out-of-plane component of the velocity of the bottom surface of each disc is measured after applying the external broadband signal. Therefore, no wire or soldering point disturb the laser beam. Table 5.1 shows seven measured bending modes compared with a isogeometric finite element solutions. The dominant displacements are in x_3-direction. It must be noted that the wire and soldering points which are illustrated in Figure 5.3B have only a low influence on the eigendynamic of the discs [168]. Therefore, they are not included in the numerical model. Nevertheless, the results in Table 5.1 show a good agreement (error is smaller than 10 % with respect to the numerical solution with exception of one result) between the simulations (S.) and the measurements (M.). The sequence of the mode appearance as well as the mode shapes are similar.

Table 5.1: Comparison of measurement (M.) of free piezoceramics with the isogeometric solution (S.) (1 - PIC-151, $d = 10\,\text{mm}$, $h = 1\,\text{mm}$; 2 - PIC-181, $d = 10\,\text{mm}$, $h = 0.5\,\text{mm}$; 3 - PIC-181, $d = 10\,\text{mm}$, $h = 2\,\text{mm}$; 5 - PIC-181, $d = 16\,\text{mm}$, $h = 1\,\text{mm}$; 6 - PIC-181, $d = 16\,\text{mm}$, $h = 2\,\text{mm}$; 7 - PIC-151, $d = 40\,\text{mm}$, $h = 0.5\,\text{mm}$)

	S.	M.	1 [kHz]	2 [kHz]	3 [kHz]	4 [kHz]	5 [kHz]	6 [kHz]	7 [kHz]
M.			28.9	17.7	38.8	59.7	12.9	23.4	-
S.			27.3	16.7	32.4	58.6	12.97	24.7	0.8
M.			58.1	33.2	63.1	109.5	24.3	48.1	1.9
S.			53	32.2	61.4	106.1	24.9	46.4	1.77
M.			63.5	40.1	74.4	123.3	29	55.3	2.05
S.			60.9	38.6	72.1	120.7	29.7	54.1	2.1
M.			106.8	68.1	124	192.1	49.4	90.4	3.7
S.			101.8	66.9	120.6	187.9	51.1	88.6	3.7
M.			117.5	72.5	132.2	199.6	53.2	95.8	4.15
S.			107.3	69.6	125.2	191.3	53.4	91.4	3.9
M.			156.6	103.5	179.7	263.5	74.6	129.8	5.5
S.			147.8	101	175	257.3	76.4	126.1	5.7
M.			192.1	119.6	205.5	295.8	86.5	149	6.9
S.			168.2	115.2	197	276	86.9	140.7	6.6
M.			204.5	128.7	222	-	95.2	161.3	7.6
S.			192.9	126.8	215	301.8	95.5	153.7	7.3

5.3.3 Radial modes of the piezoelectric circular plate

For the comparison of the radial modes with the experimental and the isogeometric results an analytical solution has been used. The radial eigenfrequencies f_j correspond to eigenvalues of the characteristic equation of the analytical solutions. The eigenvalues are only dependent of the *Poisson*s ratio of the x_1-x_2-plane ν_{12}. For a *Poison*s ratio of $\nu_{12} = 0.34$ the first four eigenvalues z_j are given by Giurgiutiu [49] as

$$z_1 = 2.074; \quad z_2 = 5.397; \quad z_3 = 8.576; \quad z_4 = 11.73\,.$$

With the values of z_j the eigenfrequencies f_j can be directly calculated as

$$f_j = \sqrt{\frac{1}{S_{11}^E \rho (1 - \nu_{12}^2)}} \frac{z_j}{\pi d_{max}}\,. \tag{5.2}$$

The experimental identification of the radial modes has been done using 3D scanning laser vibrometry measurements. An example is shown in Figure 5.4. All three spectra and the corresponding in-plane mode shape are plotted. The graphs show that the in-plane modes also produce remarkably high secondary out-of-plane components. It has been observed that even in out-of-plane spectra measured with a 1D vibrometer radial mode peaks are to bee observed (see Figure 5.4C). In those cases it is not possible to correlate a fundamental bending mode shape shown in Table 5.1 (and higher ones too) to the measured peaks. The isogeometric simulations show that many bending modes coexist around the higher

resonance frequencies of the first radial mode. This is also validated by the experimental results. A splitting of the mode types by 1D (out-of-plane) measurements is not possible. If the in-plane components are observed, the mode shape of an in-plane mode can be seen (see Figure 5.4D).

(A) u_1-displacement

(B) u_2-displacement

(C) u_3-displacement

(D) Measured mode shape $u_{mag} = \sqrt{u_1^2 + u_2^2}$; $f = 222$ kHz
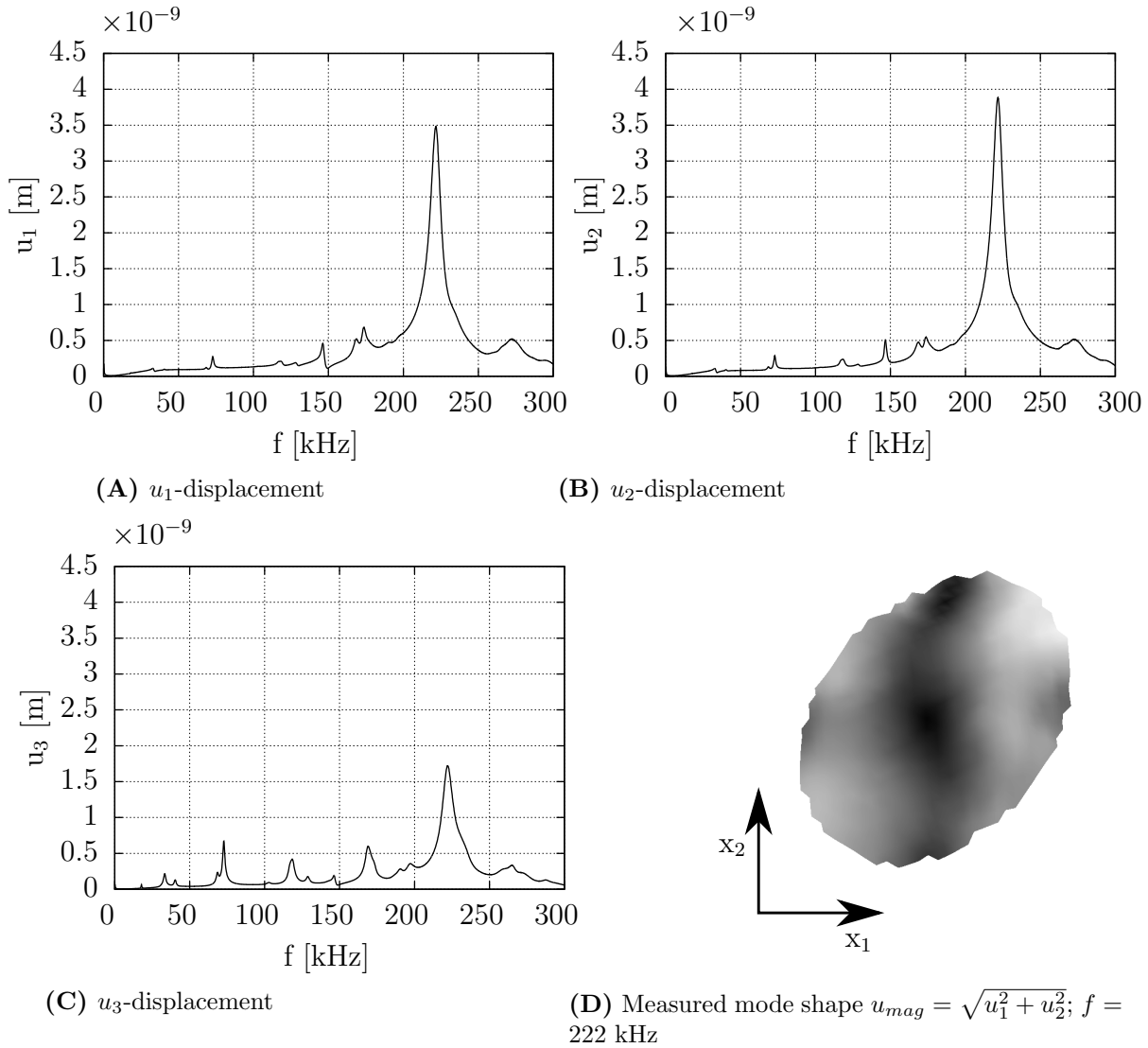
Figure 5.4: 3D measurement of a piezoceramic ($d = 10$ mm, $h = 0.5$ mm, PIC-181).

Because, knowing the in-plane spectra are sometimes not enough to identify the radial eigenfrequencies without a doubt, additional measurements were done. Following Huang et al. [63] only in-plane and thickness modes cause resonance peaks in the spectrum of electrical impedance. To additionally validate the resonance values, the impedance has been measured with a network analyser Advantest R3751 A [116]. Table 5.2 illustrates the comparison between the calculated frequencies of the first radial mode with the 3D-measured ones and values obtained with impedance measurements. The 3D laser measurements do not observe all existent radial eigenfrequencies. However, the analytical as well as the isogeometric solution determine all first radial modes correctly. Moreover, as Equation (5.2) states, a change of the height of the piezoceramic disc has no influence on the resonance frequencies. Both, the experiments and the isogeometric result show such behavior.

Table 5.2: Comparison of the experimental data (3D vibrometry and impedance measurements) with the analytic solution of the radial eigenfrequencies.

Diameter [mm]	Material	Height [mm]	Analytical [kHz]	Numerical [kHz]	3D vibrometer [kHz]	Impedance [kHz]
10	PIC-151	1	190.77	192.9	195	195
40	PIC-151	0.5	47.693	48.4	-	49
10	PIC-181	0.5	228.32	233.7	222	225
10	PIC-181	1	228.32	233	225	224
10	PIC-181	2	228.32	230.3	224	223

5.3.4 Vibration of the coupled piezoceramic actuator

The design of a piezoceramic patch actuator for structural health monitoring applications should guarantee a most effective *Lamb* wave generation. According to Kessler, Su, et al. [72, 144, 159] the most effective generation of *Lamb* waves is accomplished, if the actuator length or diameter d, respectively, is related to the wave length in the following manner

$$d = \lambda(n + 0.5) \, . \tag{5.3}$$

λ describes the wavelength of the regarded *Lamb* wave mode and n is an arbitrary integer ($n = 0, 1, 2, \ldots$). To investigate the resonance effects a CFRP plate with a $[(0/90)_f / + 45 / - 45 / \overline{(0/90)}_f]_S$ layup and a plate thickness of $2\,\mathrm{mm}$ is examined. Table 5.3 shows the first four optimal wavelengths for this CFRP plate. The values are determined using Equation (5.3) in combination with the measured dispersion curves to get the frequencies which are corresponded to the wavelengths λ [116]. The experimental investigation has been done between 0 and 500 kHz. Only one optimal excitation frequency of the S_0-mode and three for the A_0-mode are within the considered frequency range.

Table 5.3: Optimal frequencies for *Lamb* mode generation in a CFRP plate up to $500\,\mathrm{kHz}$ in 0°-direction.

n	λ [m]	f of A_0 [kHz]	f of S_0 [kHz]
0	0.0200	40.7	276
1	0.0067	186	> 500
2	0.0040	335	> 500
3	0.0029	480	> 500

Circular shaped piezoceramic actuators with three different heights (0.5 mm, 1 mm, 2 mm) and a diameter $d = 10$ mm are glued on the CFRP plate. A linear swept-frequency cosine signal is used to excite *Lamb* waves with multiple frequencies. Two measurements are performed for each piezoceramic. First the surface of the ceramic is scanned to gain the frequency response of the ceramic. The second measurement measures the CFRP plate. The measurement has been done avoiding reflections from the edges. By taking the wave numbers of the A_0- and S_0- mode it is possible to plot the frequency response spectra of each mode. Therefore, a 3D FFT is performed on the data of the measured C-scan of the laser vibrometer to detect the temporal periodicities (frequencies) and the spatial

periodicities (wave numbers) of the propagating signals [5, 28]. In doing so the separated frequency amplitude curve can be determined.

If Equation (5.3) holds the A_0-mode experiences a first maximum at 40.7 kHz and the S_0-mode at 276 kHz. The experimental results are displayed in Figures 5.5A - 5.5C. The noise in the S_0-mode spectra are caused by the great wavelength and the small displacement in x_3-direction. The different curves from Figure 5.5 show a close relation between the resonances of the piezoelectric actuators and the spectra of the *Lamb* wave modes. The frequencies corresponding to certain values of *Lamb* wave wavelength for the CFRP plate have been derived from Equation (5.3) and are given in Table 5.3 for frequencies up to 500 kHz both for the S_0- and A_0-mode. Comparing the measured resonance frequencies (Figure 5.5) with the calculated data from Table 5.3 it can be concluded that Equation (5.3) cannot be applied for thicker piezoceramic actuators. For example for a frequency of $f = 335$ kHz a optimal excitation for the A_0-mode should occur. Only the type 1 piezoceramic shows a maximum.
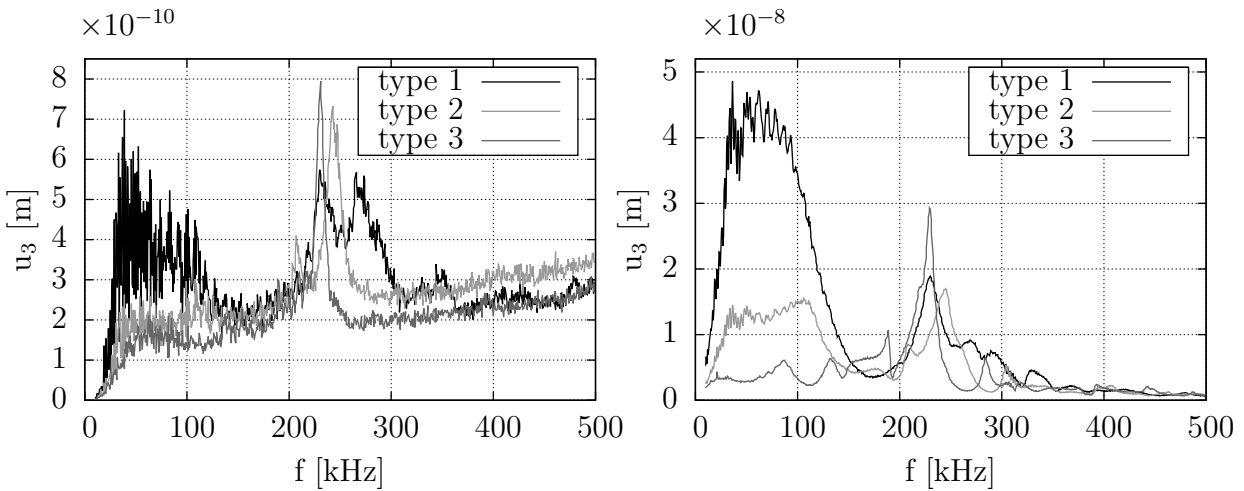
(A) S_0-mode spectra

(B) A_0-mode spectra
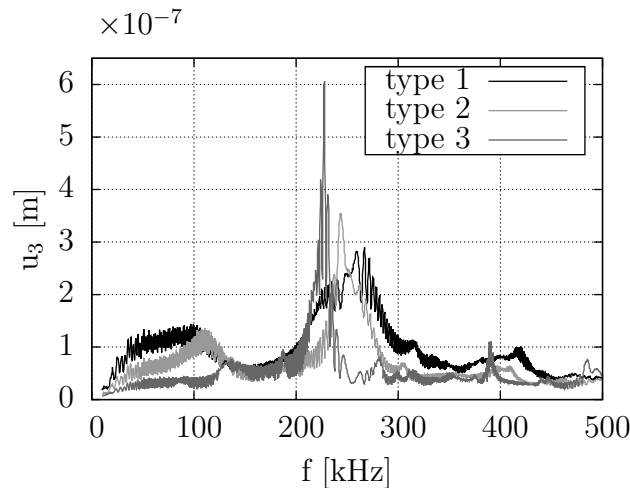
(C) Spectra of piezoceramic discs

Figure 5.5: Spectra for the *Lamb* wave modes for a CFRP plate and different piezocermic discs - Type 1 ($d = 10$ mm, $h = 0.5$ mm), Type 2 ($d = 10$ mm, $h = 1$ mm) and Type 3 ($d = 10$ mm, $h = 2$ mm).

It is evident that the eigenfrequencies of the actuator in connection with the structure have a major impact on the excited *Lamb* wave amplitudes. The assumption that an optimal excitation of *Lamb* modes occurs if the diameter of the piezoceramic disk is one half of an integer number of the wavelengths does not hold under any circumstance [116]. Only for thin ceramics it can be confirmed that the lowest eigenfrequency calculated with Equation (5.3) coincides with the measurements. In all other cases no agreement with measurements could be observed, meaning that the application of Equation (5.3) to estimate optimal excitation frequencies cannot be recommended.

For SHM systems the application of higher frequencies are preferable due to an improved resolution and a better ability to detect damages. The resonances play a major role in the excitation of *Lamb* waves. For thicker piezoceramics it is the dominant effect which influences the amplitudes of the excited *Lamb* waves [54, 97]. This effect can be used to reduce the input energy of the actuators. The adhesive layer as mentioned before shifts the position of the resonances. Therefore, a tuning of the optimal frequency should be applied to receive an optimal excitation.

5.3.5 Influence parameters to the *Lamb* wave excitation

The experiments of the previous section have shown that the resonances of the coupled piezoceramic actuator have a dominant influence on the excited *Lamb* waves. In this section the parameters which influence the resonance of the actuator-adhesive layer-host structure system are studied. To investigate the parameters a two-dimensional isogeometric finite element model is created (see Figure 5.6). Therefore, computationally very costly three-dimensional simulations can be avoided [162]. Moreover, the findings presented in chapter 4 are used and the optimal discretization scheme is applied ($p_{x_1} = 3$, $p_{x_2} = 4$, $\chi_{A_0} > 4$) to reduce the numerical effort and to gain a good accuracy.
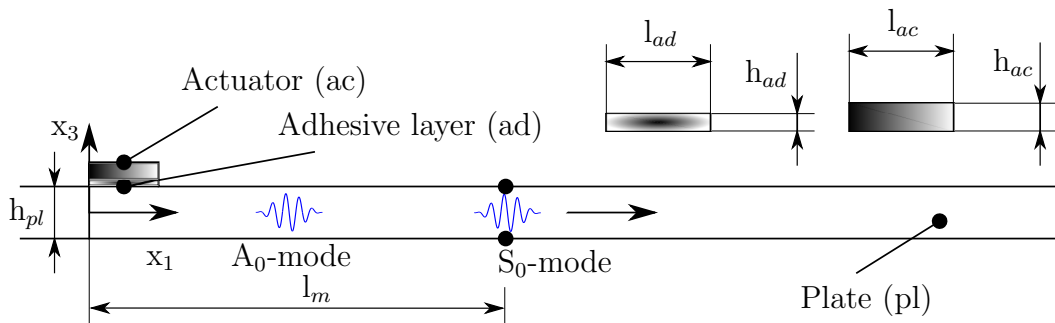
Figure 5.6: Two-dimensional symmetric model, used to investigate the influence of the bonding layer to the *Lamb* wave excitation (actuator: PIC-181; adhesive layer: paraffin wax; plate: aluminium, $l_{pl} = 0.6$ m, $h_{pl} = 2$ mm); the results are being measured at a point located at a distance of $l_m = 50$ mm from the actuator.

Several parameters are varied to study their influence on the resonance of the actuator and the A_0- and S_0-mode spectra. The parameter are:
- the thickness of the adhesive layer,
- the *Young*s modulus of the adhesive layer,

- the thickness of the actuator,
- the length of the actuator and
- the *Young*s modulus of the plate.

The geometry of the plate remains the same for all simulations. The non-varied properties of the model are given in Table 5.4. In all given models the rest of the parameters are chosen as in the Table 5.4. At the left side of the model (cf. Figure 5.6) symmetric

Table 5.4: Properties of the model in Figure 5.6.

Parameter	Length [mm]	Height [mm]	Material [kHz]
pl	600	2	aluminum (Table A-1)
ac	5	1	PIC-181 (Table A-5)
ad	5	0.05	paraffin wax (Table A-6)

boundary conditions ($u_1(x_1 = 0, x_2) = 0$) are applied to reduce the numerical effort. The actuator is made of the piezoelectric material PIC-181 (see Table A-5), the plate consists of aluminum (see Table A-1) and the adhesive layer is made of paraffin wax (see Table A-6). The model is defined by the plate thickness h_{pl}, the plate length l_{pl}, the actuator thickness h_{ac}, the actuator length l_{ac}, the adhesive layer thickness h_{ad} and the adhesive layer length l_{ad}.

At the top surface of the piezoceramic actuator a constant electrical potential is applied. At the bottom surface of the actuator the electrical potential is set to zero. A broad-band excitation signal (linear chirp)

$$\phi\left(t\right) = \hat{\phi}\sin\left[2\pi\left(f_0 + \frac{f_1 - f_0}{t_1}t\right)t\right] \tag{5.4}$$

is used. The start frequency f_0 and end frequency f_1 are chosen as $f_0 = 10$ kHz and $f_1 = 500$ kHz. The time is given as $t_1 = 1/f_0$. The displacements of the top surface of the piezoceramic actuator and the displacements of a top ($x_3 = +h_{pl}/2$) and a bottom ($x_3 = -h_{pl}/2$) node of the plate in a distance $l_m = 50$ mm are calculated. The displacements of the top surface of the piezoceramic are used to determine the spectrum of the applied actuator. The displacements of the top and bottom node of the plate are used to separate the two *Lamb* modes from each other without performing a 2D FFT. In the end after applying a FFT to the time-dependent data, three spectra are gained similar to Figure 5.5. Figures 5.7A-5.7C show the simulated u_3-displacement spectra of the two-dimensional model of the two basic *Lamb* wave modes and the piezoceramic actuator. The model is defined as illustrated in Figure 5.6 and Table 5.4 without varied parameter. As illustrated in the experimental investigation in the previous section there is a dominant coupling between the actuator eigendynamic and the excited *Lamb* waves. As in the experiments the A_0-mode is strongly influenced by the low frequency peaks in the piezoceramic spectrum. This is an indicator for the existence of bending modes in this frequency domain. As shown in the previous section these eigenmodes have a greater influence on the A_0-mode than on the S_0 one. On the other side, the first radial eigenmode at $f = 237$ kHz has a strong impact to the symmetric S_0-mode which leads to a high peak in the spectrum on the symmetric mode.

In summary, it can be said that the general properties of the coupled actuator-structure

system in comparison of the numerical and experimental results can be described by a simple two-dimensional model.
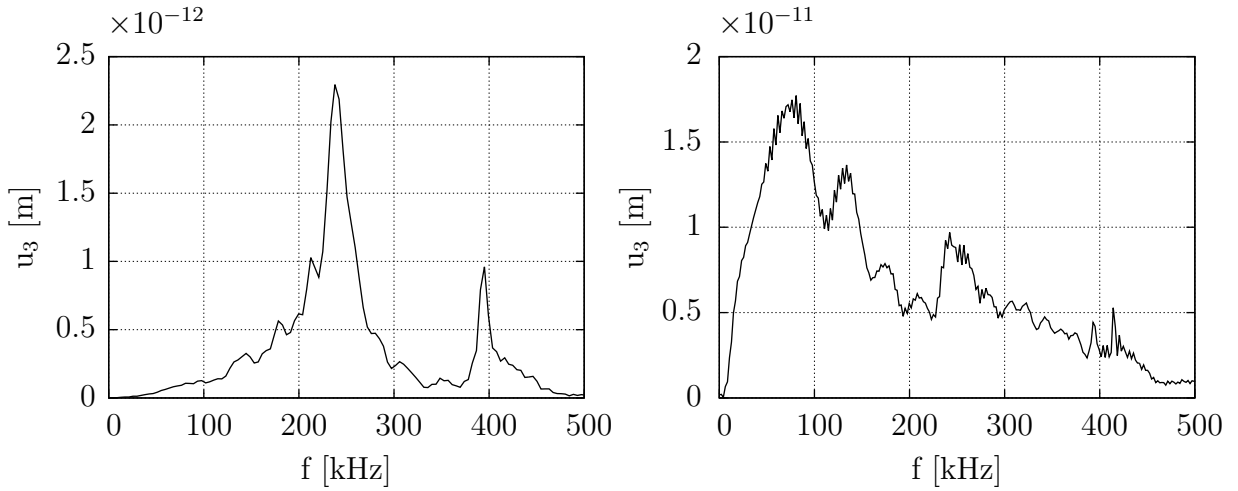
(A) S_0-mode spectrum at a distance l_m

(B) A_0-mode spectrum at a distance l_m
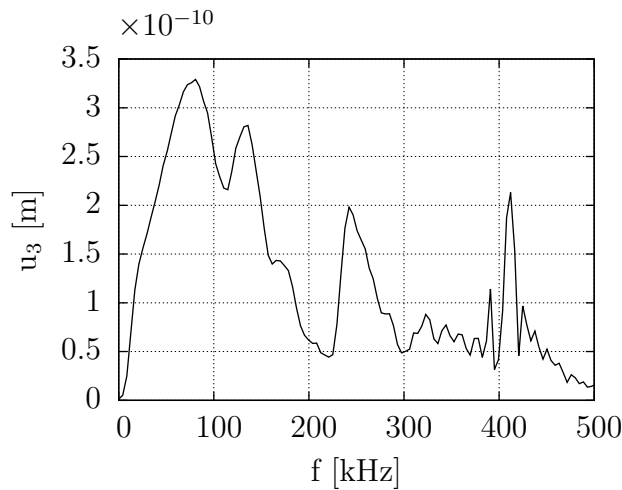
(C) Spectrum of the piezoceramic

Figure 5.7: Spectra of u_3-displacement of the two-dimensional model without parameter variation.

Influence of the adhesive layer

The impact of the adhesive layer to the coupling between an actuator and a structure is well known for thin piezoceramic patches. If a patch actuator is glued to the surface of a structure the so called "shear lag" effect can be observed. The "shear lag" is caused by an adhesive layer of finite thickness between the actuator and the host structure (see Figure 5.8). The excitation signal from the actuator is transmitted to the structure through interfacial shear stresses within the bonding layer for the most part [49, 138]. The "shear lag" causes a reduction of shear strain transfer between the PZT actuator and the host structure. With a lower shear modulus and a thicker adhesive layer, the "shear lag" effect becomes more pronounced. As a result, the signal amplitude is reduced significantly if

the resonance effects play a minor role [53]. Due to this effect the effective length of a piezoelectric actuator is smaller than the actual length. Consequently, it can be assumed, that only a fraction of the actual surface of a piezoelectric actuator contributes to the strain transfer [22]. Thus, correction factors have to be applied in order to account for the "shear lag" effect. Based on analytical models (e.g. *Euler-Bernoulli* beam theory) correction factors for various problems assuming the application of thin piezoceramics ($\approx 0.2\,mm$) only have been derived in [22, 35, 49, 136].
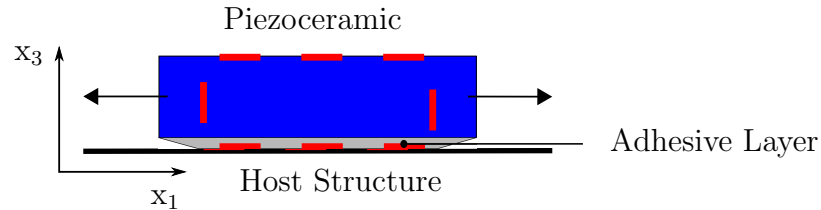

**Figure 5.8:** Schematic representation of the "shear lag" effect

For thicker piezoceramics the resonances of the coupled actuator-structure system play a more important role and superimpose the "shear lag" effect. Moreover, the assumptions made by the *Euler-Bernoulli* beam theory are not fulfilled in the case of thick ceramics and the correction factors can be overestimated. Therefore, two parameters of the adhesive layer are varied to study their influence to the first resonance of the S_0-mode.

The A_0-mode spectrum has no clear first resonance peak caused by the first radial mode of the piezoceramic. This mode is influenced by the bending modes as well as the radial modes. Because, both modes are affected differently by a parameter variation the analysis has been shown that the equal resonance peak of the A_0-mode is harder to find for the variations compared to the S_0-mode spectra. Therefore, the movement of the resonance peak in the A_0-mode spectrum caused by the radial mode is hard to determine and no analysis of this spectrum has been done. However, the changes in the S_0-mode spectrum are caused by the behavior of the piezoceramic actuator. The results gained by the analysis of the S_0-mode spectrum should be applicable to the behavior of the A_0-mode spectrum.

Adhesive layer thickness: The adhesive layer thickness h_{ad} is varied between $10\,\mu m \ldots 150\,\mu m$. The change in the first resonance frequency as well as the amplitude of this excitation frequency are observed for the S_0-mode. Figure 5.9A shows the frequency of the first peak in the S_0-mode spectrum as a function of the adhesive layer height. The frequency decreases for a greater adhesive layer thickness. As illustrated before, for the experimental model in Figure 5.5 and the numerical model in Figure 5.7, there is a connection between the dynamic behavior of the piezoceramic actuator and the spectra of the two *Lamb* wave modes. Because the coupled actuator-structure system becomes softer the resonance frequencies of the actuator shift to a lower frequencies.

The amplitude of the resonance peak increases (see Figure 5.9B). This disagrees with the "shear lag" effect, which states that higher thicknesses lead to a reduction in the amplitudes of the excited *Lamb* wave modes. The amplitude curve is not steady because near the first radial eigenfrequency other peaks occur. The radial mode is superposed by bending modes. Both mode types are influenced differently by the adhesive layer height and depending on how similar the resonance frequencies of both mode types are, the amplitudes

increase or decrease. However, only great changes (20 μm or more) in the adhesive layer thickness lead to a noticeable change in frequency and amplitude. Therefore, the adhesive layer thickness could be used in the design process to alter the eigenfrequencies of the piezoceramic actuator. Small variations caused by the production process are negligible from the original design.
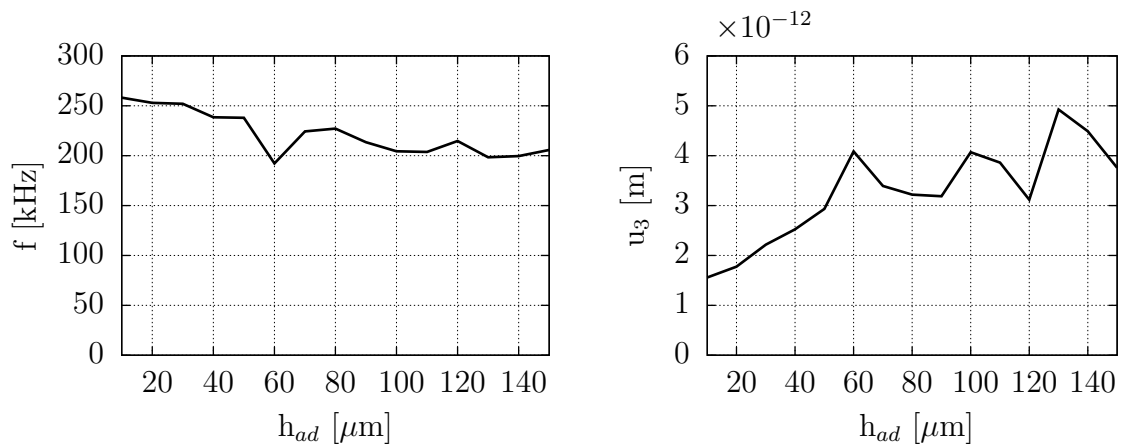
(A) Frequency of the first resonance peak

(B) Amplitude of the first resonance peak

Figure 5.9: Influence of the thickness h_{ad} of the adhesive layer to the frequency and to the amplitude of the S_0-mode.

Adhesive layer stiffness: The adhesive layers *Young*s modulus Y_{ad} is varied between $0.5 \cdot 10^9 \, \text{N/m}^2 \ldots 3300 \cdot 10^9 \, \text{N/m}^2$. The lower bound correlates to 50% of the *Young*s modulus of paraffin and the upper bound of the *Young*s modulus correlates to epoxy, which is typically used to glue piezoceramics irreversible to structures.

(A) Frequency of the first resonance peak

(B) Amplitude of the first resonance peak

Figure 5.10: Influence of the *Young*s modulus Y_{ad} of the adhesive layer to the amplitude of the S_0-mode.

The influence of the stiffness change in the adhesive layer to the frequency of the first peak in the S_0-mode spectrum is illustrated in Figure 5.10A. For higher *Young*s moduli the first resonance peak shift to higher frequencies. The results show that the *Young*s modulus of different adhesive layers (epoxy or paraffin) does not change the frequency of the first peak drastically.

Figure 5.10B shows the amplitude of the first peak in the S_0-mode spectrum as a function of the *Young*s modulus of the adhesive layer. Higher *Young*s moduli cause a reduction in amplitude. This behavior disagrees with the "shear lag" effect and underline that for thicker piezoceramics the eigendynamic superimposes the "shear lag" effect [54, 162]. Variations of the material properties of the adhesive layer do not seem to influence the first resonance frequency drastically. Therefore, changes in the material properties due to temperature variations and/or variations caused by a variance in the production process are negligible in the design process.

In summary one can say that the "shear lag" correction factor based on the assumption of the *Euler-Bernoulli* beam theory does not work correctly in resonance regions of the actuator to predict the amplitude losses caused by adhesive layer changes. Therefore, more detailed analyses are needed.

Influence of the actuator geometry

After studying the influence of the adhesive layer on the *Lamb* wave excitation the impact of the actuator geometry is observed. Firstly, the length is studied and secondly the thickness of the actuator.

Actuator length: The piezoceramic actuator length l_{ac} is varied between 2 mm...16 mm. The influence of this variation on the first resonance frequency is illustrated in Figure 5.11A. There is approximately a $1/d$ correlation (analytical) between the length of the actuator and the first peak in the S_0-mode spectrum caused by the first radial eigenfrequency of the piezoceramic actuator. This coincides with the behavior of the radial eigenfrequencies of the a free circular disc in Equation (5.2).
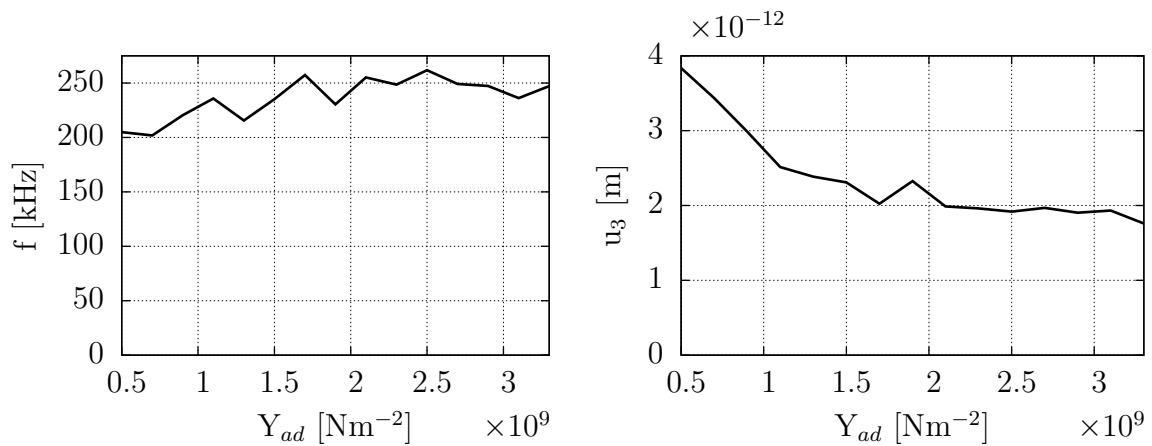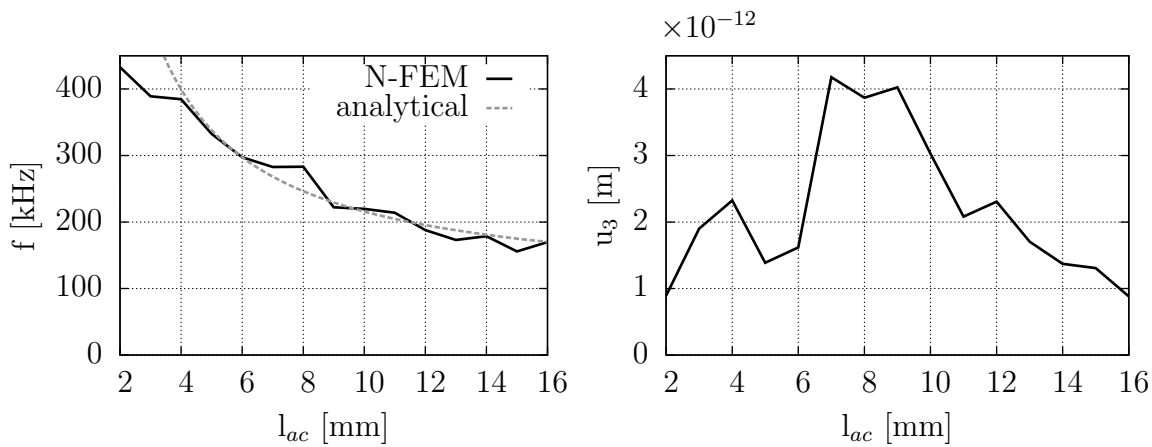

(A) Frequency of the first resonance peak   **(B)** Amplitude of the first resonance peak

Figure 5.11: Influence of the thickness l_{ac} of the adhesive layer to the amplitude of the S_0-mode.

The value of the u_3-displacement illustrated in Figure 5.11B first increases and for lengths $l_{ac} > 9$ mm decreases. This behavior could be explained as a result of superposition of the first radial and a bending mode. Both modes are differently influenced by extending the length of the actuator; $1/d$ for the radial mode and $1/d^2$ for the bending modes [116]. For lengths between 7 mm and 10 mm the frequency of a lower order bending mode correlates with the first radial mode. The optimal diameter calculated with Equation 5.3 optimal diameter for the actuator does not agree with the results.

That is to say, the changes in the actuator length strongly influence the dynamic behavior. But also here small changes due to the production process can be neglected.

Actuator thickness: The piezoceramic actuator thickness h_{ac} is varied between 0.1 mm $\ldots 3$ mm. In Figure 5.12A the frequency as a function of the actuator thickness is plotted. Changes in the thickness has a low influence the resonance frequency (compared to a change of the length) of the radial eigenmode as Equation (5.2) stated for the free elastic disc, except the strong decrease between 0.2 mm and 0.6 mm. Experimental and numerical investigations of the free piezoceramic disc show that the eigenfrequencies for thicker piezoceramics are higher. In this research the frequency of the first peak of the S_0-mode spectrum is considered. If a bending mode moves near a radial mode, both modes superpose each other and lead to higher amplitudes. The first peak is shifted to lower frequency regions.
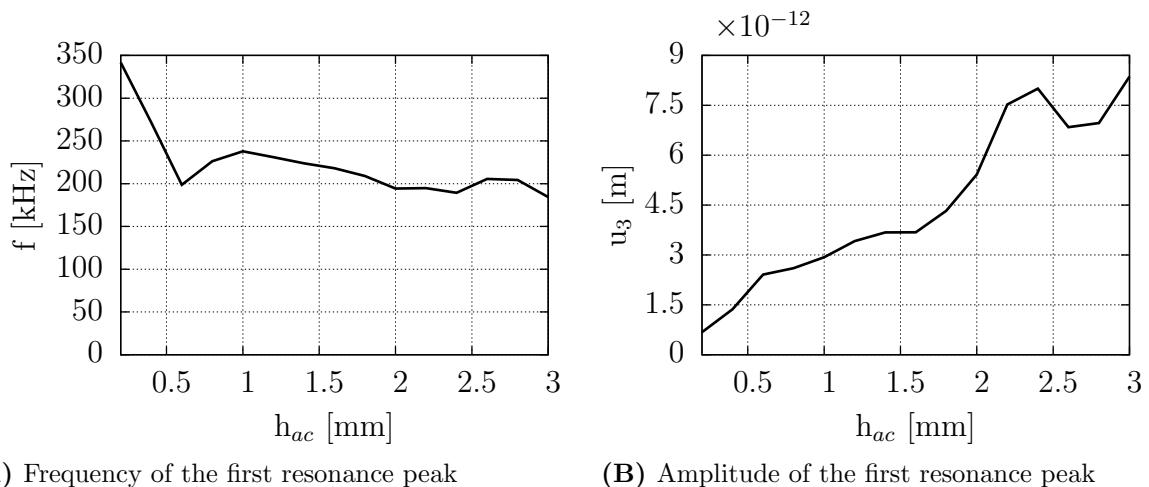
(A) Frequency of the first resonance peak   **(B)** Amplitude of the first resonance peak

Figure 5.12: Influence of the thickness h_{ac} of the actuator to the amplitude of the S_0-mode.

The amplitudes of the peaks in the S_0-mode spectrum are plotted in Figure 5.12B. For thicker piezoceramics the amplitudes increase. The S_0-mode is dominantly excited by shear stresses. Therefore, a higher bending stiffness due to the greater actuator thickness leads to a better shear stress transfer into the structure. Moreover, the bending modes are influenced by the greater bending stiffness. The frequency of the lower order bending modes shift to higher frequencies. The superposed resonances lead then to higher amplitudes as one can see in Figure 5.12B.

Influence of the plate stiffness

In this section the influence of the plate stiffness is investigated. The *Young*s modulus of the plate Y_{pl} is varied between $5 \cdot 10^9 \ldots 2.1 \cdot 10^{11}$ N/m^2. The density is constant and chosen as $\rho_{alu} = 2700$ kg/m^3. Figure 5.13A shows the frequency of the first peak of the S_0-mode spectrum as a function of the variation of the *Young*s modulus. The frequency changes between 200 kHz and 244 kHz without any noticeable connection to the change of the plates *Young*s modulus. The amplitudes behavior of the first peak of the S_0-mode is plotted in Figure 5.13B. For very low a *Young*s modulus the amplitude is high. In that case the resistance to a deformation of the plate is lower and thus higher amplitudes are possible. In contrast to the frequency behavior in Figure 5.13A there is a coupling between the amplitude reduction and the plate stiffness, except for a small variation between $Y_{pl} = 2 \ldots 2.5 \cdot 10^{11}$ N/m^2.

(A) Frequency of the first resonance peak   **(B)** Amplitude of the first resonance peak
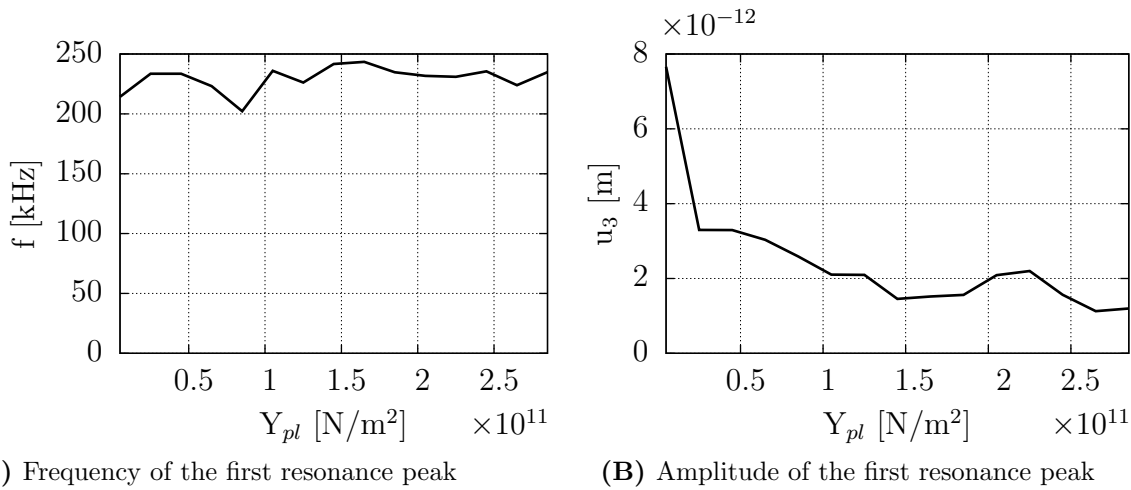
Figure 5.13: Influence of the *Young*s modulus Y_{pl} of the plate to the amplitude of the S_0-mode.

5.4 *Lamb* wave in composites (continuous mode conversion)

Lamb waves occur in minimal two modes and they, as shown in Figure 4.11, can convert into each other under special conditions. Typically that happens at discrete discontinuities which are non-symmetric with respect to the plates center plane [4, 169]. Figure 5.14 shows an example of mode conversion in a CFRP plate. The anti-symmetric A_0-mode (short wavelength) and the symmetric S_0-mode (long wavelength) are excited by a piezo-ceramic source at the right edge of the figure. The S_0-mode travels through a flat bottom hole and a new converted A_0-mode occurs. The original A_0-mode has not reached the discontinuity at the point of time displayed in Figure 5.14. A part of the energy of the S_0-mode is transferred to a A_0-mode [4]. It must be noted that the modes can only transform into other modes which exist at the specific frequency in the dispersion curves [24].

In addition to the well known mode conversion at discontinuities in experimental investigations of *Lamb* wave propagation in a CFRP plate a continuous mode conversion (CMC) phenomenon has been discovered [75, 100, 166, 167]. In this chapter the effect of CMC is

presented. Experimental investigations are shown and B-scans which are one way to identify the converted modes are illustrated. Moreover, it is tried to give an explanation for the appearance deploying a numerical analysis using the developed isogeometric finite element.
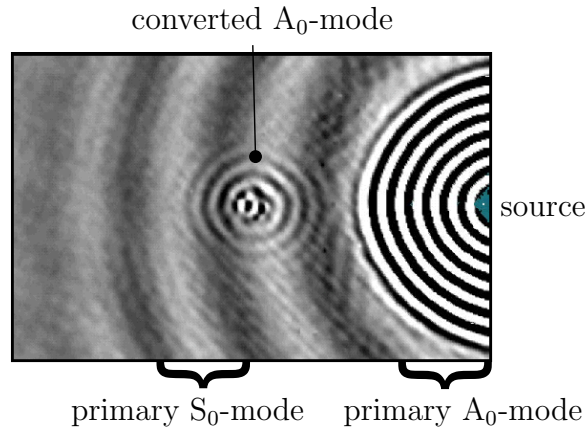
Figure 5.14: Example of mode conversion of a 5 cycle sinus burst for $f = 100$ kHz at a flat bottom hole ($d = 10$ mm, $h = 1$ mm) in a CFRP plate (1 m×1 m×2.02 mm) measured by a scanning laser vibrometer in a scanning surface (0.24 m×0.155 m).

The chapter is structured as follows. The experimental setup is shown, the effect of CMC is illustrated and its properties are explained. The identification of the conversion and the modes is done using B-scans. After the description of the effect, an experimental and numerical analysis is done to find an explanation for CMC. To perform the numerical analysis two isogeometric finite element models are utilized with different levels of detail. The results are discussed and conclusions are drawn.

5.4.1 Experimental setup

The experimental investigations are performed with help of a 1D (PSV 300) as well as 3D (PSV 400 3D) scanning laser vibrometer from Polytec. As commented in section 5.2 laser scanning vibrometry is widely used for the experimental investigation of *Lamb* waves. Also in this chapter the scanning laser vibrometry is used to obtain the experimental data.
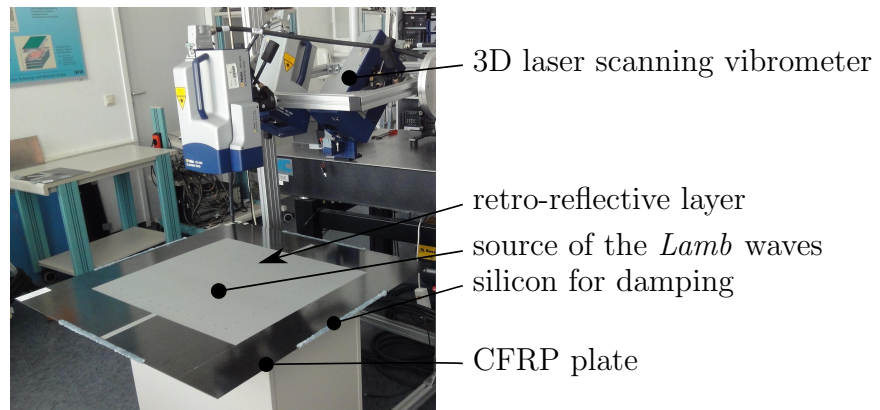
Figure 5.15: Experimental setup.

Figure 5.15 displays the experimental setup. The 3D laser scanning vibrometer scans the top surface of a CFRP plate (1 m×1 m×2.02 mm), which is positioned on foam. The stacking sequence of the investigated CFRP plate is given in Table 5.5. The top and the bottom surface are made of a twill fabric (see Figure 5.21A) and the center layer is made of a plain fabric (see Figure 5.21B). The average distances between the lasers and the plate are between 0.62 m and 0.94 m.

Table 5.5: Layer setup of the CFRP plate (1 m×1 m×2.02 mm) [131].

| layer	orientation [°]	type	layer thickness [mm]
1	0/90	twill fabric	0.4
2	+45	UD layer	0.25
3	-45	UD layer	0.25
4	0/90	plain fabric	0.22
5	-45	UD layer	0.25
6	+45	UD layer	0.25
7	0/90	twill fabric	0.4

The *Lamb* waves are excited using a piezoceramic actuator of 20 mm diameter and a thickness of $h = 1$ mm made from the material Marco FPM202[2]. To allow a reversible coupling between actuator and plate the piezoceramic source is attached with paraffin at the center of the bottom surface. The edges are damped by silicon to reduce the amplitude of reflected waves. The top surface is coated by a retro-reflective layer to enhance the signal-to-noise-ratio of the measurement signals. As excitation signal a 5 cycle sinus burst amplified by a NF-HSA-4011-amplifier is fed to the actuator. During the measurement the sinus burst is repeated for each measurement point and as results one gets a C-scan similar to Figure 5.14 for a frequency $f = 100$ kHz.

5.4.2 The description of the phenomenon

Figure 5.16 shows the out-of-plane velocity field of an undamaged CFRP plate for an excitation frequency of $f = 200$ kHz. The actuator is applied at the center at the bottom surface of the plate. The x_1-axis of the global coordinate system corresponds to the zero degree orientation of the CFRP plate. Two primary modes are excited by the piezoceramic source, the fast S_0-mode (long wavelength) and the slower A_0-mode (short wavelength). Due to their different velocities the two modes are clearly separated as shown in Figure 5.16. The term primary means that both modes are excited directly by the piezoelectric actuator at the center of the plate. For all presented scans only the out-of-pane displacements are shown. The in-plane components measured by the 3D laser scanning vibrometer have been used to facilitate the identification of the S_0-mode. However, no additional information is obtained.

Inside the S_0-mode other waves occur. These unexpected new waves are characterized by plane wave fronts being nearly parallel to each other. The orientation of the wavefront of the new modes depends on the region where the modes arise. In the bottom left of

---

[2]marco Systemanalyse und Entwicklung GmbH, see: http://www.marco.de/E/index.html Oct. 13 2011

Figure 5.16 the different orientation between two wavefronts is shown. In addition, the new waves do not occur everywhere in the plate.
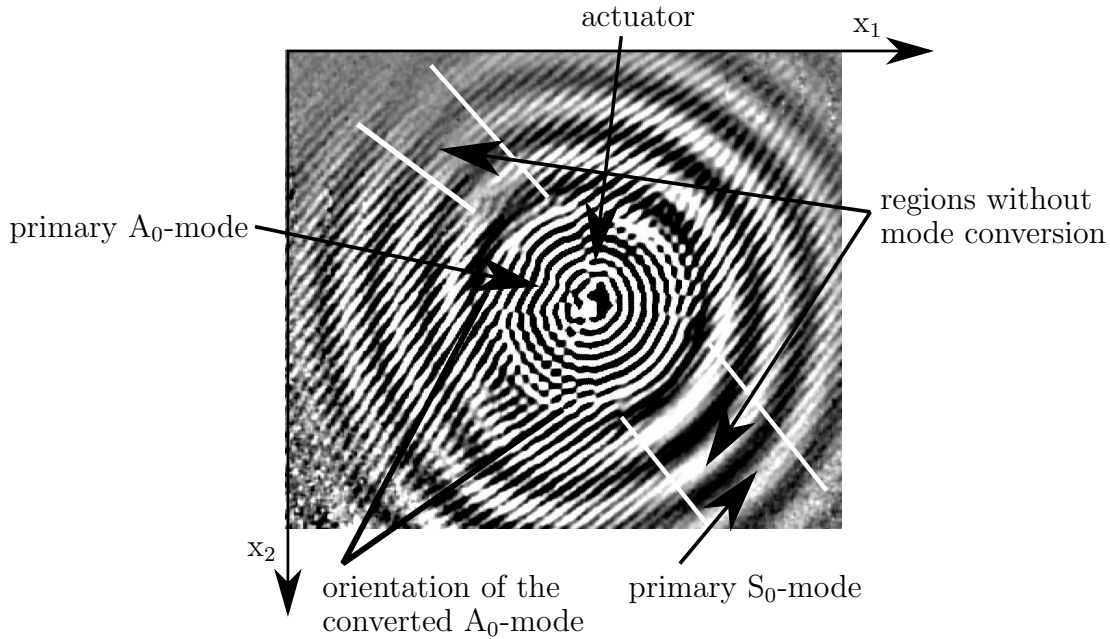
Figure 5.16: *Lamb* wave propagation in a CFRP plate at $f = 200\,\text{kHz}$, excited with a actuator in the center $(300\,\text{mm} \times 250\,\text{mm})$.

At 200 kHz the upper left and the lower right regions do not show new modes. Nevertheless, these regions change if *Lamb* waves are excited with another frequency. All investigated frequencies show that the orientation of the modes remain similar. The effect first takes place for the presented CFRP plate at 138 kHz and appears at all investigated frequencies from $138 - 350\,\text{kHz}$.

(A) Phase velocity

(B) Group velocity
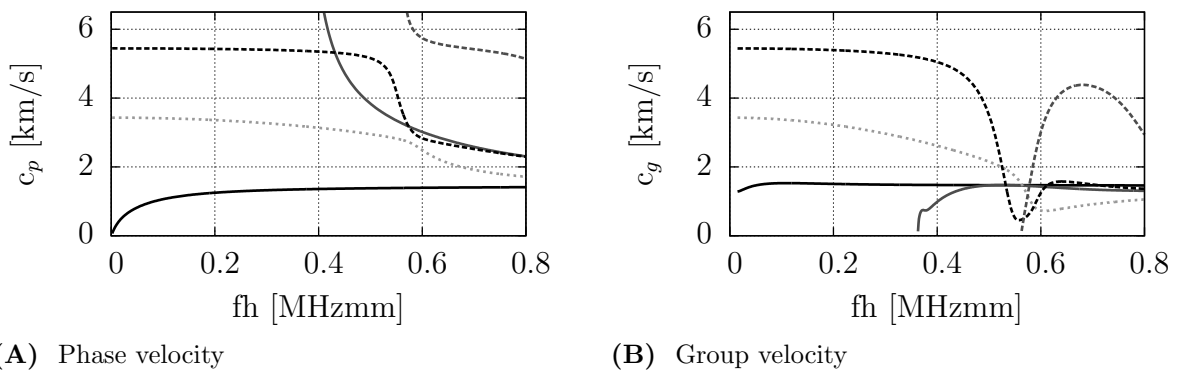
Figure 5.17: Dispersion curves for the quasi-isotropic CFRP plate in 0°-direction with thickness h.

In the following it is tried to clarify what type of mode arises in the S_0-wave field in Figure 5.16. Figure 5.17 shows the dispersion curves of the presented CFRP plate. The curves have been calculated with the help of the semi-analytical finite element (SAFE) method. The SAFE results have been validated with experimental data from the investigated CFRP plate [4].

The dispersion curves of the plate show that for frequencies lower than 205 kHz only three modes exist, the anti-symmetric A_0-, the shear-horizontal SH_0- and the symmetric S_0-mode. Above this frequency a fourth mode appears, the A_1-mode. At frequencies higher than 280 kHz the symmetric S_1-mode occurs. In Figure 5.16 it can be seen that the anti-symmetric A_0-mode has a shorter wavelength and because of the lower group velocity (see Figure 5.17B) its wave field is next to the source. The waves inside the S_0-mode have wavelengths similar to the A_0-mode. The C-scan example correlates to the entry 0.4 MHzmm in the dispersion curves (see Figure 5.17). For the presented frequency two higher order modes can occur. Nevertheless, the phase velocities c_p of the A_1-, S_1- and SH_0-mode are significantly higher in comparison to the A_0-mode. Therefore, the wavelength

$$\lambda = \frac{c_p}{f} \tag{5.5}$$

has to be longer. Because the wavelengths of the new mode are close to the A_0-mode it is assumed that a dominant conversion between the S_0- and the A_0-mode occurs. However, the mode conversion does not take place at a specific discontinuity, but continuously while the S_0-mode travels through the plate.

5.4.3 The identification of CMC

In the following section arguments are gathered to identify the converted mode as A_0-mode. Because the A_0-mode is slower than the S_0-mode, the existence of the anti-symmetric mode inside the S_0-wave field is an evidence for CMC. Six identically produced CFRP plate have been investigated. All of them show an analogous behavior. Therefore, a random local damage inside the plate can be excluded as source of this mode conversion.

Figure 5.18A shows a strip of the *Lamb* wave C-scan taken from a plate. The source is located at the left side. The primary modes are already separated from each other. In the space between both primary modes a number of oblique waves can be seen. Using the center line perpendicular to the wave front of the primary modes the C-scan strip can be transformed into a B-scan. With the B-scan group velocity of the different *Lamb* wave modes can be visualised. The time-amplitude data of each point of the center line of Figure 5.18A is plotted side by side as illustrated in Figure 5.18B. The heights of the amplitudes at a specific time and position are visualised by the gray scale. Dark gray illustrates negative and bright gray positive amplitude values.
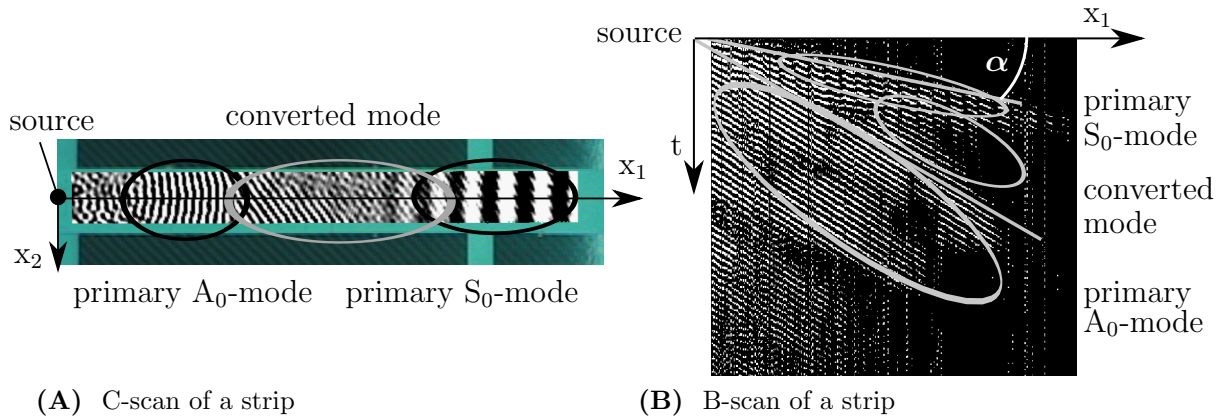
(A) C-scan of a strip

(B) B-scan of a strip

Figure 5.18: Analysis of the new mode at $f = 200\,\text{kHz}$.

If a *Lamb* wave is excited by a burst signal, at least three primary groups of waves travel through the plate which may separate from each other (A_0, SH_0, S_0). The groups propagate with different velocities. The B-scan displays the movement of these groups by oblique parallel lines. The inclinations of the lines correspond to the group velocities (see Figure 5.17B) of the excited modes. The dominant lines with the highest amplitudes correspond to the central frequency of the burst signal. Smaller angles α between the lines and the x_1-axis indicate a higher velocity. Therefore, the upper lines correspond to the S_0-mode, whereas the lower lines belong to the anti-symmetric A_0-mode. The shear horizontal mode has very low amplitudes in out-of-plane direction. Therefore, this mode can not be seen in the B-scan and is not taken into account in the further investigation.

If one starts at the origin of the coordinate system corresponding to the location of the piezoceramic transducer and draws a line which has the inclination of the A_0-mode (taken from Figure 5.17A), the position of the primary A_0-mode in the B-scan can be found. It must be noted that the A_0-mode is highly dispersive. The group velocity of the A_0-mode varies for different frequencies. In reality a mono-frequent excitation is not feasible. Depending on the bandwidth of the excitation signal multiple A_0-modes are included in one group. Some of these modes travel faster than the group velocity of the chosen excitation frequency. However, these faster parts of the group are created inside the original A_0-mode group and have a higher velocity with a lower angle α.

In Figure 5.18B lines between the primary A_0- and S_0-modes can be seen, which start in the area corresponding to the S_0-mode. An extension of these lines to $t = 0$ s does not cut the source ($x_1 = 0$) but the inclination of these lines is equal to the inclination of the primary A_0-mode. This mode has to be created continuously by a mode conversion from S_0- to A_0-mode. The B-scans of other frequencies show similar effects [75] .

5.4.4 Experimental and numerical investigation of CMC

Analysis of the problem

After presenting the phenomenon of continuous mode conversion, it is tried to explain its appearance. The conversion between two modes occurs if a *Lamb* wave mode encounters a discontinuity in such way, that parts of the particle movement activate another mode. Typically mode conversion happens locally at holes, damages, etc.

(A) Pure S_0-mode

(B) Conversion of S_0- in A_0-mode
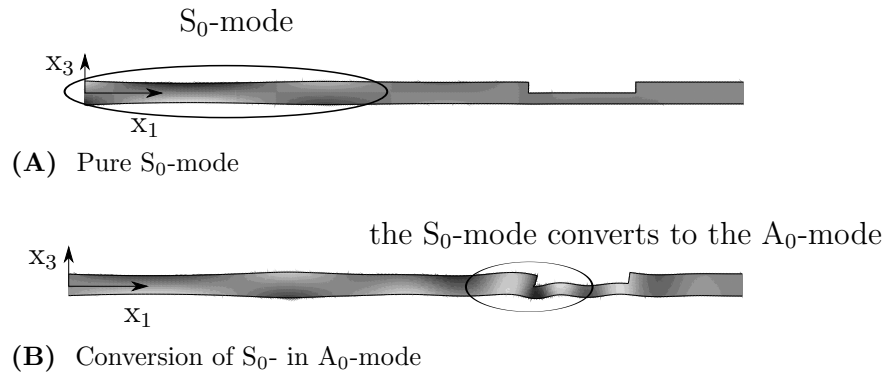
Figure 5.19: Example of a mode conversion in a two-dimensional model of an aluminum plate.

Figure 5.19 shows a two-dimensional example to explain mode conversion at a flat bottom hole. A symmetric mode is excited at the left edge and travels (see Figure 5.19A) through the plate. If the symmetric mode reaches the flat bottom hole a mode conversion takes place (see Figure 5.19B). The symmetric mode in an isotropic material has an approximately constant in-plane displacement over the thickness of the plate. If the mode travels through the flat bottom hole the stiffness changes over the height. In the upper part of the plate the wave is reflected and in the lower part the mode travels further, which causes a bending (see Figure 5.19B) of the plate. Because the anti-symmetric mode is a bending mode, parts of the energy of symmetric mode are transferred to the anti-symmetric one and two modes exist.

In the following part it is tried to explain why CMC takes place in the presented CFRP plate. Figure 5.20 shows a strip of the *Lamb* wave C-scan with a length of $l = 64$ mm. Besides the measured data a photograph of the plate surface is displayed. The texture of the bottom layer made of twill fabric can be identified. The drawn skew lines are an extension of the fabrics texture. The distance between two lines is 2 mm. It can be seen that the wave front of the continuously converted mode corresponds to this direction.

Figure 5.20: Influence of twill fabric to the S_0-mode wave front caused by CMC. The skew lines illustrate the texture caused by the twill fabric, which influence the A_0-mode.

The top layer is also made of twill fabric which is displayed in Figure 5.21A. It is assumed that the texture of the fabric displayed by the skew lines causes the mode conversion. A

plain fabric layer is also a part of the CFRP plate. The plain fabric also has a texture like the twill fabric (skew broken lines in Figure 5.21B). However, experimental inve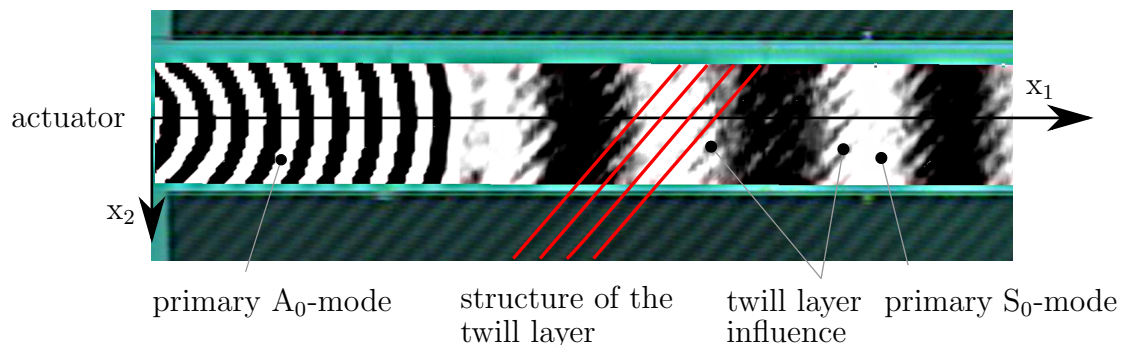stigations have shown that CMC does not take place [75]. Therefore, in the following sections the *Lamb* wave propagation in twill fabrics is studied. Experimental and numerical models are used to facilitate the interpretation.

(A) Twill fabric   **(B)** Plain fabric
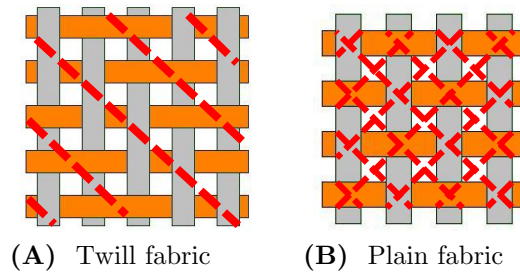
Figure 5.21: Fabric types in the CFRP plate and their textures (skew lines)[133].

Twill fabric - experimental investigation

The experiments are conducted utilizing a single layer twill fabric plate ($1\,\text{m} \times 1\,\text{m} \times 0.3\,\text{mm}$). Because of the plates thickness the measurements are done several times after rotating the plate. The same results for all measurements have been obtained, which means that the influence of the bending of the plate caused by its own weight to the results of the measurements can be neglected. In Figure 5.22A the C-scan for a frequency $f = 50$ kHz is plotted. The mode conversion occurs primarily in 0°-, 90°-, 180°- and 270°-direction. Perpendicular and parallel to the texture of the twill fabric no mode conversion takes place. The CMC arises at all measured frequencies $f > 20\,\text{kHz}$. In Figure 5.22B the B-scan at 50 kHz in 0°-direction is plotted. The symmetric mode cannot be seen by displaying the out-of-plane components of the laser vibrometer measurements. The line corresponding to the primary S_0-mode is plotted by connecting the starting points of the converted mode. Besides the primary, a converted A_0-mode starts inside the S_0-mode.

(A) C-scan with actuator in the center ($100\,\text{mm} \times 100\,\text{mm}$)   **(B)** B-scan
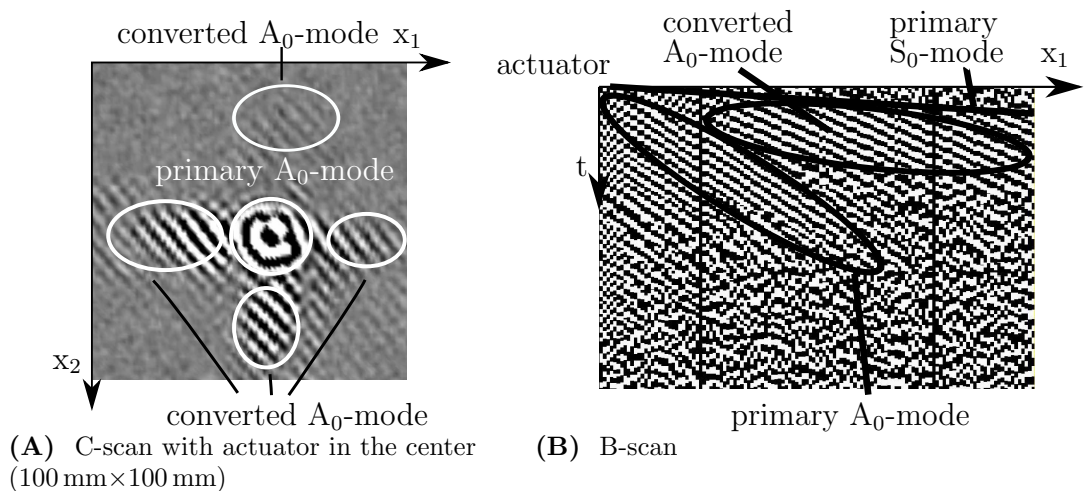
Figure 5.22: Experimental investigation of a one layer twill fabric for $f = 50\,\text{kHz}$.

Twill fabric - numerical investigation

Figure 5.23 shows a part of the twill fabric model. The length and the thickness of the quadratic twill fabric cell model are defined as $l_f = 8\,\text{mm}$ and $h_{pl} = 0.3\,\text{mm}$. The homogenized material properties are given in Table A-7 (UD-Layer). The experiments are performed on a plate consisting of a single twill fabric layer.
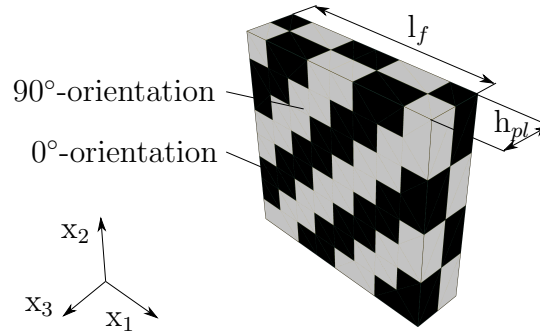
Figure 5.23: Twill fabric without matrix material ($l_f = 16\,\text{mm}$, $h_{pl} = 0.3\,\text{mm}$).

To reduce the numerical effort the fibres are approximated as cubes and the matrix material is included in the parameters of the homogenized material. However, the orientation of the fibres as well as the texture of the fabric has been included. To excite the Lamb waves collocated point force at the center of the plate with a time-dependent amplitude following a sine burst signal (see Equation (4.17)) have been used. The section displayed in Figure 5.23 is copied several time to reach the plate size of $0.2\,\text{m}\times0.2\,\text{m}\times0.3\,\text{mm}$. The simulation has been done utilizing the isogeometric finite elements.
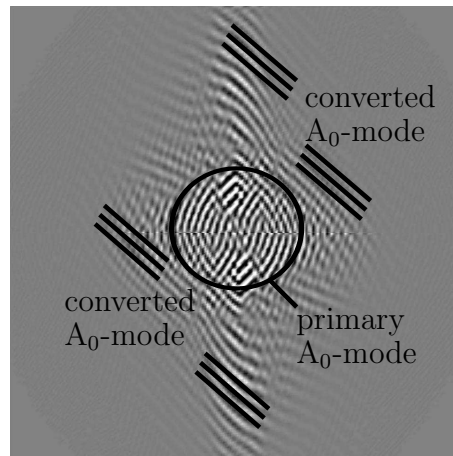
Figure 5.24: Numerical results of a one layer twill fabric plate ($0.2\,\text{m}\times0.2\,\text{m}\times0.3\,\text{mm}$) for $f = 50\,\text{kHz}$ and $t = 8.5 \cdot 10^{-6}\,\text{s}$.

In Figure 5.24 a result of the simplified numerical twill fabric model for a frequency $f = 50\,\text{kHz}$ at a time $t = 8.5\cdot10^{-6}\,\text{s}$ is shown. The phenomenon of continuous mode conversion is to be observed as well. The main regions where CMC occurs are similar to the experiments

(black parallel lines). The mode conversion mainly takes place in 0°-, 90°-, 180°- and 270°-direction. The orientation of the converted mode agrees with the experiments. Hence, it can be inferred that the model is able to qualitatively capture the physical behaviour of the twill fabric plate.

After the preliminary analysis of CMC with a simplified model a more detailed isogeometric model is created. Using a more complex model it is hoped to discover an explanation for the CMC phenomenon. Figure 5.25 shows a part of the one layer twill fabric plate which has been analysed in the experiments. Each cell has a width and length $a = 2$ mm and the plate thickness is $h_{pl}/2 = 0.15$ mm (see Figure 5.23). The complete plate has a dimension of (16 mm×8 mm×0.3 mm). The cell has been modeled with elliptic fibres inside the matrix material. However, the transition of the fibres between top and bottom has not been considered. The material properties of the fibres and the matrix are given in Table A-8.
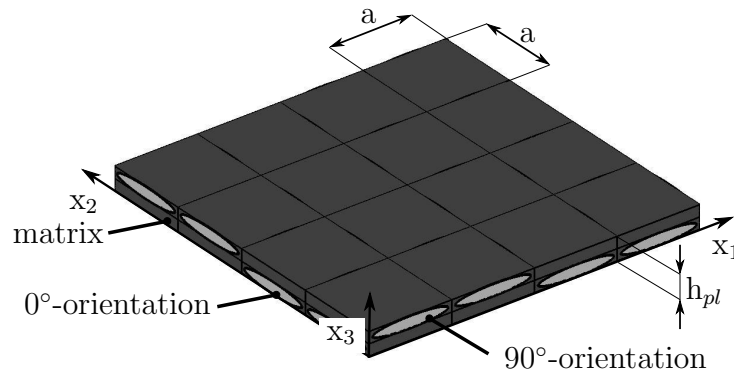
Figure 5.25: Part of a twill fabric (see experimental results in Figure 5.22) plate modeled with isogeometric finite elements ($a = 2$ mm, $h_{pl} = 0.3$ mm).

As illustrated in chapter 2 the in-plane displacement of the symmetric S_0-mode in an isotropic plate is approximately constant over the thickness (see Figure 2.4A for the isotropic case). It is assumed, that the reason for the mode conversion is, that constant in-plane displacements with respect to the center plane cause non-symmetric out-of-plane displacements. To study this assumption a one-dimensional tensile test has been computed for a small twill fabric strip (16 mm×8 mm×0.3 mm), applying an external uniform displacement $u_1(x_1{=}0){=}0.2$ mm. The boundary condition are given as ($u_1(x_1{=}16$ mm)=0, $u_2(x_2{=}0){=}0$, $u_3(x_1{=}0, x_3{=}0){=}0$).
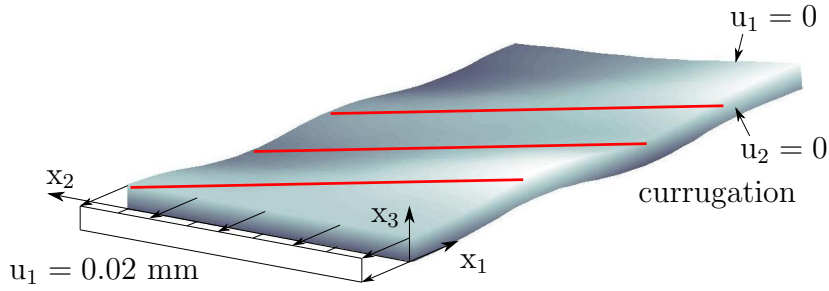
Figure 5.26: Results of a one-dimensional tensile test $(16\,\mathrm{mm}\times 8\,\mathrm{mm}\times 0.3\,\mathrm{mm})$.

Figure 5.26 shows the result of the computation with the detailed isogeometric model. A constant symmetric displacement is applied to the boundary surface and used to model the tensile test. As one can see this load causes corrugations inside the plate. A strong in-plane - bending coupling occurs, because the in-plane stiffness of the plate is non-symmetric with respect to the center plane. Therefore, the strains caused by an one-dimensional tensile test are not constant over the thickness. The orientation of the corrugation agrees with the texture of the twill fabric. In section 5.4.4 it has been explained that a non-symmetric change of plate stiffness as a flat bottom hole is able to cause mode conversion. In the twill fabric this non-symmetric stiffness changes exist periodically everywhere in the plate. Therefore, the mode conversion can occur continuously. If the loads are applied in a direction parallel and perpendicular to the texture of the twill fabric no corrugations can be observed [166]. This behavior coincides with the experimental findings, where the conversion does not occur in 45°, 135°, 225° and 315°-direction. In this case the stiffness of the plate is symmetric with respect to the center plane. A analysis of wave propagation in the detailed model has not be done until now, due to the high computational effort.

5.4.5 Summary

In this chapter two SHM specific problems have been investigated both experimentally and numerically. The first problem studies parameters, which mainly influence the *Lamb* wave excitation using piezoceramic transducers. The comparison of the numerical eigenfrequency analysis with the experimental results of a free piezoceramic disc shows that the impact of both a soldering point and a wire is low and can be neglected. The discrepancy between the simulation and the experiments is, with the exception of one eigenfrequency, lower than 10%.

In the next part of the chapter the experiments have been introduced which show that the resonances of the coupled actuator-structure system have a great impact on the spectra of the *Lamb* wave modes. The general properties could be reproduced by the developed two-dimensional finite element model. Therefore, the two-dimensional isogeometric finite element model has been used to study the impact of varying several parameters. The findings gained in chapter 4 have been used to minimize the computational effort.

The variation of the adhesive layer thickness shows that only great thickness changes influence the position of the first peak in the S_0-mode spectrum noticeably. Therefore, this parameter could be used to adapt the position of the first peak. However, small variation in the adhesive layer thickness barely influence the position of the peak and thickness variations during the production process do not have to be taken into account for the design. The *Young*s modulus of the adhesive layer has a low impact on the first peak in the S_0-

mode spectrum as well as to the corresponding amplitude. Small variations of the material properties of the adhesive layer during the production process or caused by temperature variations do not change the dynamical behavior of the piezoceramic actuator significantly. The variation of the actuator length shows that for longer patches the frequency of the first peak in the S_0-mode spectrum decreases. This correlates with the analytical formulation of the radial eigenfrequency of a circular disc. The corresponding amplitudes increase and decrease. The bending and the radial mode of the piezoceramic are differently influenced by changing the length of the actuator. Therefore, for a specific frequency both modes superimpose. As a result the amplitudes of the excited S_0-mode are increased. An optimal energy efficient actuator design tries to superimpose both resonances.

The variation of the thickness of the actuator shows that the optimal *Lamb* wave excitation is not only dependent on the length of the actuator. For greater thicknesses the frequency of the first maxima of the symmetric mode is reduced. The amplitude of this maximum increases for a greater thickness. This numerical result agrees with the experimental findings and disagrees with "shear lag" predictions. The resonances of the actuator have a great impact on the excited *Lamb* wave mode. This effect covers the "shear lag" effect and is more dominant in influencing *Lamb* wave amplitudes than the adapted length proposed by Giurgiutiu et al. [49].

The variation of the plate *Young*s modulus shows that the position of the first peak in the S_0-mode spectrum is dominantly influenced by the piezoceramic source. The amplitudes, except for soft plates ($Y_{pl} < 10^{11}$ N/m^2), show only small variations.

In summery the design of an optimal shaped piezoceramic actuator (working in resonance) could be made for a fixed adhesive layer and a given plate material. Small changes in the adhesive layer, actuator geometry and plate stiffness do not dominantly change the behavior of the piezoceramic source.

The second SHM specific problem deals with the effect of material induced continuous mode conversion in a CFRP plate. The effect has been observed first in a multi-layer composite plate, where 50% of the whole plate is made of fabrics. For the investigated CFRP plate the effect of CMC first occurs around 138 kHz and is identified as mode conversion from S_0- to A_0-mode. For this identification the dispersion curves as well as B-scans are used.

For a better understanding of the CMC effect a pure twill fabric plate is analysed both experimentally and numerically. In the experiments the conversion arises for all investigated frequencies $f > 20$ kHz. The orientation of the wavefront of the converted A_0-mode is parallel to the texture of the twill fabric. The new mode occurs only in 0°-, 90°-, 180°- and 270°-direction.

The isogeometric elements are a useful tool to model fabric plates. In that case the numerical effort is reduced. The main behavior of CMC can be described using a simplified model. A detailed analysis which takes the fibres and the matrix material into account has been done for the static case. It has been found that an uniform tensile test causes corrugations in the plate. This shows a strong coupling between the approximately constant in-plane displacements of the S_0-mode and non-symmetric out-of-plane displacements (with respect to the center plane). This coupling might be the reason for CMC. A dynamic analysis of the detail model has not be done until now because the computational effort is too high.

6 Conclusion and outlook

In the thesis an isogeometric piezomechanical finite element for the design of *Lamb* wave based SHM applications has been developed, studied and utilized for two SHM based problems. To model *Lamb* wave propagation problems a high spatial and temporal discretization is required. Furthermore, structures which should be monitored have often a complex geometry. Therefore, an isogeometric approach has been used to guarantee an exact geometrical description. However, a coupled piezomechanical isogeometric element to model actuators as well as sensors for SHM purposes did not exist, yet. Moreover, the behavior of isogeometric finite elements in the dynamic case has not been studied. Thus, the dynamic behavior regarding ultrasonic guided waves has been scrutinized. Hence, novel results with respect to transient analysis using isogeometric finite elements have been gained. The questions stated in the introduction can be answered as follows:

(a) Several benchmarks show that isogeometric finite elements are an effective numerical tool to model *Lamb* wave based problems.

(b) The quality of the solution of the isogeometric elements of *Lamb* wave propagation problem have been determined using benchmark calculations and comparisons to other numerical approaches. Furthermore, guidelines have been proposed to estimate the accuracy a priori for a given polynomial degree.

(c) The inter-element-continuity has a huge impact on the convergence behavior of the isogeometric finite element.

(d) Isogeometric finite elements with a C^{p-1} inter-element-continuity need fewer number of degrees-of-freedom to solve *Lamb* wave propagation problems compared to the spectral finite elements and the p-finite elements.

(e) Isogeometric elements are able to describe SHM specific problems in complex geometries.

6.1 Conclusion

The most important findings of the thesis can be divided in two parts. The results of the first part are related to the numerical aspects of the developed isogeometric piezomechanical finite element. The second part is related to the application of this finite element to two SHM based problems, where experimental investigations as well as application of the new NURBS elements have been used.

The new 3D isogeometric piezoelectric finite elements have been tested by solving several benchmark tests and a good agreement to analytical, numerical and experimental solutions has been found. Furthermore, it is shown that a better geometrical approximation with isogeometric finite elements, e.g. if circular piezoelectric patches are used, results in a far more accurate solutions in comparison to standard isoparametric finite elements with a significantly lower number of degrees-of-freedoms (50 % less degrees-of-freedom for the piezoceramic ring actuator in section 3.5.3). Regarding the complexity of real structures

the developed isogeometric piezoelectric finite element leads to a reduction in computational time as well as memory requirements for piezomechanical problems in comparison to standard low order finite elements. Moreover, it has been shown that isogeometric elements are not prone to shear locking. Moderately distorted elements $a/h < 180$ do not influence the quality of the solution noticeably.

Although the advantages of the isogeometric finite elements have been shown in various publications the quality of *Lamb* wave simulation and the convergence behavior for this type of elements were unknown until now. Therefore, in chapter 4 the isogeometric finite element has been compared to two other higher order finite element schemes with respect to their suitability concerning *Lamb* wave propagation analysis. As reference solution the group velocity of the analytical *Lamb* wave solution has been used. The relative error of the three approaches (SEM, p-FEM, N-FEM) has been studied. The developed isogeometric element offers the highest convergence rate in comparison to the two other approaches. The maximum accuracy is equal to the other two methods. So far, if the presented memory criteria (relative error lower than 1 %) is used the isogeometric elements would have to be recommended due to their high convergence rates and therefore the lowest memory consumption. Furthermore, if a complex geometry needs to be modeled, isogeometric finite elements would certainly have an advantage compared to other methods, because no extra blending-function method is needed [20]. As an optimal polynomial degree for ultrasonic guided wave propagation it has been found $p_{x_1} = p_{x_2} = 3$ and $p_{x_3} = 4$. By utilizing 4.5 "nodes-per-wavelength" the relative error with respect to the group velocity is lower than 1 %. This optimal discretization has been used to model complex 3D plates as well as higher order *Lamb* wave modes [164].

When scrutinizing isogeometric finite elements the order of inter-element-continuity is a variable which has a strong influence on convergence rate of the solution. The studies show that a higher order of inter-element-continuity influences the convergence rate of the isogeometric elements in a positive way. Therefore, it is recommended to use the highest inter-element-continuity possible C^{p-1}.

The main findings of the first part,

- isogeometric piezomechanical finite elements are an efficient tool to simulate piezo-ceramic actuators,
- shear locking has a low impact on isogeometric elements,
- optimal discretization scheme: $p_{x_1} = p_{x_2} = 3$ and $p_{x_3} = 4$ with 4.5 "nodes-per-wavelength" and C^{p-1}-continuity leads to less than 1% error of the group velocity,
- all physical aspects of *Lamb* waves (e.g. mode conversion, dispersion) can be modelled,

have been used to investigate two SHM specific problems in the second part of the thesis. The first problem is related to the excitation process of the *Lamb* waves. Experimental findings have shown a coupling between the actuator resonances and the spectra of the *Lamb* wave modes [116]. A variation of several parameters, the adhesive layer thickness and *Young*s modulus, the actuator length and thickness, and the *Young*s modulus of the plate, have been conducted. The new isogeometric piezoelectric finite elements have been used to create a two-dimensional model. With help of this model all parameters have been varied and their impact on the excitation of the *Lamb* waves has been studied.

The variation of the adhesive layer thickness shows that this parameter can be used to adjust the dynamic properties of the piezoceramic source. However, small variations in the adhesive layer thickness cause only small changes in the dynamic behavior of the actuator.

Therefore, it is robust against small variations in the production process.

Higher *Young*s moduli cause a reduction in the amplitude. This behavior disagrees with the "shear lag" effect and underlines that for thicker piezoceramics the eigendynamic superimposes this effect. But variations of the material properties of the adhesive layer do not seem to influence the first resonance frequency drastically.

The variation of the actuator length shows that for longer patches the frequency decreases. This correlates with the analytical formulation of the radial eigenfrequency of a disc.

The variation of the thickness of the actuator shows that an optimal *Lamb* wave excitation is not only depended on the length of the actuator. For thicker piezoceramic patches the resonance superimpose the effects of optimal length given by Giurgiutiu [49]. For higher thicknesses the frequency of the first maximum of the symmetric mode is reduced. The amplitude of this maximum increases for an increased thickness.

In summery it is to say, that the well known "shear lag" model does not predict all the observed effects. Moreover, the effects caused by the adhesive layer all small and slight parameter variations typical for the production process can be neglected. The dynamic behavior of the piezoceramic is dominantly influenced by their geometry.

The second SHM related problem is the material induced phenomenon of continuous mode conversion (CMC). The description of this new effect is done with experimental data. It has been found that the stacking sequence of the CFRP plate leads to CMC. In detail the twill fabric causes the mode conversion. Therefore, a simple twill fabric has been modeled utilizing the new isogeometric elements. This model is capable to describe the experimental findings. A more detailed model including fibres as well as matrix material shows that a strong in-plane-bending-coupling exists. This strong coupling is an indicator for the appearance of CMC. However, because of the numerical effort it is not possible to use this detailed model to calculate *Lamb* wave propagation, yet.

The thesis has shown that isogeometric finite elements have a great potential in modeling *Lamb* wave based problems. The three-dimensional piezomechanical ansatz of the approach gives a flexible tool to model various SHM related problems. Furthermore, the high convergence rate reduces the numerical effort for high-frequency simulations. Moreover, the consideration of the piezoelectric material properties allows an holistic description of complete SHM systems including actuators and sensors.

6.2 Outlook

Despite the good results there are several open questions for future work with isogeometric finite elements for *Lamb* wave based problems. First of all the isogeometric finite element has to be tested with several time integration schemes. The used *Runge-Kutta* algorithm is not efficient. If a mass lumping technique could be developed a finite difference method might be a more suitable and numerically efficient approach. Moreover, in future work a tool has to be developed which facilitates the exchange between CAD tools and the finite element code. That includes the prevention of highly distorted elements. NURBS can describe the geometry very efficiently, but for that in the CAD tool the size and distortion of the patches or (later) elements are arbitrarily [27]. Therefore, CAD tools are needed which consider the suitability of the geometrical description with respect to a FEM discretization. For time integration schemes especially for explicit time integration methods the element size and distortion is very important. The CAD tool should be capable to use

as little patches as possible to preserve the advantage of the k-refinement, particularly for *Lamb* wave simulation.

The numerical integration effort can be reduced by applying efficient quadrature rules, e.g. the "half-point rule" proposed by Hughes [67]. Furthermore, the impact of the exact geometrical description of the NURBS to the quality of the solution of *Lamb* wave propagation problems has to be investigated. If an exact description is not needed the finite cell method (FCM) shows a high potential for the simulation particulary for cellular materials [108]. However, these simulations have been done only for static and eigenfrequency analysis. For several problems the comparison between the p-FEM and the B-spline based FCM are in good agreement [129]. An extension of the results to dynamic analysis has still to be done. The findings of this thesis show that for NURBS the convergence rate are drastically higher in comparison to the p-FEM due to the k-refinement. Therefore, the capability of FCM with a NURBS ansatz for *Lamb* wave simulations in honeycombs, foam and fabric material has to be studied [61]. In the current thesis all calculations are done in the time-domain. The properties of a isogeometric approach in the frequency domain have not been studied to date as well.

A Material data

Table A-1: Material data for aluminum.

parameter	unit	value
Y	$[10^9 \text{ N/m}^2]$	70
ν	[-]	0.3
c_1	[m/s]	6197
c_2	[m/s]	3121
ρ	$[\text{kg/m}^3]$	7760

Table A-2: Material data for the bimorph beam [95].

parameter	unit	PVDF layer
Y	$[10^9 \text{ N/m}^2]$	2
ν	[-]	0.29
b_{31}	$[\text{C/m}^2]$	-0.046
b_{32}	$[\text{C/m}^2]$	-0.046
ϵ_{33}	$[10^{-10} \text{ F/m}]$	1.062

Table A-3: Material properties of the active plate [74].

parameter	unit	PZT G1195	T300/976
layer thickness		$0.254\,mm$	$0.138\,mm$
S_{11}^E	$[10^{-12}\,\text{m}^2/\text{N}]$	1.587	6.666
S_{22}^E		15.87	111.1
S_{44}^E		41.32	140.8
S_{66}^E		41.32	400.0
ν_{12}	[-]	0.3	0.018
ν_{23}		0.3	0.3
b_{31}	$[\text{C/m}^2]$	-22.86	-
b_{32}		-22.86	-

Table A-4: Piezoelectrical material properties with the electric constant $\epsilon_0 = 8.8542 \cdot 10^{-12}$ As/(Vm) [136]

parameter	unit	PZT-5H
Y	$[10^9 \text{ N/m}^2]$	174
ν	[-]	0.3
d_{31}	$[10^{-10} \text{ m/V}]$	-2.74
d_{33}		5.93
$\epsilon_{33}^T/\epsilon_0$		3399
ρ	$[\text{kg/m}^3]$	7760

Table A-5: Piezoelectrical material properties with the electric constant $\epsilon_0 = 8.8542 \cdot 10^{-12} As/(Vm)$ [2].

parameter	unit	PIC-151	PIC-181
S_{11}^E	$[10^{-12}\text{m}^2/\text{N}]$	16.83	11.75
S_{33}^E		19.00	14.11
S_{55}^E		50.96	35.33
S_{12}^E		-5.66	-4.07
S_{13}^E		-7.11	-4.996
S_{44}^E		50.96	35.33
S_{66}^E		44.97	31.64
d_{31}	$[10^{-10}\text{m/V}]$	-2.14	-1.08
d_{33}		4.23	2.53
d_{15}		6.1	3.89
$\epsilon_{11}^T/\epsilon_0$	$[-]$	1936	1224
$\epsilon_{33}^T/\epsilon_0$		2109	1135
ρ	$[\text{kg/m}^3]$	7760	7850

Table A-6: Material data for paraffin [170].

parameter	unit	value
Y	$[10^9 \text{ N/m}^2]$	1
ν	[-]	0.3
ρ	$[\text{kg/m}^3]$	1100

Table A-7: Material properties of a carbon fibre reinforced plastic (CFRP) plate [131].

parameter	unit	twill fabric	plain fabric	UD-layer
Y_{11}	$[10^9\,\mathrm{N/m^2}]$	49.6	53.4	127.5
Y_{22}		49.6	53.4	7.9
Y_{33}		6.1	6.4	-
G_{12}		3.56	3.83	5.58
G_{23}		2.67	2.87	2.93
G_{31}		5.58	2.93	-
ν_{12}	[-]	0.03	0.03	-
ν_{23}		0.322	0.319	0.273
ν_{31}		0.034	0.033	-
ρ	$[\mathrm{kg/m^3}]$	1520	1560	1550

Table A-8: Non-homogenized material parameter of a twill fabric plate [52].

parameter	unit	T400	EP 6376
Y_{11}	$[10^9\,\mathrm{N/m^2}]$	250	3.3
Y_{22}		16.68	-
G_{12}		20.8	-
ν_{12}	[-]	0.24	0.36
ν_{23}		0.3	-
ρ	$[\mathrm{kg/m^3}]$	1800	1230

B NURBS surface and volume description

The NURBS surface can be calculated as

$$R_{i,j}^{p_{x_1},p_{x_2}}(\beta,\,\gamma) = \frac{N_{i,p_{x_1}}(\beta)M_{j,p_{x_2}}(\gamma)w_{i,j}}{\sum\limits_{\hat{i}=1}^{n_{cont}}\sum\limits_{\hat{j}=1}^{m_{cont}} N_{\hat{i},p_{x_1}}(\beta)M_{\hat{j},p_{x_2}}(\gamma)w_{\hat{i},\hat{j}}}$$

$$\mathbf{NS}(\beta,\gamma) = \sum\limits_{i=1}^{n_{cont}}\sum\limits_{j=1}^{m_{cont}} R_{i,j}^{p_{x_1},p_{x_2}}(\beta,\gamma)\mathbf{P}_{i,j}\,.$$

(B-1)

The notation is given in section 2.5. The NURBS surface derivative can be calculated separately for each direction

$$\frac{\partial}{\partial\beta}R_{i,j}(\beta,\,\gamma) = \frac{W(\beta,\,\gamma)N'_{i,p_{x_1}}(\beta)M_{j,p_{x_2}}(\gamma) - W'(\beta,\,\gamma)N_{i,p_{x_1}}(\beta)M_{j,p_{x_2}}(\gamma)}{W(\beta,\,\gamma)^2}\,,$$

$$W(\beta,\,\gamma) = \sum\limits_{\hat{i}=1}^{n_{cont}}\sum\limits_{\hat{j}=1}^{m_{cont}} N_{\hat{i},p_{x_1}}(\beta)M_{\hat{j},p_{x_2}}(\gamma)w_{\hat{i},\hat{j}}\,,$$

$$W'(\beta,\,\gamma) = \sum\limits_{\hat{i}=1}^{n_{cont}}\sum\limits_{\hat{j}=1}^{m_{cont}} N'_{\hat{i},p_{x_1}}(\beta)M_{\hat{j},p_{x_2}}(\gamma)w_{\hat{i},\hat{j}}\,,$$

$$\frac{\partial}{\partial\beta}\mathbf{NS}(\beta,\gamma) = \sum\limits_{i=1}^{n_{cont}}\sum\limits_{j=1}^{m_{cont}} \frac{\partial}{\partial\beta}R_{i,j}^{p_{x_1},p_{x_2}}(\beta,\gamma)\mathbf{P}_{i,j}\,.$$

(B-2)

The NURBS volume can be calculated utilize

$$R_{i,j,k}^{p_{x_1},p_{x_2},p_{x_3}}(\beta,\,\gamma,\,\zeta) = \frac{N_{i,p_{x_1}}(\beta)M_{j,p_{x_2}}(\gamma)O_{k,p_{x_3}}(\zeta)w_{i,j,k}}{\sum\limits_{\hat{i}=1}^{n_{cont}}\sum\limits_{\hat{j}=1}^{m_{cont}}\sum\limits_{\hat{k}=1}^{o_{cont}} N_{\hat{i},p_{x_1}}(\beta)M_{\hat{j},p_{x_2}}(\gamma)O_{\hat{k},p_{x_3}}(\zeta)w_{\hat{i},\hat{j},\hat{k}}}\,,$$

$$\mathbf{NV}(\beta,\gamma,\zeta) = \sum\limits_{i=1}^{n_{cont}}\sum\limits_{j=1}^{m_{cont}}\sum\limits_{k=1}^{o_{cont}} R_{i,j,k}^{p_{x_1},p_{x_2},p_{x_3}}(\beta,\gamma,\zeta)\mathbf{P}_{i,j,k}\,,$$

(B-3)

and analogously to Equation (B-2) the NURBS volume derivative in each direction is computable using

$$\frac{\partial}{\partial \beta} R_{i,j,k}(\beta,\, \gamma,\, \zeta) = \frac{\left[W(\beta,\, \gamma,\, \zeta) N'_{i,p_{x_1}}(\beta) - W'(\beta,\, \gamma,\, \zeta) N_{i,p_{x_1}}(\beta) \right] M_{j,p_{x_2}}(\gamma) O_{k,p_{x_3}}(\zeta)}{W(\beta,\, \gamma,\, \zeta)^2}$$

$$W(\beta,\, \gamma,\, \zeta) = \sum_{\hat{i}=1}^{n_{cont}} \sum_{\hat{j}=1}^{m_{cont}} \sum_{\hat{k}=1}^{o_{cont}} N_{\hat{i},p_{x_1}}(\beta) M_{\hat{j},p_{x_2}}(\gamma) O_{\hat{k},p_{x_3}}(\zeta) w_{\hat{i},\hat{j},\hat{k}}$$

$$W'(\beta,\, \gamma,\, \zeta) = \sum_{\hat{i}=1}^{n_{cont}} \sum_{\hat{j}=1}^{m_{cont}} \sum_{\hat{k}=1}^{o_{cont}} N'_{\hat{i},p_{x_1}}(\beta) M_{\hat{j},p_{x_2}}(\gamma) O_{\hat{k},p_{x_3}}(\zeta) w_{\hat{i},\hat{j},\hat{k}},$$

$$\frac{\partial}{\partial \beta} \mathbf{NV}(\beta,\gamma,\zeta) = \sum_{i=1}^{n_{cont}} \sum_{j=1}^{m_{cont}} \sum_{k=1}^{o_{cont}} \frac{\partial}{\partial \beta} R_{i,j,k}^{p_{x_1},p_{x_2},p_{x_3}}(\beta,\gamma,\zeta) \mathbf{P}_{i,j,k}.$$
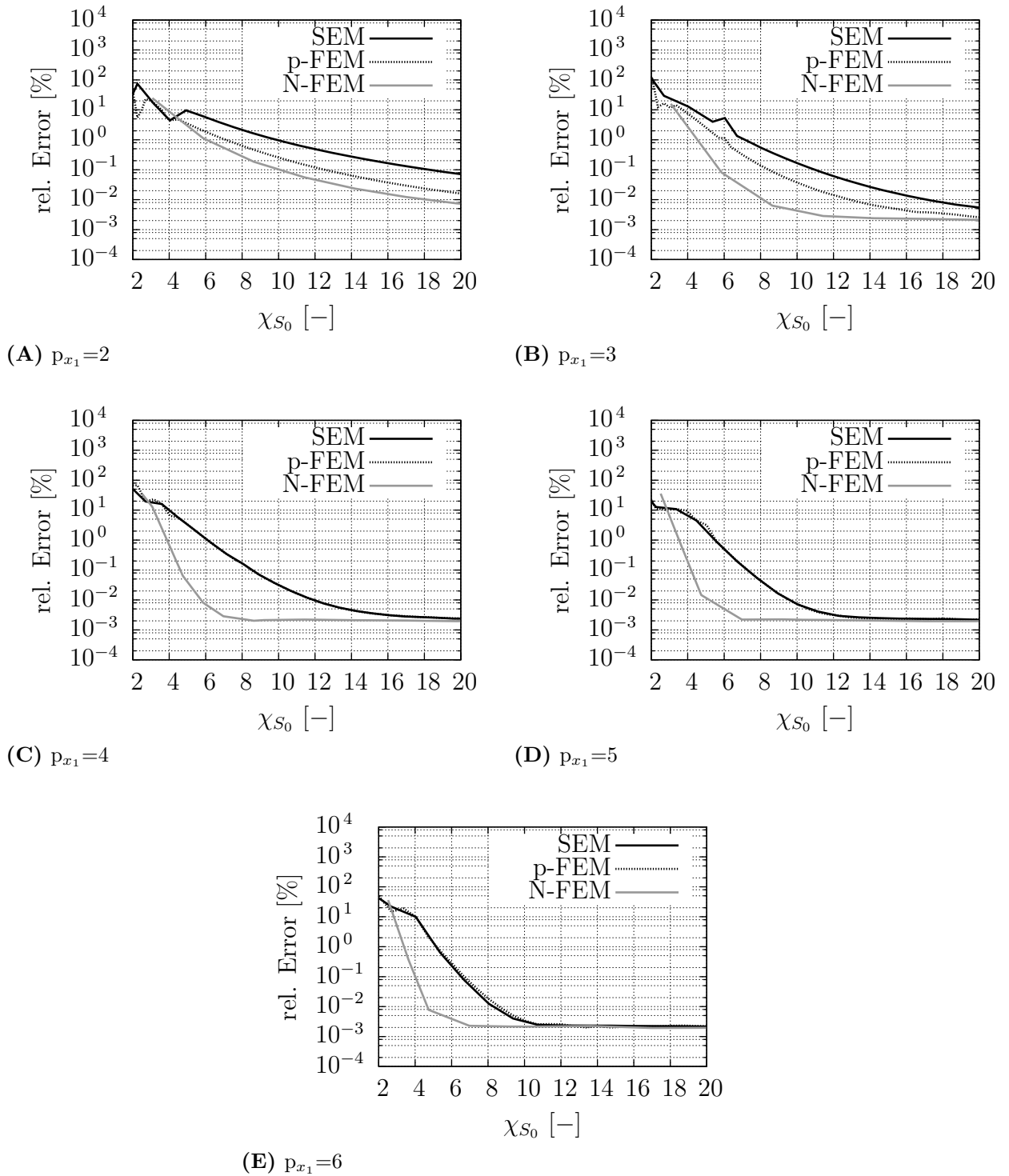
(B-4)

C Solutions of the convergence study

(A) $p_{x_1}=2$

(B) $p_{x_1}=3$

(C) $p_{x_1}=4$

(D) $p_{x_1}=5$

(E) $p_{x_1}=6$

Figure C–1: Convergence curve for the S_0-mode.

References

[1] Materials Classroom, University of Liverpool, http://www.whystudymaterials.ac.uk /casestudies/piezo.asp, Apr. 2012.

[2] PI Ceramic GmbH, Lederhose - GERMANY, http://www.piceramic.com/index.php, Feb. 2011.

[3] Columbia accident investigation board, 2003.

[4] Z. A. B. Ahmad. *Numerical Simulations of Lamb waves in plates using a semi-analytical finite element method.* PhD thesis, Otto-von-Guericke-University of Magdeburg, Fortschritt-Berichte VDI Reihe 20, Nr. 437, Düsseldorf: VDI Verlag, ISBN:978-3-18-343720-7, 2011.

[5] D. Alleyne and P. Cawley. A two-dimensional Fourier transform method for the measurement of propagating multimode signals. *Journal of the Acoustical Society of America*, 89(3):1159–1168, 1991.

[6] J. P. Andrews, A. N. Palazotto, M. P. DeSimio, and O. S. E. Lamb wave propagation in varying isothermal enviroments. *Structural Health Monitoring*, 7:265–270, 2008.

[7] J. W. Ayres, F. Lalande, C. Zaffir, and C. A. Rogers. Qualitative impedance-based health monitoring of civil infrastructures. *Smart Materials and Structures*, 7:599–605, 1998.

[8] R. Balasubramanyamy, D. Quinneyz, R. E. Challisy, and C. P. D. Toddy. A finite-difference simulation of ultrasonic Lamb waves in metal sheets with experimental verification. *Journal of Physics D: Applied Physics*, 29:147–155, 1996.

[9] R. H. Bartels, J. C. Beatty, and B. A. Barsky. *An Introduction to Splines for use in Computer Graphics & Geometric Modeling.* Morgan Kaufmann Publishers, Inc., ISBN: 1-55860-400-6, 1996.

[10] I. Bartoli, F. L. di Scalea, M. Fateh, and E. Viola. Modeling guided wave propagation with application to the long-range defect detection in railroad tracks. *NDT & E International*, 38:325–334, 2005.

[11] K.-J. Bathe. *Finite-Elemente-Methoden.* Springer, ISBN: 3-540-66806-3, 2002.

[12] Y. Bazilevs. *Isogeometric Analysis of Turbulence and Fluid-Structure Interaction.* PhD thesis, The University of Texas at Austin, 2006.

[13] Y. Bazilevs, L. Beirão da Veiga, J. A. Cottrell, T. J. R. Hughes, and G. Sangalli. Isogeometric analysis: Approximation, stability and error estimates for h-refined meshes. *Mathematical Models and Methods in Applied Sciences*, 16(7):1031–1090, 2006.

[14] C. Becker. *Finite Elemente Methoden zur räumlichen Diskretisierung von Mehrfeldproblemen der Strukturmechanik unter Berücksichtigung diskreter Risse*. PhD thesis, Ruhr-University of Bochum, 2007.

[15] T. Belytschko and L. P. Bindeman. Assumed strain stabilization of the eight node hexahedral element. *Computer Methods in Applied Mechanics and Engineering*, 105:225–260, 1993.

[16] A. Bertram. *Elasticity and Plasticity of Large Deformations - an Introduction*. Springer, ISBN: 3-540-24033-0, 2005.

[17] S. Bhalla and C. K. Soh. Electromechanical impedance modeling for adhesively bonded piezo-transducers. *Journal of Intelligent Material Systems and Structures*, 15:955–972, 2004.

[18] C. Boller, W. Staszewski, and G. Tomlinson. *Health Monitoring of Aerospace Structures*. John Wiley & Sons, ISBN: 0-470-84340-3, 2004.

[19] T. H. Brockmann. *Theory of Adaptive Fiber Composites: From Piezoelectric Material Behavior to Dynamics of Rotating Structures*. Springer, ISBN: 978-90-481-2434-3, 2009.

[20] H. Bröker. *Integration von geometrischer Modellierung und Berechnung der p-Version der FEM*. PhD thesis, Technical University of Munich, 2001.

[21] R. K. Burla. *Finite Element Analysis using uniform B-spline Approximation and Implicit Boundary Method*. PhD thesis, University of Florida, 2008.

[22] M. Calomfirescu. *Lamb Waves for Structural Health Monitoring in Viscoelastic Composite Materials*. PhD thesis, University of Bremen, April 2008.

[23] T. H. T. Chan, L. Yu, H. Y. Tam, Y. Q. Ni, S. Y. Liu, W. H. Chung, and L. K. Cheng. Fibre Bragg grating sensors for structural health monitoring of Tsing Ma bridge: Background and experimental observation. *Engineering Structures*, 28:648–659, 2006.

[24] Y. Cho. Estimation of ultrasonic guided wave mode conversion in a plate with thickness variation. *IEEE Transactions on Ultrasonics, Ferroelectrics, and Frequency Control*, 47(3):591–603, 2000.

[25] C. C. Ciang, J.-R. Lee, and H.-J. Bang. Structural health monitoring for a wind turbine system: A review of damage detection methods. *Measurement Science and Technology*, 19:122001, 2008.

[26] E. Cohen, T. Lyche, and L. L. Schumaker. Degree raising for splines. *Journal of Approximation Theory*, 46:170–181, 1986.

[27] T. Cohen, E. Martin and R. M. Kirby. Analysis-aware modeling: Understanding quality considerations in modeling for isogeometric analysis. *Computer Methods in Applied Mechanics and Engineering*, 199:334–356, 2010.

[28] R. D. Costley Jr. and Y. H. Berthelot. Dispersion curve analysis of laser-generated lamb waves. *Ultrasonics*, 32(4):249 – 253, 1994.

[29] J. A. Cottrell, T. J. R. Hughes, and Y. Bazilevs. *Isogeometric analysis: Toward integration of CAD and FEA*. John Wiley & Sons, ISBN-10: 0470748737, 2009.

[30] J. A. Cottrell, T. J. R. Hughes, and A. Reali. Studies of refinement and continuity in isogeometric structural analysis. *Computer Methods in Applied Mechanics and Engineering*, 196:4160–4183, 2007.

[31] J. A. Cottrell, A. Reali, Y. Bazilevs, and T. J. R. Hughes. Isogeometric analysis of structural vibrations. *Computer Methods in Applied Mechanics and Engineering*, 195:5257–5296, 2006.

[32] M. G. Cox. The numerical evaluation of B-splines. *Journal of the Institute of Mathematics and its Applications*, 10:134–149, 1972.

[33] M. G. Cox. Practical spline approximation. *Topics in Numerical Analysis, Springer*, 965:79–112, 1982.

[34] L. J. Crane, M. D. Gilchrist, and J. J. H. Miller. Analysis of Rayleigh-Lamb wave scattering by a crack in an elastic plate. *Computational Mechanics*, 19:533–537, 1997.

[35] E. F. Crawley and J. de Luis. Use of piezoelectric actuators as elements of intelligent structures. *AIAA Journal*, 25:10, 1987.

[36] C. de Boor. On calculating with B-splines. *Journal of Approximation Theory*, 6:50–62, 1972.

[37] C. de Boor. *Splinefunktionen*. Birkenhäuser, ISBN: 3-7643-2514-3, 1990.

[38] C. de Boor. *A practical guide to splines*. Springer, ISBN: 3-540-90356-9, 1993.

[39] P. Deuflhard and A. Hohmann. *Numerische Mathematik I*. Gruyter, ISBN 978-3110171822., 2002.

[40] S. Duczek. Entwicklung eines finiten 3D-Schichtelementes nach der p-Methode für die Berechnung von Lamb-Wellen in Faserverbundstrukturen. Diplomathesis, Otto-von-Guericke-University Magdeburg, 2010.

[41] S. Duczek, C. Willberg, D. Schmicker, and U. Gabbert. Development, validation and comparison of higher order finite element approaches to compute the propagation of Lamb waves efficiently. *Key Engineering Material*, 518:95–105, 2012.

[42] H. Duflo, B. Morvan, and J.-L. Izbicki. Interaction of Lamb waves on bonded composite plates with defects. *Composite Structures*, 79:229–233, 2007.

[43] A. Düster. *High order Finite Elements for three dimensional, thin-walled nonlinear continua*. PhD thesis, Technical University of Munich, 2002.

[44] J. A. Evans, Y. Bazilevs, I. Babuška, and T. J. R. Hughes. *n*-Widths, sup-infs, and optimality ratios for the *k*-version of the isogeometric finite element method. *Computer Methods in Applied Mechanics and Engineering*, 198:1726–1741, 2009.

[45] G. Farin. *NURBS from Projective Geometry to Practical Use.* AK Peters, ISBN: 1-56881-084-9, 1999.

[46] C. R. Farrar, S. W. Doebling, and D. A. Nix. Vibration-based structural damage identification. *Philosophical Transactions of the Royal Society A*, 359:131–149, 2001.

[47] D. P. Flanagan and T. Belytschko. A uniform strain hexahedron and quadrilateral with orthogonal hourglass control. *International Journal for Numerical Methods in Engineering*, 17:679–706, 1981.

[48] U. Gabbert, A. Görnandt, and H. Köppe. Benchmark problems for the analysis of piezothermoelastic smart structures. *Proceedings of the NAFEMS Seminar: Finite element application for adaptive strucural elements, Magdeburg November 11-12., 1998*, (paper no. 5), 1998.

[49] V. Giurgiutiu. *Structural Health Monitoring with Piezoelectric Wafer Active Sensors.* Academic Press (Elsevier), ISBN-13: 978-0-12-088760-6, 2008.

[50] S. Gopalakrishnan. *Finite Elements: Modeling of Piezoceramic and Magnetostrictive Sensors and Actuators*, chapter 43, pages 811–831. in Encyclopedia of Structural Health Monitoring; John Wiley & Sons, ISBN-10: 0470058226, 2009.

[51] A. Görnandt and U. Gabbert. Finite element analysis of thermopiezoelectric smart structures. *Acta Mechanica*, 154:129–140, 2002.

[52] G. T. Günter. *Ökonomischer und ökologischer Leichtbau mit faserverstärkten Polymeren.* expert-Verlag, ISBN 3-8169-1416-0, 1997.

[53] S. Ha. *Modeling Lamb Wave Propagation Induced by Adhesively Bonded PZTs on Thin Plates.* PhD thesis, Stanford University, California, USA, 2009.

[54] S. Ha. Adhesive interface layer effects in PZT-induced Lamb wave propagation. *Smart Materials and Structures*, 19:025006, 2010.

[55] G. Hamel. *Theoretische Mechanik. Eine einheitliche Einführung in die gesamte Mechanik.* Springer, ISBN-10: 3540038167, 1949.

[56] G. Hayward and J. Hyslop. Determination of Lamb wave dispersion data in lossy anisotropic plates using time domain finite element analysis. Part I: Theory and experimental verification. *IEEE Transactions on Ultrasonics, Ferroelectrics, and Frequency Control*, 53(2):443–448, february 2006.

[57] G. Hayward and J. Hyslop. Determination of Lamb wave dispersion data in lossy anisotropic plates using time domain finite element analysis. Part II: Application to 2-2 and 1-3 piezoelectric composite transducer arrays. *IEEE Transactions on Ultrasonics, Ferroelectrics, and Frequency Control*, 53(2):449–455, february 2006.

[58] W. Heywang, K. Lubitz, and W. Wersing. *Piezoelectricity Evolution and Future of a Technology.* Springer Series in Materials Science, ISBN: 978-3-540-68680-4, 2008.

[59] W. Hillger. Lamb-Wellen zur Schadensanzeige in faserverstärkten Kunststoffen. In *DGZfP-Jahrestagung 2005, 2.-4. Mai, Rostock*, 2005.

[60] W. Hillger. Structural heath monitoring using lamb waves and visualization of their propagation in composites. In *EU Project Meeting on Aircraft Integrated Structural Health Assessment (AISHA), Leuven, Belgium, June 2007*, 2007.

[61] S. M. H. Hosseini and U. Gabbert. Analysis of guided Lamb wave propagation (GW) in honeycomb sandwich panels. In *PAMM, Proceedings in Applied Mathematics and Mechanics, ,Volume 10, Issue 1, pp. 11-14.*, 2010.

[62] N. Hu, T. Shimomukai, H. Fukunaga, and Z. Su. Damage identification of metallic structures using A_0 mode of Lamb waves. *Structural Health Monitoring*, 7(3):271–285, 2008.

[63] C.-H. Huang, Y.-C. Lin, and C.-C. Ma. Theoretical analysis and experimental measurement of resonant vibration of piezoceramic circular plates. *IEEE Transactions on Ultrasonics, Ferroelectrics, and Frequency Control*, 51:12–24, 2004.

[64] H. Huang, T. Pamphile, and M. Derriso. The effect of actuator bending on Lamb wave displacement fields generated by a piezoelectric patch. *Smart Materials and Structures*, 17:1–13, August 2008.

[65] T. J. R. Hughes. *The Finite Element Method*. Prentence-Hall International (UK) Limited, ISBN-10: 0486411818, 1987.

[66] T. J. R. Hughes, J. A. Cottrell, and Y. Bazilevs. Isogeometric analysis: CAD, finite elements, NURBS, exact geometry and mesh refinement. *Computer Methods in Applied Mechanics and Engineering*, 194:4135–4195, 2005.

[67] T. J. R. Hughes, A. Reali, and G. Sangalli. Efficient quadrature for NURBS-based isogeometric analysis. *Computer Methods in Applied Mechanics and Engineering*, 199:301–313, 2010.

[68] T. Ikeda. *Fundamentals of piezoelectricity*. Oxford science publications. Oxford University Press, 1996.

[69] S.-H. Jun, S.-M. Lee, S.-H. Lee, K.-E. Kim, and K.-W. Lee. Piezoelectric linear motor with unimorph structure by co-extrusion process. *Sensors and Actuators A: Physical*, 147(1):300–303, 2008.

[70] I. Kang, M. J. Schulz, J. H. Kim, V. Shanov, and D. Shi. A carbon nanotube strain sensor for structural health monitoring. *Smart Materials and Structures*, 15:737–748, 2005.

[71] S. Katzir. *The Beginnings of Piezoelectricity*. Springer, ISBN-10 1-4020-4669-3, 2006.

[72] S. Kessler, M. Spearing, and M. Atallab. In-situ damage detection of composites structures using Lamb wave methods. In *Proc. First European Workshop on Structural Health Monitoring 10-12 July 2002 Paris France*, pages 374–381, 2002.

[73] H.-J. Kim, Y.-D. Seo, and Y. S.-K. Isogeometric analysis for trimmed CAD surfaces. *Computer Methods in Applied Mechanics and Engineering*, 198:2982–2995, 2009.

[74] H. Kioua and S. Mirza. Piezoelectric induced bending and twisting of laminated composite shallow shells. *Smart Materials and Structures*, 9:476 – 484, 2000.

[75] S. Koch. Untersuchung an der materialinduzierten Modenkonversion von Lambwellen in Faserverbundplatten. Diplomathesis, Otto-von-Guericke-University Magdeburg, 2011.

[76] D. Komatitsch and J. Tromp. Spectral-element simulations of global seismic wave propagation - I validation. *International Journal of Geophysics*, 149:390–412, 2002.

[77] P. Kudela, M. Krawczuk, and W. M. Ostachowicz. Wave propagation modelling in 1D structures using spectral elements. *Journal of Sound and Vibration*, 300:88–100, 2007.

[78] P. Kudela and W. M. Ostachowicz. 3D time-domain spectral elements for stress waves modelling. *Journal of Physics*, 181, 2009.

[79] T. Kuroishi, H. Nishimura, N. Matsumoto, A. Shiibashi, F. Sakata, and K. Aoki. Guided wave pipe inspection and monitoring system. Technical report, Mitsubishi Heavy Industries, Ltd. Technical Review Vol. 42 No. 3, 2005.

[80] M. W. Lai, D. Rubin, and E. Krempl. *Introduction to Continuum Mechanics*. Butterworth-Heinemann, ISBN-10: 0080169716, 1993.

[81] H. Lamb. On waves in an elastic plate. *Royal Society of London Proceedings Series A*, 93:114–128, mar 1917.

[82] R. Lammering. Observation of piezoelectrically induced Lamb wave propagation in thin plates by use of speckle interferometry. *Experimental Mechanics*, 50:377–387, 2010.

[83] G. Lanzara, Y. Yoon, Y. Kim, and F.-K. Chang. Influence of interface degradation on the performance of piezoelectric actuators. *Journal of Intelligent Material Systems and Structures*, 20:1699–1710, 2009.

[84] B. C. Lee and W. J. Staszewski. Modelling of Lamb waves for damage detection in metallic structures: Part I. Wave propagation. *Smart Materials and Structures*, 12:804–814, 2003.

[85] B. C. Lee and W. J. Staszewski. Modelling of Lamb waves for damage detection in metallic structures: Part II. Wave interactions with damages. *Smart Materials and Structures*, 12:815–824, 2003.

[86] B. C. Lee and W. J. Staszewski. Lamb wave propagation modelling for damage detection: II. Damage monitoring strategy. *Smart Materials and Structures*, 16:260–274, 2007.

[87] E. T. Y. Lee. A note on blossoming. *Computer Aided Geometric Design*, 6:359–362, 1989.

[88] W. H. Leong, W. J. Staszewski, B. C. Lee, and F. Scarpa. Structural health monitoring using scanning laser vibrometry: III. Lamb waves for fatigue crack detection. *Smart Materials and Structures*, 14:1387–1395, 2005.

[89] S. Li and C. J. Lissenden. Piezoelectric fiber composite strip transducer design considerations for generating Lamb waves. *Journal of Intelligent Material Systems and Structures*, 22:1345–1358, 2011.

[90] C. Liang, F. P. Sun, and C. A. Rogers. Coupled electro-mechanical analysis of adaptive material systems - deteremination of the actuator power consumption and system energy transfer. *Journal of Intelligent Material Systems and Structures*, 5(1):12–20, 1994.

[91] X. Lin and F. G. Yuan. Diagnostic Lamb waves in an integrated piezoelectric sensor/actuator plate: analytical and experimental studies. *Smart Materials and Structures*, 10:907–913, 2001.

[92] S. Lipton, J. Evans, Y. Bazilevs, T. Elguedj, and T. J. R. Hughes. Robustness of isogeometric structural discretization under severe mesh distortion. *Computer Methods in Applied Mechanics and Engineering*, 199:357–373, 2010.

[93] Y. Liu, H. Ning, Alamusi, T. Watanabe, Y. Koshin, Y. Cao, and H. Fukunaga. Relative reflection intensity of Lamb waves from elliptically-shaped damages in metallic plates. *Smart Materials and Structures*, 20, 2011.

[94] M. Majumder, T. K. Gangophyay, A. K. Chkraborty, K. Dasgupta, and D. K. Bhattacharya. Fibre bragg gratings in structural health monitoring - Present stratus and applicactions. *Sensors and Actuators A: Physical*, 174:150–164, 2008.

[95] D. Marinkovìc. *A new finite composit shell element for piezoelectric active structures*. PhD thesis, Otto-von-Guericke-University Magdeburg, Fortschritt-Berichte VDI Reihe 20, Nr. 406, Düsseldorf: VDI Verlag, ISBN:978-3-18-340620-3, 2007.

[96] D. Marinkovìc, H. Köppe, and U. Gabbert. Numerically efficient finite element formulation for modeling active composite laminates. *Mechanics of Advanced Materials and Structures*, 13:379–392, 2006.

[97] R. Mohamed, D. L. Demer, and P. Masson. A parametric study of piezoelectric thickness effect on the generation of fundamental Lamb modes. In *Health Monitoring of Structural and Biological Systems, Proceedings of SPIE Vol. 7984*, 2011.

[98] J. Moll, R. T. Schulte, B. Hartmann, C.-P. Fritzen, and O. Nelles. Multi-site damage localization in anisotropic plate-like structures using an active guided wave structural health monitoring system. *Smart Materials and Structures*, 19:1–16, 2010.

[99] T. Monnier. Lamb waves-based impact damage monitoring of a stiffened aircraft panel using piezoelectric transducers. *Journal of Intelligent Material Systems and Structures*, 17:411–421, 2006.

[100] G. Mook, J. Pohl, C. Willberg, and J. Simonin. Ankopplung, Ausbreitung und Wechselwirkung von Lambwellen zur strukturintegrierten Bauteilüberwachung von Faserverbunden. In *10. Magdeburger Maschinenbau-Tage: Forschung und Innovation, Universität Magdeburg (Germany), 27.-29.9.2011, Beitrag B4-5, ISBN: 978-3-940961-60-0*, 2011.

[101] F. Moser, J. J. Laurence, and J. Qu. Modeling elastic wave propagation in waveguides with finite element method. *NDT & E International*, 32:225–234, 1999.

[102] E. Moulin, J. Assaad, and C. Delebarre. Piezoelectric transducer embedded in a composite plate: Application to Lamb wave generation. *Journal of Applied Physics*, 82 (5):2049–2055, 1997.

[103] H. Nakano and S. Nagai. Laser generation of antisymmetric Lamb waves in thin plates. *Ultrasonics*, 29:230–234, 1991.

[104] A. H. Nayteh. *Wave propagation in layered media with applications to composites.* North-Holland Series in Applied Mathematics and Mechanics, Volume 39, ISBN 10: 0444890181, 1995.

[105] W. M. Ostachowicz, T. Wandowski, and P. Malinowski. Elastic wave phased array for damage localisation. *Journal of Theoretical and Applied Mechanics*, 46(4):917–931, 2008.

[106] R. Paradies and B. Schläpfer. Finite element modeling of piezoelectric elements with complex electrode configuration. *Smart Materials and Structures*, 18:1–13, 2009.

[107] G. Park, H. Sohn, C. Farrar, and D. J. Inman. Overview of piezoelectric impedance-based health monitoring and path forward. *The Shock and Vibration Digest*, 35(6):451–463, 2003.

[108] J. Parvizian, A. Düster, and E. Rank. Finite Cell Method: h- and p-extension for embedded domain methods in solid mechanics. *Computational Mechanics*, 41:122–133, 2007.

[109] K. J. Peters, editor. *Sensor Systems and Networks: Phenomena, Technology, and Application for NDE an Health Monitoring, Proc. of SPIE Vol. 6530, 65300J*, volume 6530, 2007.

[110] K. J. Peters, editor. *Sensor Systems and Networks: Phenomena, Technology, and Application for NDE an Health Monitoring, Proc. of SPIE Vol. 6530, 65300L*, volume 6530, 2007.

[111] V. Piefort. *Finite Element Modelling of Piezoelectric Active Structures.* PhD thesis, Université Libre de Bruxelles, 2001.

[112] L. Piegl and W. Tiller. *The NURBS Book.* Springer, ISBN: 3-540-55069-0, 1995.

[113] J. Pohl. *Zerstörungsfreie Charakterisierung adaptiver CFK-Piezokeramik-Verbunde (konventionelle Verfahren und health monitoring).* State doctorate thesis, Otto-von-Guericke-University Magdeburg, 2003.

[114] J. Pohl, S. Herold, G. Mook, and F. Michel. Damage detection in smart CFRP-composites by impedance spectroscopy. *Smart Materials and Structures*, 10:834–842, 2001.

[115] J. Pohl, C. Willberg, U. Gabbert, and G. Mook. Analyse der Lambwellen-erzeugung durch Piezoaktoren in Structural Health Monitoring-Systemen. In *ZfP in Forschung, Entwicklung und Anwendung, DGZfP-Jahrestagung, Bremen, 30.5.-1.6.2011, Berichtsband 127-CD, Mo.3.A.2, ISBN 978-3-940283-33-7*, 2011.

[116] J. Pohl, C. Willberg, U. Gabbert, and G. Mook. Theoretical analysis and experimental determination of the dynamic behaviour of piezoceramic actuators for SHM. *Experimental Mechanics*, 51(4):429–438, 2012.

[117] W. H. Prosser, K. E. Jackson, S. Kellas, B. T. Smith, J. McKeon, and A. Friedman. Advanced, waveform based acoustic emission detection of matrix cracking in composites. *Materials Evaluation*, 9:1052–1058, 1995.

[118] X. Qian. Full analytical sensitivities in NURBS based isogeometric shape optimization. *Computer Methods in Applied Mechanics and Engineering*, 199:2059–2071, 2010.

[119] X. P. Qinga, H.-L. Chana, S. J. Bearda, T. K. Ooib, and S. A. Marottab. Effect of adhesive on the performance of piezoelectric elements used to monitor structural health. *International Journal of Adhesion and Adhesives*, 26(8):622–628, 2006.

[120] O. Rabinovitch and J. R. Vinson. Adhesive layer effects in surface mounted piezoelectric actuators. *Journal of Intelligent Material Systems and Structures*, 13:689–704, November 2002.

[121] A. Raghavan and C. E. S. Cesnik. Review of guided-wave structural health monitoring. *The Shock and Vibration Digest*, 39:91–114, 2007.

[122] C. Ramadas, K. Balasubramaniam, A. Hood, M. Joshi, and C. Krishnamurthy. Modelling of attenuation of lamb waves using rayleigh damping: Numerical and experimental studies. *Composite Structures*, 93:2020–2025, 2011.

[123] C. Ramadas, K. Balasubramaniam, M. Joshi, and C. V. Krishnamurthy. Interaction of the primary anti-symmetric Lamb mode (A0) with delaminations: numerical and experimental studies. *Smart Materials and Structures*, 18:1–7, 2009.

[124] A. Reali. An isogeometric analysis approach for the study of structural vibrations. Master's thesis, Rose School: European School for Advanced Studies in Reduction of Seismic Risk, 2004.

[125] J. N. Reddy. *An Introduction to the Finite Element Method*. McGraw-Hill, ISBN: 0-07-051355-4, 1993.

[126] D. Rosenberger. *Technische Anwendungen des Lasers*. Springer, ISBN: 3-540-06533-4, 1975.

[127] M. Ruzzene. Frequency-wavenumber domain filtering for improved damage visualization. *Smart Materials and Structures*, 16:2116–2129, 2006.

[128] M. K. Samal, P. Seshu, S. Parashar, U. von Wagner, P. Hagedorn, B. K. Dutta, and H. S. Kushwaha. A finite element model for nonlinear behaviour of piezoceramics under weak electric fields. *Finite Elements in Analysis and Design*, 41:1464–1480, 2005.

[129] D. Schillinger, M. Ruess, N. Zander, Y. Bazilevs, A. Düster, and E. Rank. Small and large deformation analysis with the *p*- and B-spline version of the Finite Cell Method. *Computational Mechanics*, pages 1–34 (online first), 2012.

[130] D. Schmicker. Development and testing of higher order finite elements based on lagrange polynomials for the analysis of guided ultrasonic waves in thin-walled structures. Diplomathesis, Otto-von-Guericke-University Magdeburg, 2011.

[131] D. Schmidt. Dokumentation CFK-Testplatten. Technical report, DLR, Institute of Composite Structures and Adaptive Systems, 2010.

[132] I. Schoenberg. Contributions to the problem of approximation of equidistant data by analytic functions. *Quarterly of applied mathematics*, 4:45–99 and 112–141, 1946.

[133] H. Schürmann. *Konstruieren mit Faser-Kunststoff-Verbunden*. Springer, ISBN: 978-3-540-72189-5, 2007.

[134] M. Senesi and M. Ruzzene. A frequency selective acoustic transducer for directional Lamb wave sensing. *Journal of the Acoustical Society of America*, 10(4):1899–1907, 2011.

[135] A. Shelke, T. Kundu, U. Amjad, K. Hahn, and W. Grill. Mode-selective excitation and detection of ultrasonic guided waves for delamination detection in laminated aluminum plates. *IEEE Transactions on Ultrasonics, Ferroelectrics, and Frequency Control*, 58(3):567–577, 2011.

[136] J. Sirohi and I. Chopra. Fundamental understanding of piezoelectric strain sensors. *Journal of Intelligent Material Systems and Structures*, 11:246–257, 2000.

[137] H. Sohn, D. Dutta, J. Y. Yang, M. DeSimio, S. Olson, and E. Swenson. Automated detection of delamination and disbond from wavefield images obtained using a scanning laser vibrometer. *Smart Materials and Structures*, 20(4):045017, 2011.

[138] H. Sohn and S. J. Lee. Lamb wave tuning curve calibration for surface-bonded piezoelectric transducers. *Smart Materials and Structures*, 19:015007, 2010.

[139] W. Staszewski, C. Boller, and G. Tomlinson, editors. *Health Monitoring of Aerospace Structures - Smart Sensor Technologies and Signal Processing*. John Wiley & Son, ISBN-13: 978-0470843406, 2004.

[140] W. J. Staszewski, B. C. Lee, L. Mallet, and F. Scarpa. Structural health monitoring using scanning laser vibrometry: I. Lamb wave sensing. *Smart Materials and Structures*, 13:251–260, 2004.

[141] W. J. Staszewski, B. C. Lee, and R. Traynor. Fatigue crack detection in metallic structures with Lamb waves and 3D laser vibrometry. *Measurement Science and Technology*, 18:727–739, 2007.

[142] W. J. Staszewski, S. Mahzan, and R. Traynor. Health monitoring of aerospace composite structures - Active and passive approach. *Composites Science and Technology*, 69:1678–1685, 2009.

[143] Z. Su and L. Ye. *Identification of Damage Using Lamb Waves: From Fundamentals to Applications.* Springer, ISBN: 978-1-84882-783-7, 2009.

[144] Z. Su, L. Ye, and Y. Lu. Guided Lamb waves for identification of damage in composite structures: A review. *Journal of Sound and Vibration*, 295:753–780, 2006.

[145] B. Szabó and I. Babŭska. *Finite Element Analysis.* John Wiley & Son, ISBN: 0-471-50273-1, 1991.

[146] K. Sze and L. Yao. Modeling smart structures with segmented piezoelectric sensors an actuators. *Journal of Sound and Vibration*, 235:495–520, 2000.

[147] K. S. Tan, N. Guo, B. S. Wong, and C. G. Tui. Experimental evaluation of delaminations in composite plates by the use of Lamb waves. *Composites Science and Technology*, 53:77–84, 1995.

[148] G. U. Tian, J. and, H. Berger, and X. Su. Lamb wave interaction with delaminations in CFRP laminates. *Computers, Materials, & Continua*, 1:327–336, 2004.

[149] W. Tiller. Rational B-splines for curve and surface representation. *IEEE Computer Graphics and Applications*, 24:36–46, 1983.

[150] N. Toyama and J. Tkatsubo. Lamb wave method for quick inspection of impact-induced delaminations in composite laminates. *Composites Science and Technology*, 64:1293–1300, 2004.

[151] K. K.-H. Tseng and A. S. K. Naidu. Non-parametric damage detection and characterization using smart piezoceramic material. *Smart Materials and Structures*, 11:317–329, 2002.

[152] T.-K. Uhm and S.-K. Youn. T-spline finite element method for analysis of shell structures. *International Journal for Numerical Methods in Engineering*, 80:507–536, 2009.

[153] A. Ungethüm. *Migrationsbasierte Lokalisierung von Schadensereignissen und Schäden in flächigen anisotropen Strukturen.* PhD thesis, Helmut-Schmidt-University Hamburg, Bericht aus dem Institut für Mechanik, ISSN 0939-2343, 2011.

[154] K. J. Versprille. *Computer-aided design applications of the rational B-spline approximation form.* PhD thesis, Syracuse University, Syracuse, NY, USA, 1975.

[155] I. A. Viktorov. *Rayleigh and Lamb Waves.* Plenum Press, 1967.

[156] J. M. Vivar-Perez. *Analytical and spectral methods for the simulation of elastic waves in thin plates.* PhD thesis, Otto-von-Guericke-University of Magdeburg, Fortschritt-Berichte VDI Reihe 20, Nr. 441, Düsseldorf: VDI Verlag, ISBN:978-3-18-344120-4, 2012.

[157] J. M. Vivar-Perez, C. Willberg, and U. Gabbert. Simulation of piezoelectric Lamb waves in plate structures. In *International Conference on Structural Engineering Dynamics. ICEDyn Ericeira, Portugal. 22.-24. Juni, 2009*, 2009.

[158] S. von Ende. *Transient angeregte Lamb-Wellen in elastischen und viskoelastischen Platten.* PhD thesis, Helmut-Schmidt-University Hamburg, Bericht aus dem Institut für Mechanik, 2008.

[159] S. von Ende and R. Lammering. Investigations on piezoelectrically induced Lamb wave generation and propagation. *Smart Materials and Structures*, 16:1802–1809, 2007.

[160] C.-Y. Wang and J. D. Achenbach. Lamb's problem for solid of general anisotropy. *Wave Motion*, 24:227–242, 1996.

[161] P. D. Wilcox, M. J. S. Lowe, and P. Cawley. Mode and transducer selection for long range Lamb wave inspection. *Journal of Intelligent Material Systems and Structures*, 12:553–565, 2001.

[162] C. Willberg, S. Duczek, and U. Gabbert. Increasing the scanning range of Lamb wave based SHM systems by optimizing the actuator - sensor design. *CEAS Aeronautical Journal*, 2013 (online first).

[163] C. Willberg, S. Duczek, J. Pohl, G. Mook, and U. Gabbert. Adhesive layer influence of piezoelectric induced Lamb waves. In *Proceedings ECCM 2010 Paris France*, 2010.

[164] C. Willberg, S. Duczek, J. M. Vivar-Perez, D. Schmicker, and U. Gabbert. Comparison of different higher order finite element schemes for the simulation of Lamb waves. *Computer Methods in Applied Mechanics and Engineering*, 241-244:246–261, 2012.

[165] C. Willberg and U. Gabbert. Development of a three-dimensional piezoelectric isogeometric finite element for smart structure applications. *Acta Mechanica*, 223(8):1837–1850, 2012.

[166] C. Willberg, S. Koch, G. Mook, U. Gabbert, and J. Pohl. Continuous mode conversion of Lamb waves in CFRP plates. *Smart Materials and Structures*, 21(7):1–9, 2012.

[167] C. Willberg, G. Mook, U. Gabbert, and J. Pohl. The phenomenon of continuous mode conversion of Lamb waves in CFRP plates. In *2nd International Workshop on Smart Diagnostics of Structures, November 14-16, 2011, Krakow Poland*, 2011.

[168] C. Willberg, J. M. Vivar-Perez, Z. Ahmad, and U. Gabbert. Simulation of piezoelectric induced Lamb wave motion in plates. In *Proceedings of the 7th International Workshop on Structural Health Monitoring 2009: From System Integration to Autonomous Systems, 2299-2307*, 2009.

[169] C. Willberg, J. M. Vivar-Perez, and U. Gabbert. Lamb wave interaction with defects in homogeneous plates. In *International Conference on Structural Engineering Dynamics. ICEDyn Ericeira, Portugal. 22.-24. Juni, 2009*, 2009.

[170] F. Wolf. Präzisionsmessungen des Elastizitätsmoduls von Polymeren mit Longitudinalschwingungen II. Teil: Apparatur und Ergebnisse. *Colloid and Polymer Science Kolloid-Zeitschrift & Zeitschrift für Polymere*, 257:1253–1275, 1979.

[171] D. C. Worlton. Experimental confirmation of Lamb waves at megacycle frequencies. *Journal of Applied Physics*, 32 (6):967–971, 1961.

[172] Z. Yan, S. ZhongHua, L. Jian, and N. XiaoWu. Numerical simulation and experimental detection of leaky Lamb waves induced by pulse laser at air-solid interfaces. *Science in China Series G: Physics, Mechanics & Astronomy, Springer Verlag, Science in China Press*, 51:607–616, 2008.

[173] C. Yang, L. Ye, Z. Su, and M. Bannister. Some aspects of numerical simulation for Lamb wave propagation in composite laminates. *Composite Structures*, 75:267–275, 2006.

[174] Y. Yeh and H. Z. Cummings. Localized fluid flow measurements with a HeNe laser spectrometer. *Applied Physics Letters*, 4:176–178, 1964.

[175] H. Yim and Y. Sohn. Numerical simulation and visualization of elastic waves using mass-spring lattice model. *IEEE Transactions on Ultrasonics, Ferroelectrics, and Frequency Control*, 47(3):549–558, 2000.

[176] O. C. Zienkiewicz and R. Taylor. *The Finite Element Method; Volume 1: Basis.* Butterworth-Heinemann, ISBN: 0 7506 5049 4, 2000.

[177] O. C. Zienkiewicz and R. Taylor. *The Finite Element Method; Volume 2: Solid Mechanics.* Butterworth-Heinemann, ISBN: 0 7506 5055 9, 2000.

[178] O. C. Zienkiewicz and R. Taylor. *The Finite Element Method; Volume 3: Fluid Dynamics.* Butterworth-Heinemann, ISBN: 0 7506 5050 8, 2000.

[179] C. Zwick Rosen, B. V. Hiremath, and R. Newnham. *Piezoelectricity.* American Institute of Physics, ISBN: 0-88318-647, 1992.